Alma Mater Studiorum – Università di Bologna

DOTTORATO DI RICERCA IN

BIOINGEGNERIA

Ciclo XXVII

Settore Concorsuale di afferenza: 09/G2

Settore Scientifico disciplinare: ING-INF/06

Closed-loop investigation of the dynamical properties of cardiomyocyte electrophysiology by means of Dynamic clamp and Mathematical modelling

Presentata da: Chiara Bartolucci

Coordinatore Dottorato **Relatore**

Prof. Elisa Magosso **Ph.D Stefano Severi**

Esame finale anno 2015

Ad Alessandro

ACKNOWLEDGEMENTS

Looking back on the past 3 years of my Ph.D. training, I see myself having grown and developed, both as person and as a scientist. It is impossible, however, that I would have made this progress without help from numerous people. I would like to take this opportunity to express my deepest appreciation to them.

First and foremost, I would like to acknowledge my advisor and mentor, Prof. Stefano Severi: his scientific expertise and dedication to my training have played a fundamental role on my growth, both academically and personally. I am truly indebted to Prof. Severi for all his patient guidance and support.

I also thank all the Ph.D. committee members, in particular Prof. Gianni Gnudi, for their helpful suggestions through all stages of my doctoral studies.

I want to extend my appreciation to the members of Prof. Antonio Zaza laboratory, in particular Claudia Altomare and Luca Sala, because without their help this work could not be possible.

My special thanks do to Dr. David Christini and all the members of his laboratory for welcoming me in New York and opening his laboratory to my research.

I would like to acknowledge my colleagues, Elisa Passini, Claudia Perazzini, Michelangelo Paci and Enrico Ravagli (my first "true" undergraduate student) for making these years more memorable: I feel fortunate to be working with them, not only because of all I have learned, but also all the joy and friendship.

I am especially grateful to my past university colleague Michele Antonelli, who has always believed in my talent and accompanied me during these years with his scientific support and suggestions.

Last but not least my parents who always gave me the opportunity to study. During these 3 years I have realized my self not only professionally but as a woman: I married my husband Alessandro and we have had a baby. All was possible thanks to his endless and unconditional sustain, patience and love.

KEYWORDS

Computational Biology

Cardiac Electrophysiology

Dynamic Clamp

ABSTRACT

The research field of my PhD concerns mathematical modeling and numerical simulation, applied to the cardiac electrophysiology analysis at a single cell level. This is possible thanks to the development of mathematical descriptions of single cellular components, ionic channels, pumps, exchangers and subcellular compartments. Due to the difficulties of vivo experiments on human cells, most of the measurements are acquired in vitro using animal models (e.g. guinea pig, dog, rabbit). Moreover, to study the cardiac action potential and all its features, it is necessary to acquire more specific knowledge about single ionic currents that contribute to the cardiac activity. Electrophysiological models of the heart have become very accurate in recent years giving rise to extremely complicated systems of differential equations. Although describing the behavior of cardiac cells quite well, the models are computationally demanding for numerical simulations and are very difficult to analyze from a mathematical (dynamical-systems) viewpoint. Simplified mathematical models that capture the underlying dynamics to a certain extent are therefore frequently used. **Chapter 1** contains the basic concepts about cardiomyocyte electrophysiology and action potential modelling

Cardiac action potentials (APs) are driven by ionic currents flowing through specific channels and exchangers across cardiomyocyte membranes. Once initiated by rapid Na^+ entry during phase 0, the AP time course is determined by the balance between inward depolarizing currents, carried mainly by Na^+ and Ca^{2+}, and outward repolarizing currents carried mainly by K^+. K^+ currents play a major role in repolarization. The loss of a K^+ current can impair repolarization, but there is a redundancy of K^+ currents so that when one K^+ current is dysfunctional, other K^+ currents increase to compensate, a phenomenon called ‘repolarization reserve’. Repolarization reserve protects repolarization under conditions that increase inward current or reduce outward current, threatening the balance that governs AP duration. This protection comes at the expense of reduced repolarization reserve, potentially resulting in unexpectedly large AP prolongation and arrhythmogenesis, when an additional repolarization-

suppressing intervention is superimposed. The critical role of appropriate repolarization is such that cardiac rhythm stability can be impaired with either abnormally slow or excessively rapid repolarization. Changes in the repolarization process can have a major impact on duration and shape properties of APs, which are key determinants of several important cellular functions.

A computational analysis of ventricular repolarization, using classical approach (such as voltage- and current- clamp) is described in **Chapter 2**. It has regarded a work originated from a collaboration with the Instituto de Investigaciones Biomédicas Alberto Sols, CSIC-UAM, of Madrid where we have studied a novel mutation to its short QT phenotype through multiscale computational modelling. In particular my contribution has been the simulation of the mutation using two human AP models, the ten Tusscher – Panfilov and the O'Hara Rudy, to strengthen the experimental results.

In addition to the traditional methods for the cardiac electrophysiology, this thesis is focused on the development of an innovative approach to the modelling of cardiac action potentials. My dissertation uses the dynamic clamp technique (DC), as the central technique, applying to different mathematical modelling of cardiac action potentials with the aim of gaining a clearer insight into the origin of the dynamics of electrophysiological models. In order to implement the dynamic clamp we have used the open source Real-Time eXperiment Interface (RTXI), which is a real-time biological experimentation system based on Real-Time Linux. In order to increase my knowledge on the RTXI, I have spent five months at the Weill Cornell Medical College of New York, in David Christini's laboratory, which, together with his team, has developed the RTXI software and used it in several biologic applications. The implementation of the system features and the custom user code, as modules, written in C++ for running RTXI was one of my work aspect. In **Chapter 3** a brief overview of dynamic clamp technique is exposed.

For the repolarization aforementioned importance, we have investigated with this technique different ionic currents which are responsible for it.

At first, **Chapter 4** presents the application of DC in combination with the action potential clamp technique. Both techniques were used to: 1) optimize the Luo-Rudy mathematical formulation of the guinea-pig rapid delayed rectifier K^+ current (I_{Kr}) and 2) validate the new model, analyzing the effects of the current block (using the specific blocker E4031) and of the modelled current injection on the AP duration.

In **Chapter 5**, DC was used for investigate the I_{Kr} impact on repolarization in a real cardiomyocyte, making a sensitivity analysis of AP features to parameters changing of the current kinetics (the optimized model, obtained as described in chapter 4, was tested).

In line with the work presented by Ahrens-Nicklas and Christini (2009) where they tried to anthropomorphize the mouse cardiac AP, we have used DC to compare different species. In particular, **Chapter 6** wants to clarify whether a spike – and – dome profile (SaD) (present in canine and human, but not guinea pig) is the main factor determining the direction of APD response to β – adrenergic stimulation. This work was made in collaboration with the Laboratory of Professor Zaza, at the University of Milan-Bicocca; my contribution in this work regards the implementation of dynamic clamp in order to test the effect of I_{to} introduction, and of the resulting SaD, on ISO modulation of guinea pig repolarization.

Finally we have employed DC to analyze the autonomic modulation of AP. **Chapter 7** study the "funny" current I_f present in the sinoatrial node pacemaker cells. This work has two aims: 1) a model validation between two different I_f formulations (Severi et al. 2012 and Maltsev-Lakatta 2009) blocking the native current with ivabradine and using DC for reinjecting the two "synthetic" I_f; 2) the study of the physiological mechanisms of rate modulation: which amount of isoprenaline-induced pacemaking rate increase can be ascribed to the known ISO-induced I_f activation shift?

To summarize, the results presented in this thesis have confirmed that a close integration of computational modeling and experimental recordings in real myocytes, as performed by dynamic clamp, is a useful tool in enhancing our understanding of various components of normal cardiac electrophysiology, but also arrhythmogenic mechanisms in a pathological condition, especially when fully integrated with experimental data.

CONTENTS

ACKNOWLEDGEMENTS I

KEYWORDS III

ABSTRACT V

CONTENTS VIII

CHAPTER 1 - BASIC CONCEPT ON CARDIAC ELECTROPHYSIOLOGY AND MATHEMATICAL MODELING 1

Cardiac Electrophysiology 3

Cardiac action potential 4

Proarrhythmic marker: Action Potential Duration 6

APD prolongation in heart failure 6

Cardiac Modelling 7

The Hodgkin–Huxley formalism for computing the action potential 8

Cardiac action potential models 11

CHAPTER 2 - COMPUTATIONAL ANALYSIS OF VENTRICULAR REPOLARIZATION: CLASSICAL APPROACH INVESTIGATING SHORT QT SYNDROME 16

ABSTRACT 18

INTRODUCTION 18

METHODS 19

Mutagenesis and Cell transfection 19

Preparation of cell extracts 19

Western blot analysis 19

Confocal microscopy 20

Electrophysiological recordings 20

Computational analysis 20

Statistics 20

RESULTS 21

Patient characteristics: clinical analysis and genetics 21

Characterization of F279I Kv7.1 channels 22

Inactivation is reduced by the F279I mutation 23

Properties of the WT and F279I Kv7.1/KCNE1 complexes 24

Impaired interaction between F279I Kv7.1 and KCNE1 subunits 26

Rate-dependent increase in current upon depolarizing pulse trains 27

Heterozygous condition 28

F279I mutation causes dramatic AP shortening in a ventricular cell model 30

DISCUSSION 32

CHAPTER 3 - A MODERN TOOL FOR COMPUTATIONAL AND ELECTROPHYSIOLOGY ANALYSIS: DYNAMIC CLAMP TECHNIQUE 41

INTRODUCTION 43

History 44

Dynamic Clamp 45

Real Time eXperiment Interface 46

CHAPTER 4 - USE OF DYNAMIC – CLAMP FOR AN IMPROVED IDENTIFICATION AND VALIDATION OF AN IONIC CURRENT MODEL 51

ABSTRACT 53

INTRODUCTION 54

MATERIALS AND METHODS 55

Cell isolation 55

Action-Potential Clamp 56

I_{Kr} Model 56

Dynamic-Clamp 57

Current distribution during the AP phases 58

RESULTS 59

Model Identification: AP-clamp 59

Comparison between I_{Opt} and I_{LRd} model parameters 60

Model Validation: Dynamic-clamp experiments 63

Comparison of I_{Opt} and I_{LRd} in the context of a numerical AP model 65

DISCUSSION 66

LIMITATIONS 68

CONCLUSIONS 69

CHAPTER 5 - USE OF DYNAMIC – CLAMP FOR A SENSITIVITY ANALYSIS OF THE CURRENT PARAMETERS ON THE AP FEATURES 75

ABSTRACT 77

INTRODUCTION 78

METHODS 78

Cell isolation 78

I_{Kr} numerical model 79

Electrophysiology 79

Dynamic clamp 79

Data analysis and statistics 80

RESULTS 81

I_{E4031} replacement by mI_{Kr} 81

Correlation between APD and its variability 82

Impact of mI_{Kr} features on APD and its variability 84

Changes in maximal conductance (g_{max}) 84

Changes in mid-activation voltage ($V_{0.5}A$) 86

Changes in mid-inactivation voltage ($V_{0.5}I$) 88

Changes in activation/deactivation time constant (τ) 90

Changes in mI_{Kr} distribution during repolarization 91

DISCUSSION 92

Mechanistic interpretation 94

Limitations 96

Implications 96

CHAPTER 6 - USE OF DYNAMIC – CLAMP TO COMPARE DIFFERENT SPECIES: HOW A GUINEA – PIG BECOMES DOG 101

ABSTRACT 103

INTRODUCTION 104

METHODS 105

Membrane potential and current measurements 106

Current-clamp experiments 106

Action-potential clamp 106

Dynamic clamp 106

RESULTS 107

Current-clamp experiments: ISO effects on APD 107

AP-clamp experiments: ISO effects on membrane current 107

Dynamic-clamp experiments: impact of SaD profile on APD response to ISO 109

DISCUSSION 110

Closed-loop (I-clamp) vs open-loop (AP-clamp) ISO effects 110

Role of the SaD in determining ISO effects on APD 111

CONCLUSION 113

CHAPTER 7 - USE OF DYNAMIC – CLAMP TO ANALYSE THE AUTONOMIC MODULATION OF THE AP 115

ABSTRACT 117

INTRODUCTION 118

METHODS 119

Cell preparation 119

Experimental Setup 119

Protocols 121

Data processing and statistical analysis 123

RESULTS 124

DISCUSSION 127

CONCLUSIONS 128

CONCLUSION 133

LIST OF PUBLICATIONS 135

APPENDIX A 137

APPENDIX B 153

APPENDIX C 171

CHAPTER 1

Basic concepts on cardiac electrophysiology and mathematical modeling

Cardiac Electrophysiology

The cardiac cell is a complex biological system where various processes interact to generate electrical excitation (the action potential, AP) and contraction. During AP generation, membrane ion channels interact nonlinearly with dynamically changing ionic concentrations and varying transmembrane voltage, and are subject to regulatory processes. In recent years, a large body of knowledge has accumulated on the molecular structure of cardiac ion channels, their function, and their modification by genetic mutations that are associated with cardiac arrhythmias and sudden death. However, ion channels are typically studied in isolation (in expression systems or isolated membrane patches), away from the physiological environment of the cell where they interact to generate the AP. A major challenge remains the integration of ion-channel properties into the functioning, complex and highly interactive cell system, with the objective to relate molecular-level processes and their modification by disease to whole-cell function and clinical phenotype.

Cardiac muscle can generate propagating electrical impulses (action potentials), a property that classifies it as an excitable tissue similar to skeletal muscle and nerve. At the single-cell level, the electrical action potential (AP) triggers mechanical contraction by inducing a transient rise of intracellular calcium which, in turn, carries the contraction message to the contractile proteins of the cell. This process that couples electrical excitation to mechanical function is termed excitation-contraction coupling. APs are generated by individual cells and are conducted from cell to cell through intercellular gap junctions, forming waves of excitation that activate and synchronize the blood pumping action of the heart. Similar to nerve and skeletal muscle, AP initiation and conduction in cardiac ventricular tissue rely mostly on a single membrane process, namely the flow of sodium ions through sodium-specific ion channels. However, unlike the short-duration APs of skeletal muscle and nerve, the cardiac ventricular AP is characterized by long plateau and repolarization phases that prevent premature arrhythmogenic excitation and provide control of mechanical contraction. In contrast to the ‘single-current mechanism’ of AP initiation, the plateau and repolarization phases rely on multiple ionic processes that provide precise control of the AP time-course and duration. In the cell, membrane ion channels interact with dynamically changing ionic concentrations and varying transmembrane voltage, and are subject to various regulatory processes. These interactions are nonlinear, making the single cardiac cell a complex interactive system where a high degree of synthesis and integration occurs. Because our intuition is mostly ‘linear’, our ability to predict the outcome of these multiple nonlinear

processes and to elucidate the underlying mechanisms is very limited. Analysis and synthesis of such complex nonlinear systems require mathematical approaches similar to those applied in other fields of science, notably physics and engineering.

Computational biology approaches can be used to simulate mutations and molecular interactions which require the formulation of single-channel models that represent specific channel states (e.g. open, closed, inactivated) and their interdependencies, and incorporation of these models into the model of the whole cell. This single-channel-based approach constitutes a major departure from the Hodgkin–Huxley scheme developed for the squid axon ([1]) and adopted in many cardiac cell models, where the starting point for computing the AP is macroscopic ionic currents through large ensembles of ion channels.

Cardiac action potential

The result of the action of the sarcolemmal ion currents is to cyclically change the transmembrane potential. This is known as the action potential (AP). Whereas there is a large degree of heterogeneity between the morphologies of the APs in different regions, they can none the less be described within the same framework. This consists of labelling distinct phases of the AP. Each phase corresponds to the action of one or more of the sarcolemmal ion currents. A labelled schematic of a cardiac action potential for a myocyte is shown in Figure 1.1.

The resting potential (RP) of the AP is the potential at which the membrane would remain if it were not perturbed. This is labelled as Phase 4 and is negative, usually between -70 and -85 mV. Potentials in this range and more negative are referred to as hyperpolarized. The RP is largely determined by I_{K1}, I_{NaCa} and background currents [2]. A supra-threshold electrical stimulus applied to the myocyte then initiates a fast upstroke known as Phase 0. This is called a depolarization as its action is to make the transmembrane potential less negative. It is primarily a result of the fast influx of Na^+ ions carried by I_{Na}. I_{Na} then quickly inactivates, and the transient outward potassium current, I_{to}, becomes active causing a small negative deflection in the AP. This is known as Phase 1 repolarization (repolarization because it acts to make the V_m more negative again) and is also referred to as the notch. Following this, I_{CaL} and other K^+ currents (e.g. I_{Ks}, I_{Kur}) all activate and this balance of inward and outward currents results in a plateau, corresponding to Phase 2. After some time, I_{CaL} inactivates and the potassium currents act to fully repolarize the AP back to the RP. This is Phase 3 or terminal repolarization. The negative RP deactivates the potassium channels and hence the AP is

returned to the stable phase 4 until another stimulus is applied or received. The large degree of electrophysiological heterogeneity observed in the heart manifests as different morphologies of the AP. These differences can take the form of different upstroke velocities during phase 0, the prominence of the notch in phase 1, the length and shape of the plateau in phase 2, the gradient of repolarization in phase 3 and the RP itself in phase 4. Heterogeneities are a result of the differing relative magnitudes of each current with respect to the others. For example, a myocyte which has a higher expression of I_{CaL} is likely to have a more pronounced and longer plateau than a myocyte with a lower expression of I_{CaL}, and one with a greater expression of I_{K1} will have a more negative RP.

The morphology of the AP associated with the pacemaker myocytes which have the ability to spontaneously depolarise have some marked differences to that of the working myocardium (Figure 1.1B). Never-the-less, they can still be described within the same framework. They tend not to reach as negative a potential as that of the working myocardium, reaching the most negative in a region of -50 to -60 mV. This is partly due to a lower expression of I_{K1} but also due to the presence of the inward current I_f. Phase 4 of the AP is no longer stable and hence it has less meaning to denote it a 'resting potential'. Instead, I_f and I_{CaT} act to slowly depolarize the potential (section 0). The gradient of the upstroke during phase 0 is significantly shallower due to a lower expression of I_{Na}. They have a distinct lack of a phase 1 notch or flattening during the phase 2 plateau. Instead, phase 3 directly follows phase 0.

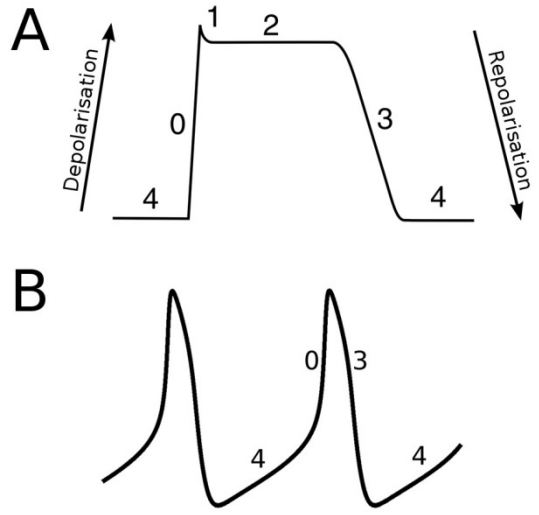

Figure 1.1. A. The phases of an action potential from the working myocardium. The numbers correspond to the phases referred to in the text. The direction of deflections known as depolarizations and repolarizations are indicated by the arrows. **B**. Phases of a spontaneously depolarizing action potential. Not all phases are present in this form of action potential.

Proarrhythmic marker: Action Potential Duration

Action potential duration (APD) is the length of the AP. It is usually measured between the onset of the AP upstroke and the point at which the cell repolarizes to a certain fraction of the maximum repolarization, e.g., APD_{50} refers to the APD measured at 50% repolarization and APD_{90} to the APD at 90% repolarization. APD is related to the length of the interval between successive cardiac impulses. When heart rate increases (the interval between successive impulses decreases), repolarization is faster. Also, the AP is shorter in duration. As heart rates slowdown, the APD lengthens [3]. This rate-dependent behavior of AP in cardiac cell is called “AP adaptation” [4].

There is a significant species- and region- dependent heterogeneity of APD. In rodent animals, such as mouse and rat, APD is normally less than 100 ms due to the significant early repolarization. In large mammals, the endocardial cells (the inner layer of the ventricular wall) have a longer APD than epicardial cells (the outer layer of the ventricular wall); while midmyocardial cells (M cells; cells between epicardium and endocardium) have the longest APD due to the small I_{Ks} [5].

It is important to maintain APD within physiological range to maintain normal electrical function of cardiomyocytes. The shorter APD of epicardium affords the normal sequence of repolarization from epicardium to endocardium, a direction that is opposite to the excitation sequence from endocardium to epicardium. It is believed that such a sequence prevents back-propagation of excitation from epicardium to endocardium, and thus protects against reentrant arrhythmias. In addition, if the APD is too short, the heart is susceptible to tachycardia or fibrillation, while if it is too long, it frequently results in early afterdepolarizations (EADs) and Torsade de pointe (TdP) type of arrhythmias [6].

APD is determined by the interplay between depolarizing and repolarizing currents that form the AP. As the depolarizing currents overpower the repolarizing currents, APD will be prolonged; as repolarizing currents overpower depolarizing currents, APD will be shortened. In many cardiac diseases, APD undergoes significant changes due to ionic remodelings.

APD prolongation in heart failure

Heart failure (HF) is a condition in which with the heart can no longer supply sufficient blood flow to meet the body's needs. HF is the end phase of many cardiovascular diseases, and is one of the leading causes of death [7]. The pathophysiology of HF is complex, but is

usually with three common features, including prolongation of the APD [8], progressive reduction of basal cardiac contractility [9], and loss of inotropic reserve [10].

One of the most consistent and significant electrical changes in failing hearts is the prolongation of APD, as it was found in HF patients and multiple animal HF models. For example, Beuckelmann and colleagues reported that, in end-stage HF patients (n =16), APD in myocytes was significantly prolonged by 60% (APD_{90}, 1038 ± 223 msec vs. 649 ± 101 msec) [11]. In a fast pacing heart failure canine model, APD_{90} ranges from 842 ± 56 ms to 1097 ± 73 ms, which is remarkably longer than a normal APD_{90} (usually < 400 ms; [12]). APD prolongation predisposes the heart to arrhythmias and sudden cardiac death [6]. Therefore, understanding the underlying mechanism of APD prolongation in diseased cardiomyocytes is critical for developing future treatment or prevention of arrhythmic events. Extensive efforts have been made to study, both experimentally and theoretically, the mechanism of APD prolongation. Generally speaking, it is caused by increases in the inward depolarizing current, and/or decreases in the outward repolarizing currents. However, the specific contribution of individual current to the APD prolongation is not fully understood.

HF is associated with many ventricular ionic changes that may predispose to arrhythmias and lead to APD prolongation (for review, see [13]). Both the fast and slow component of delayed rectifier K^+ current (I_{Ks} and I_{Kr}) were also found to be down-regulated in failing hearts ([14, 15]), which may contribute to the prolongation of APD.

Cardiac Modelling

The heart is a complex, nonlinear system with numerous interacting components and a high degree of synthesis and integration. Since human intuition subsides in face of these complexities, it is virtually impossible to predict perturbations to this complex system by reasoning alone. Because of this, the field cardiac electrophysiology has a rich history of computational approaches to promote the understanding of various mechanisms, including arrhythmogenesis. The interaction between experimental and computational cardiology started in the early 1960s and thanks to the advent of more powerful computing hardware, the field has grown ever since.

Cardiac modelling refers to the development of mathematical and computational models of the heart, which can assist in understanding the mechanisms underlying its function. It involves multi – scale integrative approaches: models must first be developed of single

cardiac myocytes; these can then be incorporated into 1D and 2D idealized models; anatomically accurate geometries can be created from clinical images and the myocyte models incorporated into these to provide detailed models of the heart at organ level. One advantage of cardiac modelling is to be able to investigate the effects of a change at the smallest scale on the overall behavior at organ level. This can be difficult experimentally as extracted myocytes, to which alterations may have been made, cannot then be placed back into tissue. Mathematical modelling also provides a significantly greater level of control over the variables than experimental techniques. It is not always possible, for example, to separate an individual ionic current from another one carried by the same type of ion. Similarly, the presence of a high level of complexity in biological systems, in which compensatory mechanisms are often in place, can make it very difficult to dissect the exact function of one particular aspect. Mathematical modelling is also, in general, much cheaper than experimental techniques. There is far less instrumentation which need be purchased, nor is there the need to purchase consumable products, such as animal tissue or solutions. Computational models do of course have their own limitations. The development of models requires simplifications of the system and assumptions must be made in order to do this.

Clinical experiments are further and further finding deeper complexities within systems, and currently computational models take into account only a small amount of this complexity. Certainly, models must be compared to experimental data to show that the simplifications and assumptions are valid. The development of the models also relies heavily on empirical data to begin with. It is therefore the combination of computational modelling and experimental techniques which provides the best framework with which to investigate the function of biological systems. Computational models of cardiac electrophysiology and the close interplay between model development and experimentation enabled us to achieve a quantitative understanding of the integrative behavior of the cardiac myocyte in health and disease. The potential of numerical modelling has been also recently acknowledged by pharmaceutical industry, and the US Food and Drug Administration has recently announced inclusion of *in-silico* methods in a new paradigm for drug safety assessment [8].

The Hodgkin–Huxley formalism for computing the action potential

The first computational model of the AP was formulated by Hodgkin and Huxley for the axon. Their circuit model of the cell membrane remains the basis for many modern neuronal and cardiac AP models. In collaboration with Katz, Hodgkin and Huxley made a fundamental

stride in characterizing voltage-dependent conductance changes in excitable cells by applying the voltage-clamp technique to the nerve axon [1]. These experiments suggested that inward movement of Na^+ is responsible for the strong positive deflection observed in intracellular recordings of the membrane potential, V_m, upon depolarization [16], while outward flow of K^+ causes repolarization to the resting, hyperpolarized state. Intrigued by these results, Hodgkin and Huxley constructed a mathematical model to test whether these fluxes could generate the AP morphology that they had recorded [1]. The framework for this model is described by the circuit diagram in Figure 1.2.

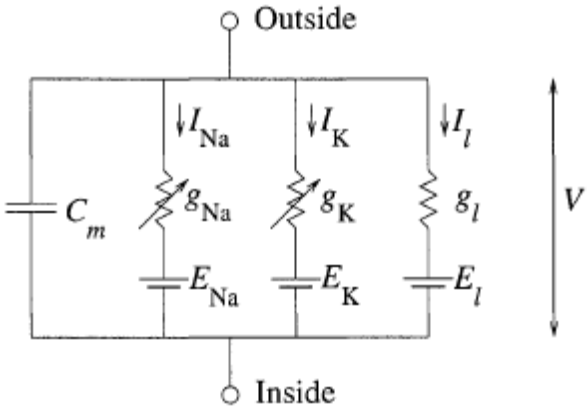

Figure 1.2. Schematic representation of cell membrane as an electrical circuit. Adapted from Hodgkin and Huxley [1].

Represented by the circuit are Na^+, K^+ and leakage currents as well as the capacitive effect of the membrane, which is a result of its hydrophobic nature that makes it impermeable to charged ions. This capacitance provides charge separation so that changes in V_m are due to charge displacement caused by the ionic currents and can be described by the following equation:

$$\frac{dV_m}{dt} = -\frac{1}{C_m} I_{ion}$$

where C_m represents the membrane capacitance and I_{ion} is the sum of all the ionic currents. This equation assumes space-clamp conditions and absence of external stimulus. Cell capacitance per unit area of membrane and current densities are typically used to calculate Vm, to normalize for variability in cell size.

The generic ionic current flowing through the membrane is represented as

$$I = x^a \cdot y^b \cdot G_{max} \cdot (V_m - E_r)$$

where $x(t, V_m)$ and $y(t, V_m)$ represent the activation and inactivation gating variables respectively, G_{max} is the maximum conductance and E_r the resting potential for the specific ioni computed as the Nerst potential:

$$E_r = \frac{RT}{zF} \cdot \ln \frac{[ion]_o}{[ion]_i}$$

The generic gating variable $x(t, V_m)$ ca be expressed in two equivalent forms. The first formulation is

$$\frac{dx}{dt} = \alpha_x(1 - x) - \beta_x x$$

Highlights the meaning of x and $(1 - x)$ as the fractions of open and closed channels respectively, in order to reproduce the transitions from the closed state to the open and vice-versa. If the values of either α_x or β_x depend on V_m, then the state of the gate is voltage-dependent as well as time-dependent. By imposing

$$\alpha_x = \frac{x_\infty}{\tau_x} \quad \text{and} \quad \beta_x = \frac{1 - x_\infty}{\tau_x}$$

the gating variable can be reformulated as

$$\frac{dx}{dt} = \frac{x_\infty - x}{\tau_x}$$

in order to highlight the dynamic sense of the gating variable $x(t, V_m)$. The steady-state

$$x_\infty = \frac{\alpha_x}{\alpha_x + \beta_x}$$

represent the value to which x tends at a certain voltage and it is usually obtained by fitting the experimental data using a sigmoid function

$$x_\infty = \frac{1}{1 + e^{\frac{V_m - V_h}{s}}}$$

where V_h is the voltage of half activation and s is the gradient of activation. The time constant

$$\tau_x = \frac{1}{\alpha_x + \beta_x}$$

means how fast the gating variable x reaches its steady state x_∞.

Cardiac action potential models

The first cardiac AP models were formulated by McAllister et al. [17], of the Purkinje fiber, and Beeler & Reuter [18], of the ventricular myocyte. These models relied on the Hodgkin–Huxley formalism to describe the ionic currents, and similar to the Hodgkin–Huxley model assumed that intracellular ion concentrations ($[Na^+]_i$, $[K^+]_i$) remain constant during the AP. However, in cardiac myocytes, entry of Ca^{2+} through $I_{Ca(L)}$, the L-type calcium channel, causes a dramatic change in its intracellular concentration, mostly by triggering Ca^{2+} release from the sarcoplasmic reticulum (SR) via the calcium-induced calcium-release (CICR) process [19]. Incorporation of dynamic changes in $[Ca^{2+}]_i$ was necessary to reproduce AP morphology even in the earliest ventricular cell models (e.g. the Beeler–Reuter model [18]).

Changes in $[Na^+]_i$ and $[K^+]_i$ can also influence AP morphology over time if cells are paced at fast rate. The first model to incorporate detailed information regarding dynamic concentration changes of these ions during the AP was the DiFrancesco–Noble model of the Purkinje fiber AP [20]. Rasmusson et al. [21] developed a similar model for a bullfrog atrial cell. The Luo–Rudy dynamic (LRd) model of the guinea pig ventricular AP formulated these processes for the ventricular guinea-pig myocyte [22] (Figure 1.3).

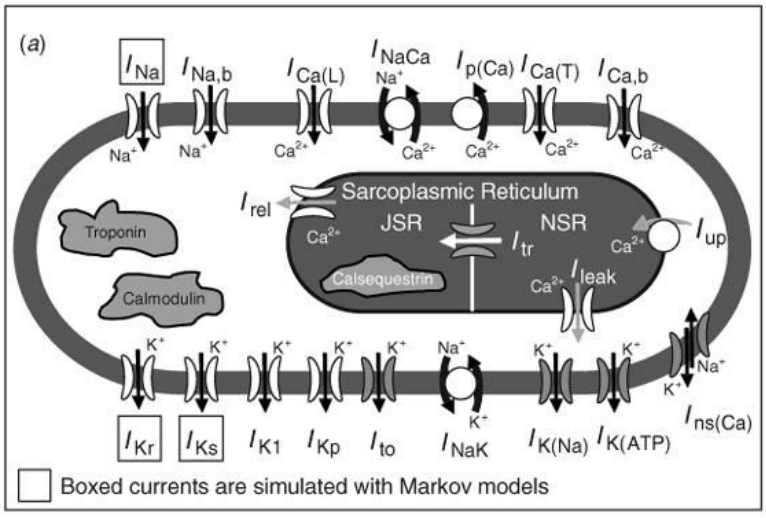

Figure 1.3: A schematic of the Luo–Rudy dynamic (LRd) ventricular cell model. The model is based mostly on data from the guinea pig. Figure from [23].

These models were founding members in a new class of 'second-generation' models that account for dynamic ion concentration changes. Several such models of the ventricular and atrial AP in different species have been published since that time ([2, 21, 24-28]).

Simulation of changes in intracellular ion concentrations requires incorporation of the pumps and exchangers that maintain resting levels (Figure 1.3). The primary pump is the

Na^+/K^+ ATPase (NaK) that converts energy produced by the metabolic system into potential energy (in the form of transmembrane ion concentration gradients) that is used to generate the AP. Extrusion of Na^+ and accumulation of intracellular K^+ by NaK generates a high $[K^+]_i$ and maintains a low $[Na^+]_i$ relative to the extracellular space. The Na^+/Ca^{2+} exchanger, NCX, uses the sodium gradient created by NaK to extrude Ca^{2+} and together with uptake into the SR, maintain a very low resting intracellular concentration $[Ca^{2+}]_i$. Under certain pathological conditions (e.g. reduced NaK capacity), during continual fast pacing, these gradients can become depleted, because the cumulative amount of ions carried by transmembrane current during repetitive APs surpasses the ability of pumps and exchangers to maintain resting concentrations. These changes can have important physiological consequences. Under pathological conditions of $[Na^+]_i$ overload, for example, depolarization slows, the AP duration (APD) shortens, and the inducibility of arrhythmia increases [29].

References

[1] Hodgkin AL, Huxley AF. A quantitatibe description of membrane current and its application to conduction and excitation in nerve. The Journal of physiology 1952;117:500-44.

[2] Courtemanche M, Ramirez RJ, Nattel S. Ionic mechanisms underlying human atrial action potential properties: insights from a mathematical model. American Journal of Physiology 1998;275:301-21.

[3] Woods SL. Cardiac nursing. Philadelphia: Lippincott Williams & Wilkins; 2005.

[4] Decker KF, Heijman J, Silva JR, Hund TJ, Rudy Y. Properties and ionic mechanisms of action potential adaptation, restitution, and accommodation in canine epicardium. Am J Physiol Heart Circ Physiol 2009;296:1017-26.

[5] Liu DW, Antzelevitch C. Characteristics of the delayed rectifier current (IKr and IKs) in canine ventricular epicardial, midmyocardial, and endocardial myocytes. A weaker IKs contributes to the longer action potential of the M cell. Circ Res 1995;76:351-65.

[6] Carmeliet E. Action potential duration, rate of stimulation, and intracellular sodium. J Cardiovasc Electrophysiol 2006;17.

[7] Piacentino Vr, Weber CR, Chen X, Weisser-Thomas J, Margulies KB, Bers DM, et al. Cellular basis of abnormal calcium transients of failing human ventricular myocytes. Circ Res 2003;92:651-8.

[8] Sager PT, Gintant G, Turner JR, Pettit S, Stockbridge N. Rechanneling the cardiac proarrhythmia safety paradigm: a meeting report from the Cardiac Safety Research Consortium. American Heart Journal 2014;167:292-300.

[9] Mason DT, Spann JFJ, Zelis R, Amsterdam EA. Alterations of hemodynamics and myocardial mechanics in patients with congestive heart failure: pathophysiologic mechanisms and assessment of cardiac function and ventricular contractility. Prog Cardiovasc Dis 1970;12:507-57.

[10] Bristow MR, Ginsburg R, Minobe W, Cubicciotti RS, Sageman WS, Lurie K, et al. Decreased catecholamine sensitivity and betaadrenergic-receptor density in failing human hearts. N Engl J Med 1982;307:205-11.

[11] Beuckelmann DJ, Nabauer M, Erdmann E. Alterations of K+ currents in isolated human ventricular myocytes from patients with terminal heart failure. Circ Res 1993;73.

[12] Kaab S, Nuss HB, Chiamvimonvat N, O'Rourke B, Pak PH, Kass DA, et al. Ionic mechanism of action potential prolongation in ventricular myocytes from dogs with pacing-induced heart failure. Circ Res 1996;78:262-73.

[13] Nass RD, Aiba T, Tomaselli GF, Akar FG. Mechanisms of disease: ion channel remodeling in the failing ventricle. Nat Clin Pract Cardiovasc Med 2008;5:196-207.

[14] Li GR, Lau CP, Leung TK, Nattel S. Ionic current abnormalities associated with prolonged action potentials in cardiomyocytes from diseased human right ventricles. Heart Rhythm 2004;1:460-8.

[15] Tsuji Y, Opthof T, Kamiya K, Yasui K, Liu W, Lu Z, et al. Pacing-induced heart failure causes a reduction of delayed rectifier potassium currents along with decreases in calcium and transient outward currents in rabbit ventricle. Cardiovasc Res 2000;48:300-9.

[16] Hodgkin AL, Huxley AF. Action potentials recorded from inside a nerve fibre. Nature 1939;144:710-1.

[17] McAllister RE, Noble D, Tsien RW. Reconstruction of the electrical activity of cardiac Purkinje fibres. Journal of Physiology 1975;251:1-59.

[18] Beeler GW, Reuter H. Reconstruction of the action potential of ventricular myocardial fibres. Journal of Physiology 1977;268:177-210.

[19] Fabiato A. Two kinds of calcium-induced release of calcium from the sarcoplasmic reticulum of skinned cardiac cells. Advances in Experimental Medicine and Biology 1992;311:245-62.

[20] DiFrancesco D, Noble D. A model of cardiac electrical activity incorporating ionic pumps and concentration changes. Philosophical Transactions of the Royal Society B: Biological Sciences 1985;307:353-98.

[21] Rasmusson RL, Clark JW, Giles WR, Robinson K, Clark RB, Shibata EF, et al. A mathematical model of electrophysiological activity in a bullfrog atrial cell. American Journal of Physiology 1990;259:370-89.

[22] Luo CH, Rudy Y. A dynamic model of the cardiac ventricular action potential. I. Simulations of ionic currents and concentration changes. Circulation Research 1994a;74:1071–96.

[23] Rudy Y, Silva JR. Computational biology in the study of cardiac ion channels and cell electrophysiology. Q Rev Biophys 2006;39:57-116.

[24] Hund TJ, Rudy Y. Rate dependence and regulation of action potential and calcium transient in a canine cardiac ventricular cell model. Circulation 2004;110:3168–74.

[25] Noble D, Varghese A, Kohl P, Noble P. Improved guinea-pig ventricular cell model incorporating a diadic space, IKr and IKs, and length- and tensiondependent processes. Canadian Journal of Cardiology 1998;14:123-34.

[26] Nygren A, Fiset C, Firek L, Clark JW, Lindblad DS, Clark RB, et al. Mathematical model of an adult human atrial cell : the role of K+ currents in repolarization. Circulation Research 1998;82:63-81.

[27] Priebe L, Beuckelmann DJ. Simulation study of cellular electric properties in heart failure. Circulation Research 1998;82:1206-23.

[28] Shannon TR, Wang F, Puglisi J, Weber C, Bers DM. A mathematical treatment of integrated Ca dynamics within the ventricular myocyte. Biophysical Journal 2004;87:3351–71.

[29] Faber GM, Rudy Y. Action potential and contractility changes in [Na(+)](i) overloaded cardiac myocytes: a simulation study. Biophysical Journal 2000;78:2392–404.

CHAPTER 2

Computational analysis of ventricular repolarization: classical approach investigating Short QT Syndrome

---

The content of this chapter has been submitted to:

Moreno C, Oliveras A, Muñoz C, de la Cruz A, **Bartolucci C**, Salar E, Gimeno-Blanes JR, Severi S, Felipe A, Lambiase P, Valenzuela C

New KCNQ1 mutation responsible of short QT syndrome located at the S5 segment

Abstract

Aims *KCNQ1 encodes $K_v7.1$, a pore-forming subunit of the cardiac outward potassium current, I_{Ks}. KCNQ1 mutations are associated with long and short QT syndrome. The aim of this study was to characterize the biophysical and cellular phenotype of a KCNQ1 missense mutation, F279I, found in a 23 years old man with a QTc of 356 ms and a family history of sudden cardiac death (SCD).*

Methods and Results *Experiments were performed using perforated patch-lamp, western blot, coimmunoprecipitation, biotinylation and immunocytochemistry techniques in HEK293, COS7 cells and in cardiomyocytes transfected with WT Kv7.1/KCNE1 or F279I Kv7.1/KCNE1 channels. In the absence of KCNE1, F279I Kv7.1 current exhibited less degree of inactivation than WT Kv7.1. Also, functional analysis of F279I Kv7.1 in the presence of KCNE1 revealed a negative shift in the activation curve and an acceleration of the activation kinetics leading to a gain of function in IKs. The co-assembly between F279I Kv7.1 channels and KCNE1 was markedly decreased compared with WT Kv7.1 channels revealed in coimmunoprecipitation experiments. All these effects contribute to the increased repolarization of IKs when channels incorporate F279I Kv7.1 subunits. A computer model simulation of these data predicts a shortening of the action potential consistent with the patient phenotype.*

Conclusion *The F279I mutation would predict a gain of function of I_{Ks} during the action potential due to an impaired coupling of the $K_v7.1$ gating modulation induced by KCNE1.*

Introduction

Approximately 10-20% of all sudden deaths do not exhibit structural cardiac abnormalities indicating a significant proportion can be due to electrical disorders. Mutations involving cardiac ion channels result in abnormal action potentials (AP), leading to cardiac arrhythmias. Major advances have occurred in the understanding of the molecular basis of inherited sudden cardiac death (SCD). With the contribution of molecular biology and electrophysiological studies, the genetic basis of numerous cardiac diseases has been established [1].

Short QT syndrome (SQTS) is a cardiac channelopathy associated with a predisposition to atrial fibrillation and SCD, established as a distinct clinical entity [2]. The patients have

structurally normal heart, but electrocardiography (ECG) exhibits abbreviated QTc intervals ranging from 248 to 300 ms (Bazett corrected QT, (QTc)). To date, 6 genes encoding ion channel subunits have been implicated in the pathogenesis of SQTS, and further genetic culprits are suspected [3-8]. SQT2 is caused by gain of function mutations in the *KCNQ1* gene encoding the alpha subunit of the $K_v7.1$ channel (I_{Ks}) [6]. In this study, we characterized the biophysical and cellular phenotype of a new *KCNQ1* mutation, F279I, found in a patient with SQTS.

Methods

An expanded Methods section is available online. The institutional review board at The Heart Hospital, Institute of Cardiovascular Science (London) approved the study, and the patient provided written informed consent. The study conforms with the Declarations of Helsinki.

Mutagenesis and Cell transfection

The F279I mutation was cloned in the pEYFP-N1-*KCNQ1* plasmid by PCR using mutant primers and the QuickChange II XL Site-Directed Mutagenesis Kit (Agilent Technologies) following manufacturer instructions. COS7 cells were transiently transfected with *KCNQ1*-YFP (WT, F279I or WT/F279I) and *KCNE1*-CFP by using Fugene6, following the manufacturer instructions (see Appendix A).

Preparation of cell extracts

For total protein extraction from HEK293, cells were washed twice (6-well dishes) with ice-cold PBS, they were homogenized and cell extracts were prepared (see Appendix A).

Western blot analysis

Samples of cell extracts containing equal amounts of protein were boiled in 250 mM Tris-HCl, pH 6.8, 2% SDS, 10% glycerol, 2% β-mercaptoethanol and size-separated in 10-15% SDS-

PAGE. Gels were blotted onto a Immobilon-P nitrocellulose membrane (Millipore) and processed as recommended by the antibodies supplier. Cell surface proteins biotinylation was carried out with Pierce Cell Surface Protein Isolation Kit (Pierce) following manufacturer's instructions (see Appendix A).

Confocal microscopy

Membrane location of the channel subunits in the cell membrane was assessed twenty-four hours after transfection of K_v7.1YFP or F279I K_v7.1YFP and KCNE1CFP and staining of plasma membrane with wheat germ agglutinin (WGA) linked with fluorescent dye Alexa 555 (Invitrogen) under non-permeabilizing or permeabilization conditions (see Appendix A).

Electrophysiological recordings

Currents were recorded from COS7 and HL-1 cells using the perforated amphotericin B-patch-clamp technique with an Axopatch 200B amplifier (Axon Instruments) as described [9-11] (see Appendix A).

Computational analysis

To estimate the effects of the mutation (F279I K_v7.1/KCNE1 and WT K_v7.1/F279I K_v7.1/KCNE1) on the action potential duration (APD) the Ten Tusscher-Panfilov (TTP) [12] and the O'Hara-Rudy (ORd) [13] models were used (see Appendix A).

Statistics

Results are presented as mean values±SEM. Two way ANOVA repetitive measurements test followed by Bonferroni test were used to assess statistical significance where appropriate. A value of $P<0.05$ was considered significant (see Appendix A).

Results

Patient characteristics: clinical analysis and genetics

The index case of the family was a 37 years old man who died unexpectedly whilst working as a postman. He had no history of syncope or other cardiac symptoms, and the information obtained from relative's interview did not demonstrate the cause of the death. Postmortem was performed and relatives were informed that it failed to identify the cause of the sudden death. Full report from post-mortem study was not available to review. His son, an athletic healthy 23 years old, was referred recently for cardiac evaluation. ECG showed sinus bradycardia (55bpm), normal PR, QRS, and slightly short QTc interval of 356ms with prominent T waves in V2-V4 (Figure 2.1A). Exercise test was normal of note; QTc shortened with the exercise, measuring 350ms at maximum workload. Echocardiogram and cardiac magnetic resonance demonstrated a normal heart, and 24-hour Holter monitoring showed no arrhythmias. Cardiac evaluation of the asymptomatic 13 years old daughter demonstrated normal ECG, Holter, exercise test, echocardiogram and cardiac magnetic resonance exhibiting a QTc was 400ms. A blood sample from the patient and his sister was sent for genetic study of most prevalent genes related to channelopathies. Genetic studies on the index case son's DNA excluded mutations in *KCNH2, KCNQ1, SCN5A, KCNE1, KCNE2, KCNJ2* and *RyR2*. Analysis of the *KCNQ1* gene revealed a novel heterozygous mutation, a single-base substitution at nucleotide 127910 (g.127910T>A) in the exon 6 of the *KCNQ1* gene, resulting in an amino acid change from phenylalanine to isoleucine at 279 in $K_v7.1$ (p.F279I) within the S5 transmembrane segment, which was not reported before (Figure 2.1B). Among the K_v7 family $K_v7.1$ is the unique channel carrying a phenylalanine at the equivalent position; suggesting that this residue might be important for the unique properties of the cardiac I_{Ks}. No other potential SQT mutations were identified and neither in his daughter or his mother (Figure 2.1C).

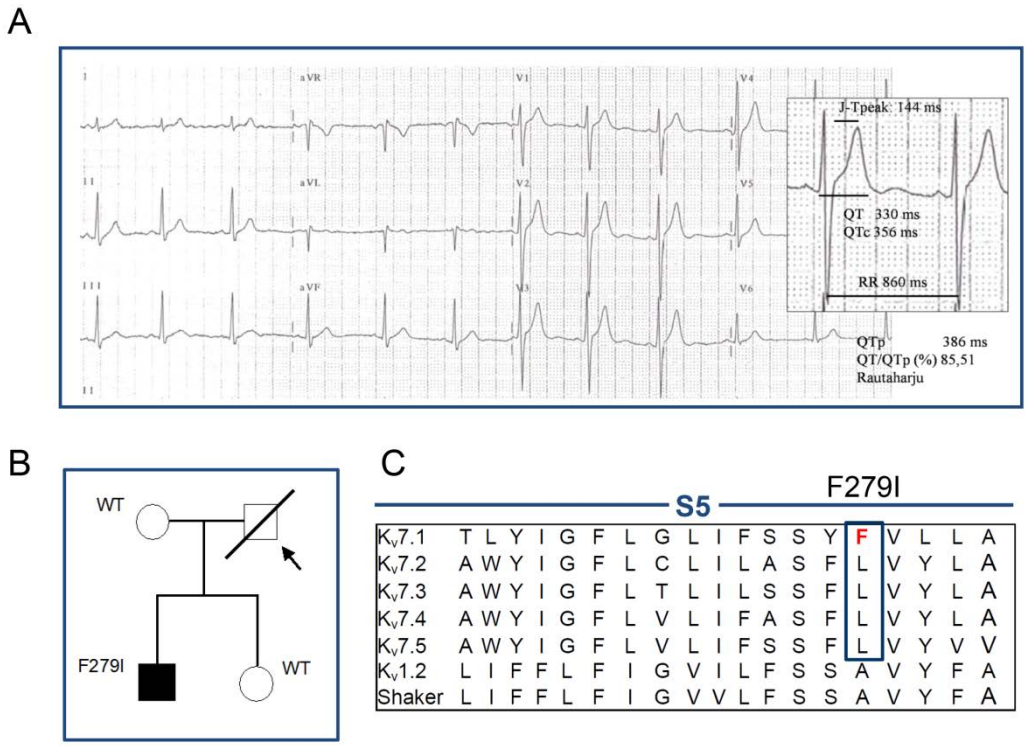

Figure 2.1. Electrocardiogram of the patient and genetic analysis

(A) Twelve-lead ECG of an affected individual (III-9). **(B)** Family pedigree. **(C)** Alignment of the amino acid sequence of $K_v7.1$, other K_v7 isoforms, $K_v1.2$ and *Shaker* channels missense mutation found in the patient.

Characterization of F279I Kv7.1 channels

The electrophysiology of F279I $K_v7.1$ channels was characterized after heterologous expression in COS7 cells. Currents were elicited by 5.5s pulses to potentials between -80mV and +100mV from a holding potential of -80mV in 20mV steps. WT and F279I $K_v7.1$ generated potassium currents that fully activate during the 5.5s pulse with an exponential kinetics (Figure 2.2A-B). Upon repolarization to -50mV, WT $K_v7.1$ tail currents displayed a hooked configuration while mutant channels did not, suggesting a decreased inactivation. The IV relationships plotted in Figure 2.2C show a gain of function of F279I $K_v7.1$ *vs.* WT $K_v7.1$ (~50% at potentials between 0mV and +40mV, $P<0.05$, n=8-9). Figure 2.2D shows the activation curves with V_h and s of V_h=-21.2±1.9mV, s=9.9±1.9mV *vs.* V_h=-22.9±1.9mV, s=8.1±0.5mV for WT and F279I $K_v7.1$ channels ($P>0.05$, n=9).

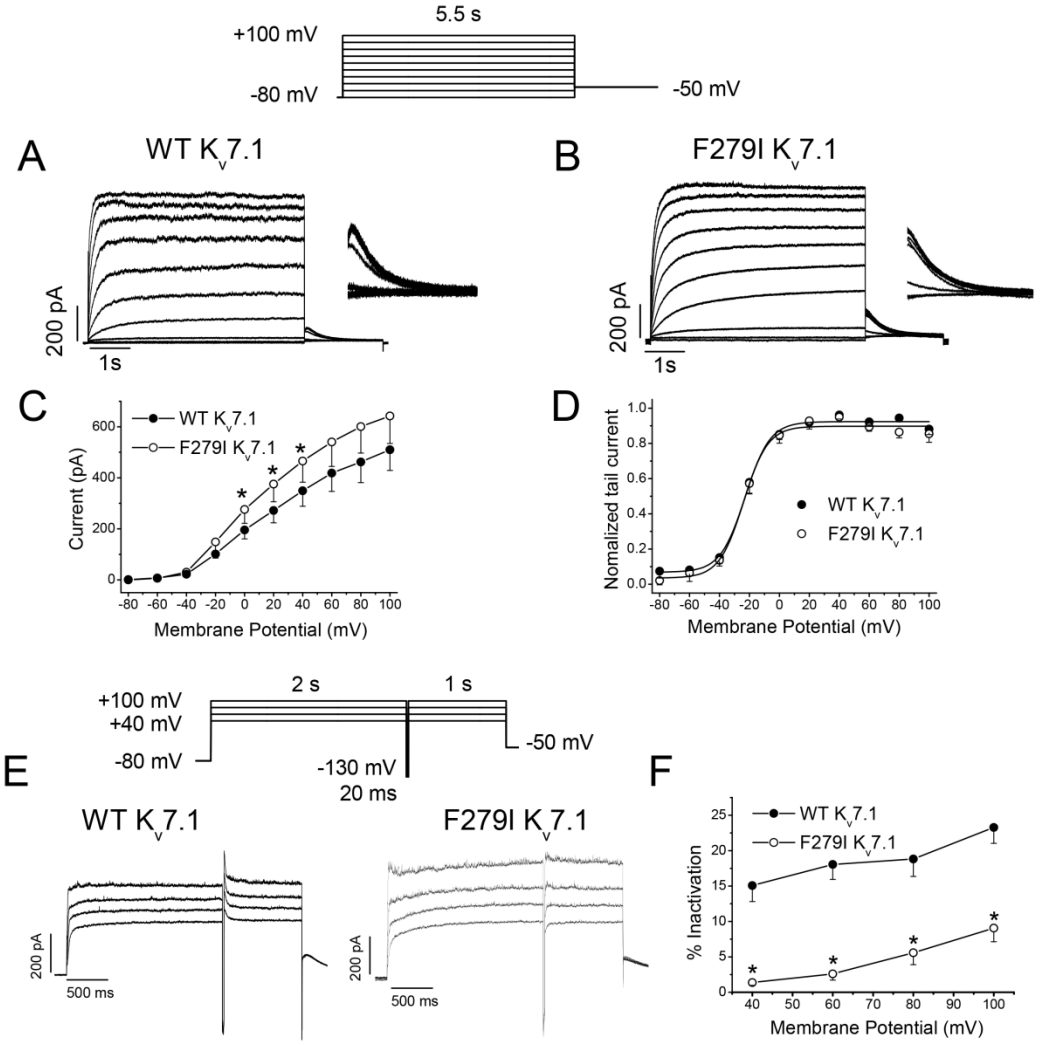

Figure 2.2. Electrophysiological characterisctics of WT and F279I K_v7.1 channels expressed in COS7 cells

Representative currents of WT **(A)** or F279I K_v7.1 **(B)**: after applying the pulse-protocol shown on the top. **(C)**: IV relationships of current measured at the end of a 5.5s depolarizing pulses for WT and F279I K_v7.1 channels. **(D)**: Activation curves obtained by plotting the normalized tail currents versus the membrane potential. **(E)** Cells were pulsed to a test potential of +40, +60, +80, or +100mV for 2s before applying a 20ms interpulse to -130 mV to allow channels to recover from inactivation. Membrane potential was returned to the test potential to measure the degree of inactivation **(F)**. *P<0.05, n=8-12.

Inactivation is reduced by the F279I mutation

Inactivation of WT K_v7.1 channels is indirectly revealed by the hooked tail currents [14, 15]. To investigate whether the gain of function of the F279I K_v7.1 channel could be explained by altered inactivation, we applied a triple-pulse protocol to measure the channel

inactivation (Figure 2.2E) [16]. Figure 2.2E shows traces obtained with this triple-pulse protocol, as well as the degree of inactivation at each potential (Figure 2.3F). Compared to WT, F279I K_v7.1 channels exhibited a decreased degree of inactivation at all potentials.

Mutations of residues within the pore region spanning S5 to S6 are crucial for K_v7.1 inactivation [17, 18], Similarly, the mutation V307L (responsible of SQTS) located in the pore loop showed slightly slowed activation and deactivation kinetics compared with WT, but again, abolished inactivation [19]. Therefore, a reduced level of inactivation could account for the greater steady-state current amplitude observed for the F279I K_v7.1 current.

Properties of the WT and F279I Kv7.1/KCNE1 complexes

Coexpression of WT K_v7.1 and KCNE1 subunits generate cardiac I_{Ks} [20]. To investigate the effects of the F279I in this physiologically relevant channel complex, either WT K_v7.1 or the mutant F279I subunit were co-transfected with KCNE1. The channel complex F279I/KCNE1 displayed ~1.8 fold acceleration of the fast component of the activation kinetics in comparison to the WT K_v7.1/KCNE1 complex (794.1±36.0ms *vs.* 445.7±27.9ms, $P<0.05$, n=8-9) being kinetically intermediate between WT K_v7.1 and WT K_v7.1/KCNE1 complexes. Furthermore, the initial sigmoidal activation, characteristic of WT K_v7.1/KCNE1 was absent (Figure 2.3A-B). This acceleration might be due to an impaired alpha-beta interaction. In fact, it has been described that substitutions at this residue by the smaller amino acid alanine, strongly disturbed the KCNE1 gating modulation [21]. However, the deactivation kinetics of the F279I/KCNE1 channels was similar to that of WT K_v7.1/KCNE1 complex (Appendix A, Figure S1).

The current generated after depolarizing F279I K_v7.1/KCNE1 channels measured at the end of a 5.5s depolarizing pulse was greater at potentials between -20 to +20mV, but this effect was reverted at potentials positive to +40mV (Figure 2.3C). Furthermore, the mutant channel starts to display accumulation of the current at potentials at around +80mV. This effect could be due to the presence of an inactivated state that according to the model of Silva and Rudy [22], is absent in WT K_v7.1/KCNE1, suggesting an impaired interaction with KCNE1 (Fig 7.4A-B). Current was also measured 300ms after the step change in membrane potential to more accurately reflect the duration of a cardiac AP (Figure 2.3D). The mutant current magnitude was greater at potentials positive to 0mV, likely due to the faster activation kinetics of F279I K_v7.1/KCNE1 current. The voltage dependence of channel opening for the mutant was shifted towards more negative potentials, without changes in the slope (Figure

2.3E, Appendix A Table S2). Altogether, the shift in the activation curve and the faster activation kinetics indicate that F279I K_v7.1/KCNE1 channels open faster and at more negative potentials than WT K_v7.1/KCNE1 channels.

In order to discern if different endeavors can modify the electrophysiological properties of these channels, other series of experiments in which WT K_v7.1/KCNE1 or F279I K_v7.1/KCNE1 were transfected in a mouse atrial cardiomyocyte tumor lineage, HL-1 cells were performed (provided by Dr. Lisardo Boscá). The results obtained under these conditions were mostly similar to those obtained in COS7 cells (Figures 7.3 and Appendix A, Figure S2) (Appendix A, Tables S1-S4). Similarly, F279I K_v7.1/KCNE1 current exhibited a faster activation and the midpoint of the activation curve was shifted to negative potentials by ~-40mV. Also, in the IV curves a greater magnitude of the F279I K_v7.1/KCNE1 current was observed at membrane potentials between -30 and +30mV and a decrease of the current at potentials positive to +60mV in comparison to WT K_v7.1/KCNE1.

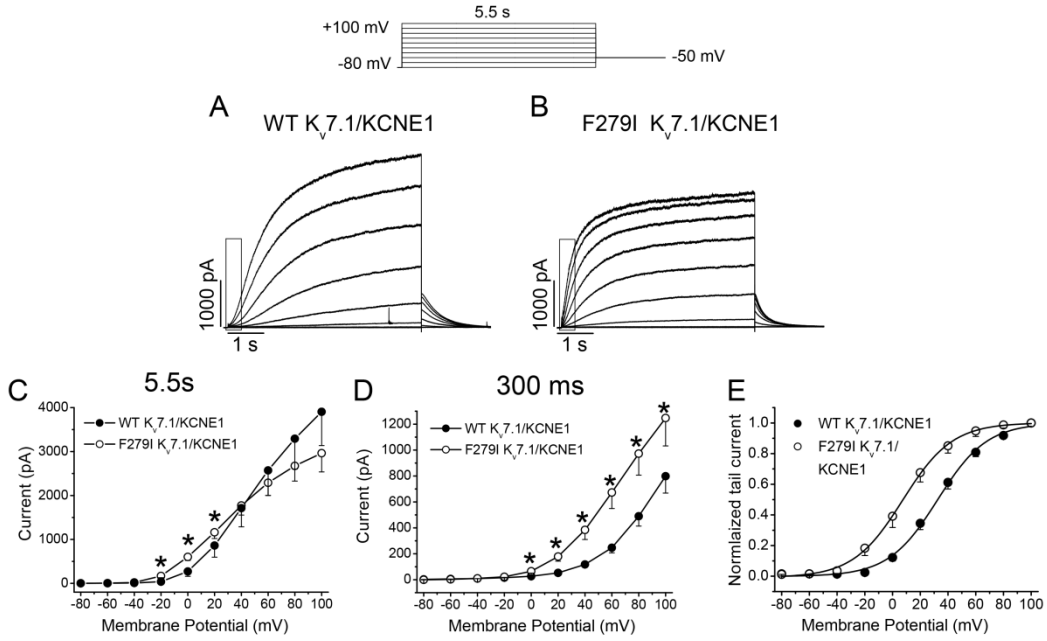

Figure 2.3. Currents induced by co-expression of KCNE1 with WT or F279I K_v7.1 channels in COS7

WT and F279I K_v7.1/KCNE1 currents records **(A-B)**. For panels A-B, pulses were applied from a holding potential of -80mV to +100mV in 20mV-steps. Tail currents were recorded at -50mV. IV relationships after plotting the current magnitude at the end of 5.5s **(C)** or after measuring the current at 300ms **(D)**. Voltage dependence of activation **(E)**. Activation curves were obtained by plotting the normalized tail current versus the membrane potential. *P<0.05 *vs.*WT K_v7.1/KCNE1, n=8-9.

Impaired interaction between F279I Kv7.1 and KCNE1 subunits

Our electrophysiological data revealed an altered interaction between F279I K_v7.1/KCNE1. Therefore, we tested the association between both subunits, we performed coimmunoprecipitation and FRET experiments in HEK293 cells. The co-assembly between F279I K_v7.1 channels and KCNE1 was markedly decreased compared with WT K_v7.1 channels as demonstrated by co-IP (Figure 2.4A-B) and FRET experiments in plasma membrane loans (PML) (Figure 2.4K-P). The membrane marker RhoPYC clearly identified PML preparations (Figure 2.4 C,D) and Kv7.1CFP/Kv7.1YFP (Figure 2.4E-G) and Kv7.1CFP/Kv1.5YFP (Figure 4H-J) colocalization in PML was used as positive and negative FRET controls respectively (Figure 2.4P). However, the traffic of F279I K_v7.1 to the membrane and the surface expression by biotinylation both, in the absence or in the presence of KCNE1, were not modified compared with that observed with WT K_v7.1 channels (Appendix A, Figure S3). All these results suggest that F279I K_v7.1 channels traffic similarly than WT to the membrane, but their assembly with KCNE1 is decreased.

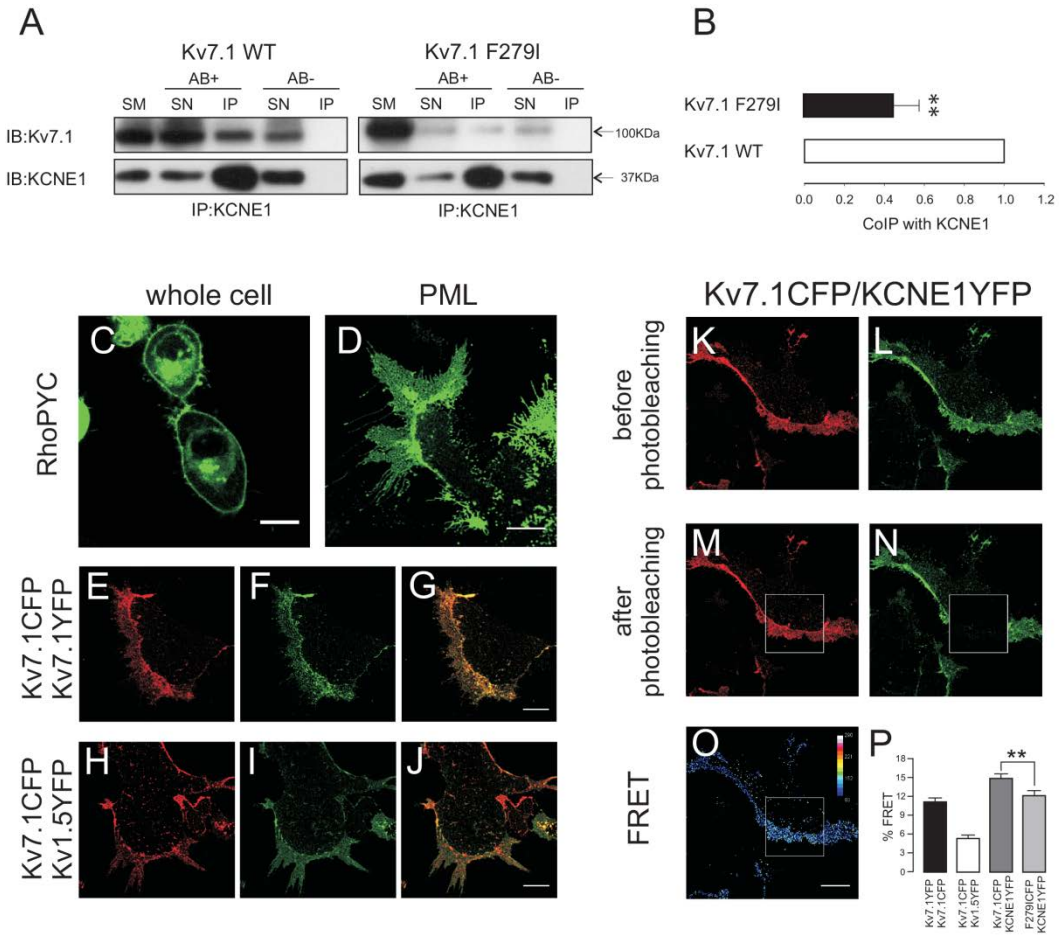

Figure 2.4. F279I K_v7.1 channels fail in assembly with KCNE1 subunits in HEK293 cells.

(A) HEK293 cells were transiently co-transfected with K_v7.1YFP and KCNE1CFP or F279I K_v7.1YFP and KCNE1CFP. Cells were lysed and total protein extracts were immunoprecipitated using anti-KCNE1. Left panel: immunoblot using anti-K_v7.1 and anti-KCNE1 demonstrating WT K_v7.1 (100 KDa arrow) co-immunoprecipitation with KCNE1 (37 KDa arrow). Right panel, shows how F279I K_v7.1 mutant co-immunoprecipitates to a lesser extent. AB+, immunoprecipitation in the presence of anti-KCNE1; AB-, immunoprecipitation in the absence of antibody; SM, starting material; SN, supernatant; IP, immunoprecipitated sample. **(B)** Percentage of K_v7.1, WT or F279I, co-immunoprecipitation related to the total amount of KCNE1 immunoprecipitated (n=4). **(C)** RhoPYC marker in whole cell targeted to the membrane. **(D)** RhoPYC staining PML. **(E-G)** K_v7.1CFP/ K_v7.1YFP colocalization in PML. **(H-J)** K_v7.1CFP/K_v1.5YFP colocalization in PML. **(K-O)** Representative K_v7.1CFP/KCNE1YFP FRET experiment in PML. K_v7.1CFP **(K)** and KCNE1YFP **(L)** before photobleaching. K_v7.1CFP **(M)** and KCNE1YFP **(N)** after photobleaching. Square indicates the area of analysis. Bars represent 10μm. **(P)** Percentage of FRET from different pairs tested. K_v7.1CFP/K_v7.1YFP and K_v7.1CFP/K_v1.5YFP were used as positive and negative controls, respectively. F279I K_v7.1/KCNE1 FRET values was lower than WT K_v7.1/KCNE1 ($P<0.01$, n=25-35 cells/group).

Rate-dependent increase in current upon depolarizing pulse trains

I_{Ks} is crucial for AP repolarization and for adaptation to changes in rate [23-25]. Slow activation of I_{Ks} ensures that the current activated by a single AP does not reach the maximal value and can be further increased upon a subsequent depolarization [22] leading to AP shortening in response to fast heart rate. Since F279I mutant resulted in faster activation kinetics, we investigated how these altered electrophysiological properties affected the rate dependent effects of I_{Ks}. To this end, we applied a stimulus train of 70 pulses to +50mV from -80mV at different frequencies (1, 2 and 2.5Hz) mimicking normal and fast heart rates (Figure 2.5A). As described for WT K_v7.1/KCNE1 channel complex a significant increase was observed at fast rates (2Hz and 2.5Hz) [22]. To quantify this increase, the instantaneous current amplitude was normalized to the steady state current amplitude reached with a single 5.5s depolarization to +50mV. When the same stimulus waveform was applied to cells expressing F279I K_v7.1/KCNE1 channels there was an increase in current at all frequencies tested, which did not reach its maximum level (Figure 2.5B).

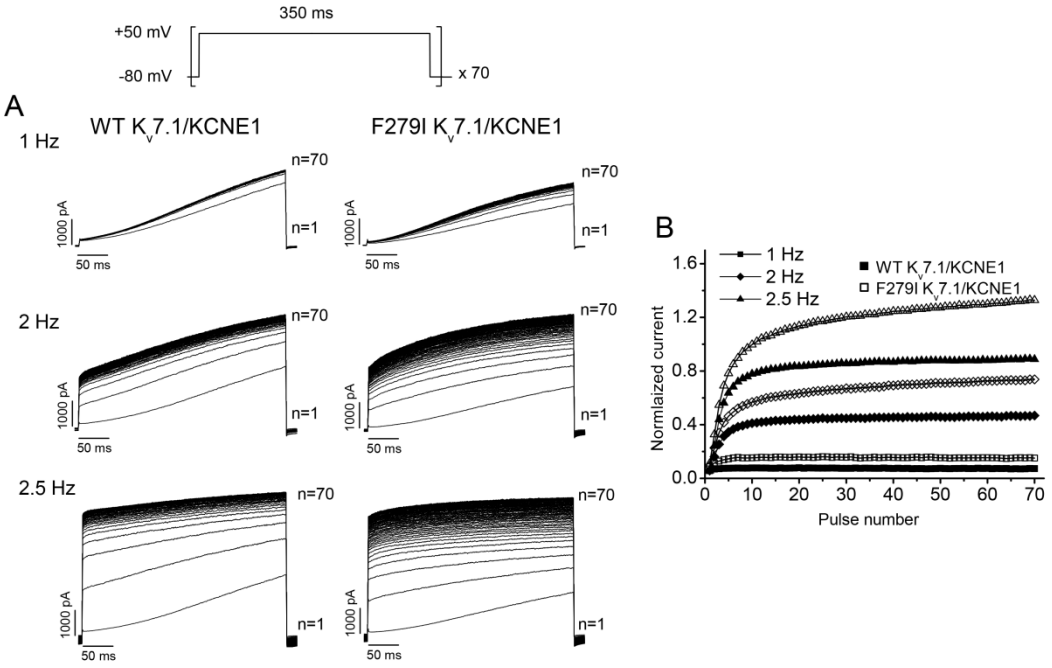

Figure 2.5. Rate dependent current increase for WT and F279I K_v7.1/KCNE1 channels

A: current recordings of WT and F279I K_v7.1/KCNE1 channels. The train-protocol is shown on the top. To normalize this increase in current, the instantaneous current amplitude was divided by the steady-state current amplitude at the end of 5.5 pulses to +50mV and plotted as a function of the pulse number **(B)**. n= 8-9.

Heterozygous condition

To mimic the heterozygous condition of the patient, co-expressions of WT and F279I K_v7.1 mutant channels in a 1:1 ratio together with KCNE1 were performed. WT/F279I K_v7.1/KCNE1 channel complexes, exhibited faster activation kinetics compared to WT K_v7.1/KCNE1 but slower than F279I K_v7.1/KCNE1 (Figure 2.6A, Appendix A: Table S1). Compared to WT K_v7.1/KCNE1 channels, the deactivation kinetics were faster for the heterozygous channel complex (Appendix A, Figure S1). The activation curve for the heterozygous channel exhibited an intermediate phenotype between the F279I K_v7.1/KCNE1 and WT K_v7.1/KCNE1 channel complexes (Figure 2.6B). The current magnitude for the heterozygous condition was also greater *vs.* WT K_v7.1/KCNE1 at the end of the 5.5s depolarizing pulse at potentials between 0 and +40mV and at every potential positive to -20mV when measured 300ms after the first voltage step ($P<0.05$; n=4-9) (Figure 2.6C). Finally, the rate-dependence increase of I_{Ks} was analyzed. At 1 and 2 Hz, a decrease in the normalized current was observed compared to WT K_v7.1/KCNE1 and a slower kinetic of increase. However, at 2.5Hz the rate-dependent increase in current for the WT/F279I K_v7.1/KCNE1 complexes was higher than those induce by WT K_v7.1/KCNE1 and it did not

reach the steady-state as it was noticed for F279I K_v7.1/KCNE1 channel complexes (Figure 2.6D-E). These data indicate that co-expression of the WT K_v7.1 together with the F279I subunit also results in a gain of function of $I_{Ks.}$

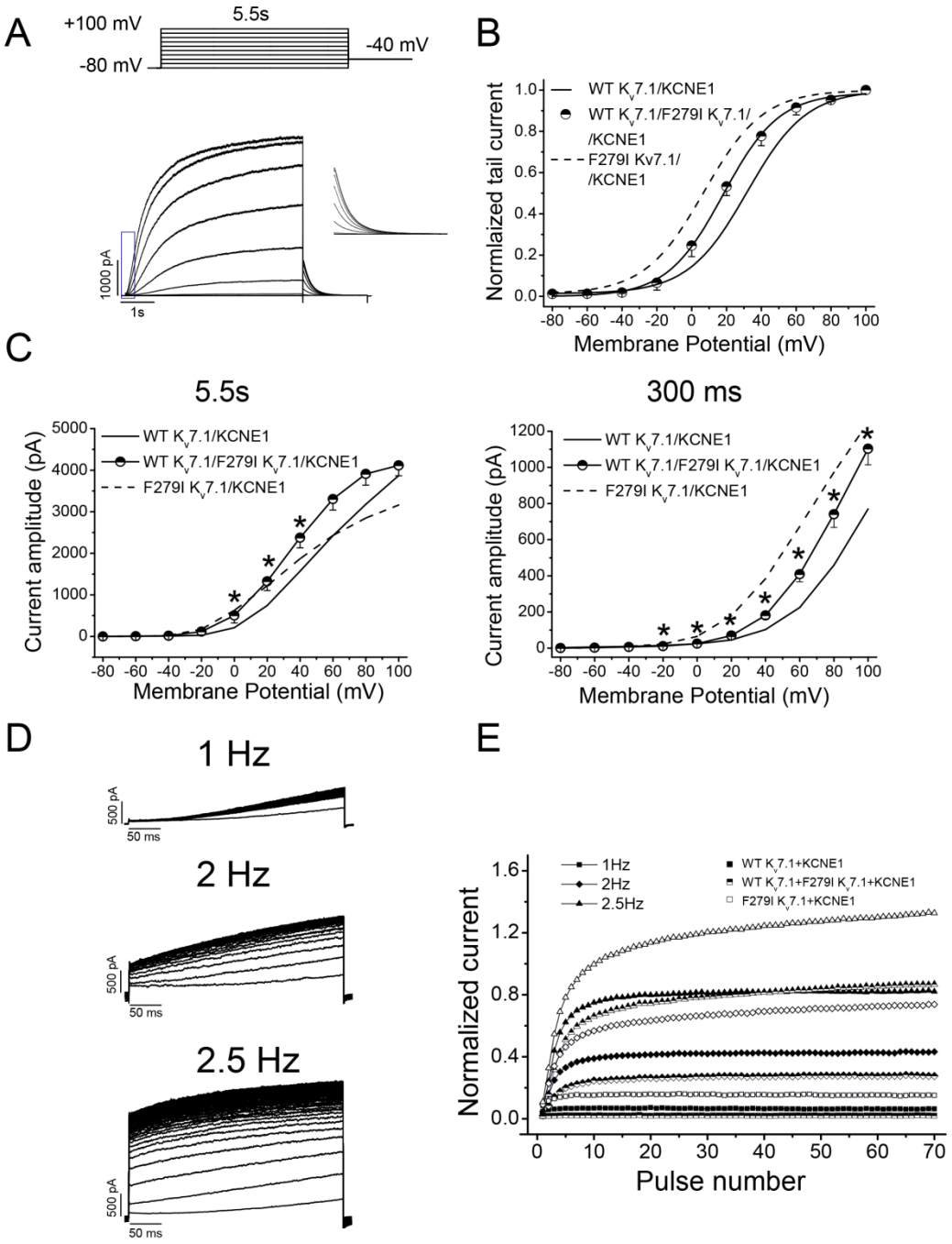

Figure 6. Electrophysiological properties of the heterozygous WT/F279 K_v7.1/KCNE1 channel complex in COS7 cells.

WT K_v7.1/F279I K_v7.1/KCNE1 current recordings **(A)**. Activation curves were obtained by plotting the normalized tail current versus the previous potential **(B)**. IV relationships obtained at the end of a 5.5s **(C)** depolarizing pulse or after 300ms **(D)**. Rate dependent current increase for WT K_v7.1/F279I K_v7.1/KCNE1

channels **(E-F)**. The train pulse protocol applied was the same described in Figure 6A. Results show the mean±SEM of 4-9 cells/ group. *P<0.05 *vs.* WT K_v7.1/KCNE1.

F279I mutation causes dramatic AP shortening in a ventricular cell model

The TTP ventricular cell computer model was used to examine the effects of mutant channels on AP morphology in epicardial, endocardial and M cells (Figure 2.7). Simulated I_{Ks} in the F279I K_v7.1/KCNE1 homozygous condition shortened the AP with respect to the WT one (from 300 to 194ms in endocardial cells, Figure 2.7A left). The F279I K_v7.1/KCNE1-induced AP shortening is due to the presence of a significant increase in the outward K^+ current during phases 3 of the AP (Figure 2.7A, lower panels). The F279I K_v7.1/KCNE1 channel did not induce significant additional changes in AP morphology with respect to WT K_v7.1/KCNE1. WT K_v7.1/F279I K_v7.1/KCNE1 also shortened the AP with respect to the WT condition, even though at a less dramatic extent (from 300 to 247ms in endocardial cells). When simulating the β-adrenergic stimulation, the APD behaviour was similar, as shown in Table S5 (Appendix A).

When introduced in the ORd model the mutation also induced APD shortening, but much less pronounced (Appendix A, Figure S3). APD reduction was almost negligible in basal conditions while it was enhanced by adrenergic stimulation (up to 23ms shortening in M cells, Appendix A: Figure S3B, right panel). The effect of the mutation on action potential duration is also present at faster stimulus frequencies, as shown by simulations performed at CL = 500 ms (Appendix A, Table S3).

Also, pseudo-ECG simulations are shown in Figure S4 8 (Appendix A). Consistently with AP simulations a dramatic reduction of the QT interval with respect to the WT condition can be observed when the TTP model is used. The QT shortening is accompanied by a large increase in T-wave amplitude, as also observed in a previous study, in which the channel kinetics of the V307L mutation of the KCNQ1 subunit of the I_{Ks} channel was incorporated into human ventricular AP models and into pseudo-ECG simulations [26]. When the ORd model is used, a QT reduction is also observed, even though it is significantly smaller than with the TTP model, and it is accompanied by a slight increase of the T amplitude. Notably, the impact of the mutation on the pseudo-ECG seems larger than those on the AP at the cellular level.

However, given the uncertainties in i) the electrophysiology of human ventricular

myocytes and, consequently, in mathematical models of such myocytes, ii) the real heterogeneity of human cardiac tissue (e.g. existence/amount/role of M cells and role of base to apex heterogeneity), iii) the mathematical description of the cardiac structure, electrical conduction and fiber orientation iv) the real relevance of pseudo-ECG *vs.* clinical ECG, tissue simulation results should be regarded as purely qualitative.

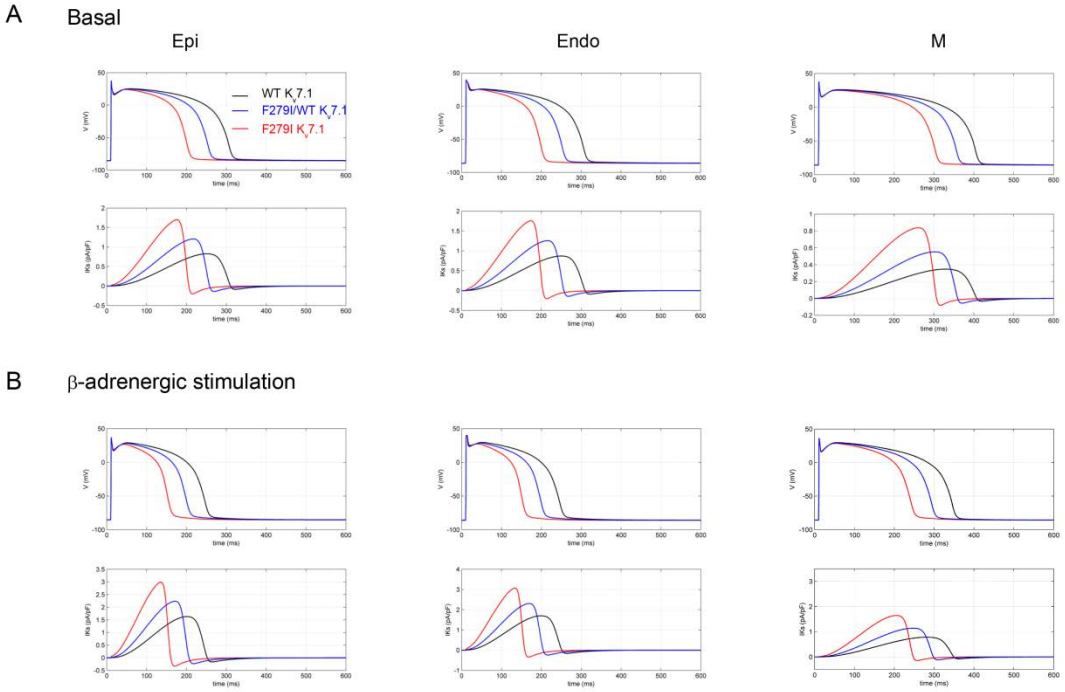

Figure 2.6. Computational analysis of F279I K_v7.1 effects on the ventricular action potential

(A) Comparison of ventricular action potentials (top) and I_{Ks} current (bottom) in wild-type (WT), F279I K_v7.1/KCNE1 and WT K_v7.1/F279I K_v7.1/KCNE1 conditions for epicardial (left), endocardial (middle), and M (right) cells (basic cycle length: 1,000ms), simulated using the TTP model. **(B)** Simulation of β-adrenergic stimulation in the same conditions as in **A** (note the different scale in lower panels showing I_{Ks} time course).

Discussion

K_v7.1 is the alpha subunit of the ion channel complex underlying I_{Ks} [20] that, together with I_{Kr}, are the major repolarizing current in ventricle [27]. Gain of function mutations on K_v7.1 cause SQT2. To date, three mutations associated with SQTS2 have been found: two at the S1 and another one at S6 of K_v7.1. In this study, the functional effects of the new missense mutation F279I on K_v7.1 found in a patient with a QTc interval of 356ms at resting and a family history of SCD were characterized. This mutation, located in the S5 transmembrane segment, modifies the gating of WT K_v7.1/KCNE1 complexes.

F279I K_v7.1 channel compared with WT K_v7.1, displayed slower activation kinetics and a reduced degree of inactivation, as it was shown by the lack of the initial hook in the tail current and by applying a three-pulse protocol. Structural basis of K_v7.1 for inactivation is not fully understood, but several reports indicate that mutations in the S5 have a profound effect on the voltage dependence of this process [17, 19, 28] and therefore, on the channel gating.

Co-assembly of F279I K_v7.1 with KCNE1 had a big impact on K_v7.1/KCNE1 current properties. The functional effects of KCNE1 are to: 1) modulate K_v7.1 kinetics (slower activation and slightly slower deactivation), 2) remove inactivation [20] and 3) increase current magnitude by enhancing the single channel conductance [29]. Compared with K_v7.1/KCNE1, F279I K_v7.1/KCNE1 current exhibited faster activation kinetics, increased current magnitude, a similar voltage dependence of activation and a small degree of inactivation. Therefore, the electrophysiological properties of the F279I Kv7.1/KCNE1 current are intermediate between K_v7.1 and K_v7.1/KCNE1 currents. These results suggest that the underlying mechanism by which this mutation modifies the gating of F279I K_v7.1/KCNE1 current seems to be due to an abnormal interaction of F279I K_v7.1 with the KCNE1 subunit. These effects lead to a gain of function, which likely will result in an enhanced I_{Ks} repolarizing current during the AP.

The interaction between KCNE1 and K_v7.1 appears to involve residues located extracellularly [30, 31], specific elements in the intracellular C-termini regions [32] and residues in the transmembrane segments [33] arguing for a multi-point interaction. Furthermore, it appears that these interactions are dynamic and that KCNE1 reorients with respect to K_v7.1 during channel gating [30, 31].

More importantly, during the revision process of this study, it has been reported that F232 (P-loop) and F279 (S5) in K_v7.1 are responsible for the gating modulation of this channel

by KCNE1. The authors propose that F232 steric interacts with F279 during the movement of the voltage sensor domain (VSD) hindering K_v7.1 channel from opening in the presence of KCNE1, which has been attributed to the bulky amino-acid residues that destabilizes the open state and thus shifts the voltage dependence of K_v7.1/KCNE1 channel. This study also demonstrates a high correlation between the side chain volume of F279X, indicating that the F279 on S5 defines the energy difference between the closed and the open state of F279X K_v7.1/KCNE1 channels [34]. The effects of these mutations at S5 on the electrophysiological properties of K_v7.1 might be due to an impaired coupling of the gating modulation of K_v7.1 induced by KCNE1 and not to an altered physical interaction with the β-subunit. In fact, biotinylation and immunocytochemical assays did not show changes in the protein expression of F279I compared to WT K_v7.1 channels on the cell membrane. However, an impaired assembly between F279I K_v7.1/KCNE1 channels was observed in comparison with WT K_v7.1/KCNE1. These results are in agreement with the electrophysiological studies, in which a faster activation kinetics was observed.

The contribution of I_{Ks} to repolarization is rate dependent [24]. This results in an accumulation of the channels in the pre-open states, which leads to a rate-dependent increase of current, causing AP shortening [22]. The effects of repetitive stimulation were compared between WT K_v7.1/KCNE1 and F279I K_v7.1/KCNE1 channels by applying train pulses at variable cycle lengths. At all frequencies tested, the F279I K_v7.1/KCNE1 channel complex displayed larger steady-state current compared to WT K_v7.1/KCNE1 and, importantly, they did not reach the steady state. All these data suggest that the enhanced accumulation of activation of I_{Ks} in response to increased heart rate would be more pronounced in F279I K_v7.1/KCNE1 channels, probably because its activation kinetics is faster and its deactivation kinetics slower, exhibiting an abnormal response to changes in rate.

Since the patient is heterozygous for the F279I mutation, co-expression experiments of the WT and F279I K_v7.1 together with KCNE1 were performed to mimic the *in vivo* situation. The voltage dependence of activation for WT/F279I K_v7.1/KCNE1 was intermediate to those of WT K_v7.1/KCNE1 and F279I K_v7.1/KCNE1 complexes, as it was the activation kinetics and the current magnitude. These biophysical characteristics would also point out to an enhanced function of the heterozygous channel complex. At slow rates (1-2Hz) there were no differences between the heterozygous complex and WT K_v7.1/KCNE1 channels. However, at faster rate (2.5Hz), although there was only a slight increase in the accumulation of current, it did not reach the steady-state, as the WT K_v7.1/KCNE1 complex did, suggesting an abnormal adaptation to rate changes, characteristic of patients with SQTS.

The use of mathematical models to simulate mutant conditions proved useful in order to assess its effects on the AP. Our results indicate that the gain of function of the mutant I_{Ks} has a significant effect on AP. The AP shortening in heterozygotes is about 15% (approximately 50ms) in all cell types, which fits well with the clinical phenotype. The APD reduction becomes dramatically large (about 100ms) when the homozygous condition is simulated. Since the basal adrenergic tone should likely affect the I_{Ks} influence on QTc in vivo, we also performed a preliminary analysis of the effects of adrenergic stimulation on AP. The addition of β-adrenergic stimulation actually did not change significantly the results. However, a more accurate modeling of β-adrenergic modulation of several cellular targets would be necessary to predict in quantitative terms the impact of I_{Ks} modulation on whole-cell electrophysiological function.

To test at which extent our simulation results were model-dependent, we repeated the analysis by using the ORd human ventricular model [13]. Using this model, the APD reduction was significantly smaller. This is likely due to the different formulations of I_{Ks} current in different models. It is actually still a matter of debate which is the actual quantitative weight of this current in the human APD. Some reports of only minor AP prolongation after selective block of I_{Ks} in humans [35] support the ORd I_{Ks} formulation. On the other hand, due to the high nonlinearity of the system, this does not necessarily implies that I_{Ks} overexpression would lead to only minor AP shortening. More importantly, clinical observations on the effects of $K_v7.1$ mutations in humans leading to loss of function (LQT1) or gain of function (SQTS) of I_{Ks} suggest a large quantitative impact of I_{Ks} in vivo. As a matter of fact, the TTP and other AP models, but not the ORd one, has been used up to now to analyze in silico the effects of I_{Ks} related mutations [36-38]. Given the uncertainties in the electrophysiology of human ventricular myocytes and, consequently, in mathematical models of such myocytes, the computer modeling studies should be interpreted as a qualitative rather than a quantitative illustration and the TTP vs ORd model based results can be considered as the upper and lower bounds of the actual effects of I_{Ks} gain of function on real ventricular myocytes. Nevertheless, our modeling studies overall clearly suggest a shortening of the action potential consistent with the patient phenotype, showing a mild QTc shortening.

The patient presented here with a QTc=356ms and a QTp=85.5% meets diagnostic criteria first proposed by Gollob [39], those included in the current guidelines [40] and also those used in the most recent series of short QT cases published [41]. According to SQTS diagnostic criteria proposed by Gollob [39], to begin to implement the diagnostic algorithm the QTc interval has to be shorter than 370 ms. The patient had a QTc interval of 356 ms (1

point), a Jpoint-T peak interval of 144 ms (>120 ms, no point), a first degree relative with autopsy negative who suffered SCD (1 point), and after electrophysiological characterization of the F279I Kv7.1 performed in the present study, a genotype positive (2 points). Within this criterion, the patient would obtain in summary 4 points (high probability of short QT).

As per 2013 guidelines [40], our patient also meets definitive short QT criteria: has a QTc below the cut-off of 360 ms, has a pathogenic mutation (extensively demonstrated by physiologic study and computational models) and had a family history of sudden cardiac death in a relative under 40 years of age. Moreover, patient reported in the present article will also meet inclusion criteria in the series of Short QT syndrome with larger follow-up reported by Giustetto in which the cut-off included QTc of 360 ms or less or < 88% [41].

Jpoint-Tpeak has been proposed as an useful measurement for both diagnosis and prognosis. Short QT syndrome patients tend to have a shorter Jpoint-Tpeak compared to normal individuals [42]. Our patient had a Jpoint-Tpeak which was above the Gollob cut-off of 120 ms but it was well below the normal range in general population (188±11ms). The supposed value on prognosis of the Jpoint-Tpeak has not been demonstrated in the largest follow-up series to date [41] and it is therefore not mentioned in the current criteria [40]. Peaked T waves in the precordial leads were reported in some of the first cases reported as characteristic of the short QT syndrome [43]. This finding, present in our patient, has not been consistently associated to the short QT syndrome and is not included in any of the 3 diagnostic algorithms previously discussed. Of note, peaked T waves were absent in the first publication by Gussak in 2000 [2].

Regarding QTc response to exercise in the Short QT syndrome; normal individuals with normal-low QTc compared to SQTS patients tend to shorten QTc significantly more [44]. This observation is based on a short series of cases and has not been included in the recently proposed diagnostic criteria [40]. The patient reported here showed a reduction in the QTc from resting to peak exercise of 6ms (356ms to 350ms).

The present study provides evidence for a causal relationship between the SQTS and the K_v7.1 mutation based on several findings. First, no additional mutation was found among the genes that might be responsible of the short QT phenotype. F279 residue is unique among the equivalent amino acid in the K_v7 family, and it appears to be an important amino acid for the K_v7.1/KCNE1 interaction. The electrophysiological characteristics associated with the mutation are expected to lead enhance repolarization with shortening of the QT interval (leftward shift of the activation curve, faster activation kinetics, and increased accumulation

of current in response to changes in rate). F279I $K_v7.1$ channels assembly with KCNE1 is impaired compared with WT $K_v7.1$ channels, accelerating the activation process at physiological relevant membrane potentials, which further contribute to the increased repolarization of I_{Ks} when channels incorporate F279I subunits. Finally, the TTP computer model simulation of these data predicts a similar shortening of the AP than observed in the patient.

References

[1] Cerrone M, Napolitano C, Priori SG. Genetics of ion-channel disorders. Curr Opin Cardiol 2012;27:242-52.

[2] Gussak I, Brugada P, Brugada J, Wright RS, Kopecky SL, Chaitman BR, et al. Idiopathic short QT interval: a new clinical syndrome? Cardiology 2000;94:99-102.

[3] Antzelevitch C, Pollevick GD, Cordeiro JM, Casis O, Sanguinetti MC, Aizawa Y, et al. Loss-of-function mutations in the cardiac calcium channel underlie a new clinical entity characterized by ST-segment elevation, short QT intervals, and sudden cardiac death. Circulation 2007;115:442-9.

[4] Bellocq C, van Ginneken AC, Bezzina CR, Alders M, Escande D, Mannens MM, et al. Mutation in the KCNQ1 gene leading to the short QT-interval syndrome. Circulation 2004;109:2394-7.

[5] Brugada R, Hong K, Dumaine R, Cordeiro J, Gaita F, Borggrefe M, et al. Sudden death associated with short-QT syndrome linked to mutations in HERG. Circulation 2004;109:30-5.

[6] Priori SG, Pandit SV, Rivolta I, Berenfeld O, Ronchetti E, Dhamoon A, et al. A novel form of short QT syndrome (SQT3) is caused by a mutation in the KCNJ2 gene. Circ Res 2005;96:800-7.

[7] Splawski I, Timothy KW, Sharpe LM, Decher N, Kumar P, Bloise R, et al. Ca(V)1.2 calcium channel dysfunction causes a multisystem disorder including arrhythmia and autism. Cell 2004;119:19-31.

[8] Templin C, Ghadri JR, Rougier JS, Baumer A, Kaplan V, Albesa M, et al. Identification of a novel loss-of-function calcium channel gene mutation in short QT syndrome (SQTS6). Eur Heart J 2011;32:1077-88.

[9] Macias A, Moreno C, Moral-Sanz J, Cogolludo A, David M, Alemanni M, et al. Celecoxib blocks cardiac Kv1.5, Kv4.3 and Kv7.1 (KCNQ1) channels: effects on cardiac action potentials. J Mol Cell Cardiol 2010;49:984-92.

[10] Moreno C, de la Cruz A, Oliveras A, Kharche SR, Guizy M, Comes N, et al. Marine n-3 PUFAs modulate IKs gating, channel expression, and location in membrane microdomains. Cardiovasc Res 2014;105:223-32.

[11] Valenzuela C, Sanchez Chapula J, Delpon E, Elizalde A, Perez O, Tamargo J. Imipramine blocks rapidly activating and delays slowly activating K+ current activation in guinea pig ventricular myocytes. Circ Res 1994;74:687-99.

[12] ten Tusscher KH, Panfilov AV. Alternans and spiral breakup in a human ventricular tissue model. Am J Physiol Heart Circ Physiol 2006;291:1088-100.

[13] O'Hara T, Virag L, Varro A, Rudy Y. Simulation of the undiseased human cardiac ventricular action potential: model formulation and experimental validation. PLoS Comput Biol 2011;7.

[14] Abitbol I, Peretz A, Lerche C, Busch AE, Attali B. Stilbenes and fenamates rescue the loss of I(KS) channel function induced by an LQT5 mutation and other IsK mutants. EMBO J 1999;18:4137-48.

[15] Tristani Firouzi M, Sanguinetti MC. Voltage-dependent inactivation of the human K+ channel KvLQT1 is eliminated by association with minimal K+ channel (minK) subunits. J Physiol Lond 1998;510:37-45.

[16] Smith PL, Baukrowitz T, Yellen G. The inward rectification mechanism of the HERG cardiac potassium channel. Nature 1996;379:833-6.

[17] Seebohm G, Westenskow P, Lang F, Sanguinetti MC. Mutation of colocalized residues of the pore helix and transmembrane segments S5 and S6 disrupt deactivation and modify inactivation of KCNQ1 K+ channels. J Physiol 2005;563:359-68.

[18] Wang Q, Curran ME, Splawski I, Burn TC, Millholland JM, VanRaay TJ, et al. Positional cloning of a novel potassium channel gene: KVLQT1 mutations cause cardiac arrhythmias. Nat Genet 1996;12:17-23.

[19] Seebohm G, Scherer CR, Busch AE, Lerche CI. dentification of specific pore residues mediating KCNQ1 inactivation. A novel mechanism for long QT syndrome. J Biol Chem 2001;276:13600-5.

[20] Sanguinetti MC, Curran ME, Zou A, Shen J, Spector PS, Atkinson DL, et al. Coassembly of K(V)LQT1 and minK (IsK) proteins to form cardiac I(Ks) potassium channel. Nature 1996;384:80-3.

[21] Ma L-J, Ohmert I, Vardanyan V. Allosteric features of KCNQ1 gating revealed by alanine scanning mutagenesis. Biophys J 2011;100:885-94.

[22] Silva J, Rudy Y. Subunit interaction determines IKs participation in cardiac repolarization and repolarization reserve. Circulation 2005;112:1384-91.

[23] Hund TJ, Rudy Y. Rate dependence and regulation of action potential and calcium transient in a canine cardiac ventricular cell model. Circulation 2004;110:3168-74.

[24] Rocchetti M, Besana A, Gurrola GB, Possani LD, Zaza A. Rate dependency of delayed rectifier currents during the guinea-pig ventricular action potential. J Physiol 2001;534:721-32.

[25] Viswanathan PC, Shaw RM, Rudy Y. Effects of IKr and IKs heterogeneity on action potential duration and its rate dependence : a simulation study. Circulation 1999;99:2466-74.

[26] Mirams GR, Arthurs CJ, Bernabeu MO, Bordas R, Cooper J, Corrias A, et al. Chaste: an open source C++ library for computational physiology and biology. PLoS Computational Biology 2013;9.

[27] Tamargo J, Caballero R, Gomez R, Valenzuela C, Delpon E. Pharmacology of cardiac potassium channels. Cardiovasc Res 2004;62:9-33.

[28] Gibor G, Yakubovich D, Rosenhouse-Dantsker A, Peretz A, Schottelndreier H, Seebohm G, et al. An inactivation gate in the selectivity filter of KCNQ1 potassium channels. Biophys J 2007;93:4159-72.

[29] Yang Y, Sigworth FJ. Single-channel properties of IKs potassium channels. J Gen Physiol 1998;112:665-78.

[30] Chung DY, Chan PJ, Bankston JR, Yang L, Liu G, Marx SO, et al. Location of KCNE1 relative to KCNQ1 in the I(KS) potassium channel by disulfide cross-linking of substituted cysteines. Proc Natl Acad Sci U S A 2009;106:743-8.

[31] Xu X, Jiang M, Hsu KL, Zhang M, Tseng GN. KCNQ1 and KCNE1 in the IKs channel complex make state-dependent contacts in their extracellular domains. J Gen Physiol 2008;131:589-603.

[32] Chen J, Zheng R, Melman YF, McDonald TV. Functional interactions between KCNE1 C-terminus and the KCNQ1 channel. PLoS One 2009;4.

[33] Melman YF, Krumerman A, McDonald TV. A single transmembrane site in the KCNE-encoded proteins controls the specificity of KvLQT1 channel gating. J Biol Chem 2002;277:25187-94.

[34] Nakajo K, Kubo Y. Steric hindrance between S4 and S5 of the KCNQ1/KCNE1 channel hampers pore opening. Nat Commun 2014;5:4100.

[35] Jost N, Virág L, Comtois P, Ordög B, Szuts V, Seprényi G, et al. Ionic mechanisms limiting cardiac repolarization reserve in humans compared to dogs. J Physiol 2013;591:4189-206.

[36] Adeniran I, Hancox JC, Zhang H. In silico investigation of the short QT syndrome, using human ventricle models incorporating electromechanical coupling. Front Physiol 2013;4:166.

[37] El Harchi A, Zhang H, Hancox JC. The S140G KCNQ1 atrial fibrillation mutation affects 'I(KS)' profile during both atrial and ventricular action potentials. J Physiol Pharmacol 2010 61:759-64.

[38] Veerman CC, Verkerk AO, Blom MT, Klemens CA, Langendijk PN, van Ginneken AC, et al. Slow delayed rectifier potassium current blockade contributes importantly to drug-induced long QT syndrome. Circ Arrhythm Electrophysiol 2013;6:1002-9.

[39] Gollob MH, Redpath CJ, Roberts JD. The short QT syndrome: proposed diagnostic criteria. J Am Coll Cardiol 2011;57:802-12.

[40] Priori SG, Wilde AA, Horie M, Cho Y, Behr ER, Berul C, et al. HRS/EHRA/APHRS expert consensus statement on the diagnosis and management of patients with inherited primary arrhythmia syndromes: document endorsed by HRS, EHRA, and APHRS in May 2013 and by ACCF, AHA, PACES, and AEPC in June 2013. Heart Rhythm 2013;10:1932-63.

[41] Giustetto C, Schimpf R, Mazzanti A, Scrocco C, Maury P, Anttonen O, et al. Long-term follow-up of patients with short QT syndrome. J Am Coll Cardiol 2011;58:587-95.

[42] Anttonen O, Junttila MJ, Maury P, Schimpf R, Wolpert C, Borggrefe M, et al. Differences in twelve-lead electrocardiogram between symptomatic and asymptomatic subjects with short QT interval. Heart Rhythm 2009;6:267-71.

[43] Gaita F, Giustetto C, Bianchi F, Wolpert C, Schimpf R, Riccardi R, et al. Short QT Syndrome: a familial cause of sudden death. Circulation 2003;108:965-70.

[44] Schimpf R, Veltmann C, Wolpert C, Borggrefe M. Channelopathies: Brugada syndrome, long QT syndrome, short QT syndrome, and CPVT. Herz 2009;34:281-8.

CHAPTER 3

A modern tool for computational and electrophysiology analysis: Dynamic clamp technique

Introduction

The patch-clamp technique is the main technique in electrophysiology to record action potentials or membrane current from isolated cells, using a patch pipette to gain electrical access to the cell. The common recording modes of the patch-clamp technique are current-clamp and voltage-clamp. In the current clamp mode, the current injected through the patch pipette is under control while the resulting membrane potential of the cell is recorded. Current clamp allows for measurements of action potentials that may either occur spontaneously or in response to an injected stimulus current. In voltage clamp mode, the membrane potential is held at a set level through a feedback circuit, which allows for the recording of the net membrane current at a given membrane potential. The current-clamp technique reveals some of the electrical behaviors exhibited by cells. The voltage-clamp technique allows the experimentalist to build accurate mathematical models of some of the biophysical properties responsible for these behaviors.

More recently, a third electrophysiological technique has been developed [1-3]. In this technique, often called the ‘‘dynamic-clamp’’ method, a specific non-predetermined membrane current can be added to or removed from the cell while it is in free-running current clamp mode. This current may be computed in real time, based on the recorded action potential of the cell, and injected into the cell. Instead of being computed, this current may also be recorded from a heterologous expression system such as a HEK-293 cell that is voltage-clamped by the free-running action potential of the cell (“dynamic action potential clamp”). Because the dynamic-clamp method allows one to mimic biological effects in the living cells, it allows the experimentalist to test new kinds of specific, quantitative hypotheses directly in experiments.

For example, dynamic clamping has been used to verify the hypothetical effects of neuromodulators [2]; show how particular conductances can account for changes in neural firing modes [4, 5], spike widths [6], or spike timing [7]; search for input characteristics that optimize some aspect of postsynaptic behavior [8, 9]; and study how particular parameters affect synchronization properties in ‘‘virtual networks’’ consisting of one or more biological excitable cells interacting with each other, or with modeled counterparts, in user specified ways [10-12].

History

In neurophysiology, “dynamic clamp” was introduced by Sharp et al. [2, 3], whereas similar techniques were introduced by Robinson and Kawai [1], named “conductance injection,” and by Hutcheon et al. [13], named “reactive current clamp,” all with the purpose to introduce artificial conductances into biological neurons, thus simulating a synaptic input, an additional membrane ionic current or an electrical synapse. At that time, as described in detail elsewhere [14], related techniques had already been applied in cardiac electrophysiology by Joyner and coworkers [15, 16], who designed an “Ersatz Nexus” and a “coupling clamp” circuit, respectively, both with the purpose to simulate intercellular electrical coupling through gap junctions. Although dynamic clamp thus exists in cardiac electrophysiology for well over 30 years now, it is less common than in neurophysiology. However, there is an emerging interest in the potential of dynamic clamp methodology in heart research. Recently, dynamic clamp has been used in cardiac cellular electrophysiology to study the role of the L-type calcium current ($I_{Ca,L}$) and the transient outward potassium current (I_{to}) [17, 18]. Madhvani et al. [17] blocked the native $I_{Ca,L}$ of isolated rabbit ventricular myocytes by nifedipine and introduced a virtual $I_{Ca,L}$, which was computed in real time based on a mathematical model. Thus, it was possible to examine the role of the steady-state half-activation and half-inactivation potential of $I_{Ca,L}$ on action potential characteristics, including early afterdepolarizations (EADs). Similarly, Workman et al. [18] computed a virtual I_{to} in real time that was either used to enhance (addition) or inhibit (subtraction) the native I_{to} of rabbit and human atrial myocytes. Thus, it was possible to determine the effects of I_{to} on action potential characteristics, including afterdepolarizations. In both studies, dynamic clamp was used to introduce a virtual membrane current into a single isolated cardiomyocyte. This “conventional” application of the dynamic clamp technique, which has been designated as “model clamp” [19] or “model reference current injection” [20, 21] because a model based current is injected into the myocyte.

Instead of being computed, the aforementioned virtual current may also be recorded from a HEK-293 cell, or a similar type of cell, that expresses this current and is voltage-clamped by the free-running action potential of the myocyte. This “dynamic action potential clamp” is experimentally challenging, but it has the advantage that it does not rely on a mathematical model to represent the ionic current of interest. This application of the dynamic clamp technique has been used to compare the functional effects of wild-type and mutant currents on the action potential of isolated cells.

A further application of the dynamic clamp technique, is to create intercellular electrical coupling through a virtual gap junction between two isolated cardiac myocytes that are not physically coupled ("coupling clamp"). We have used this configuration to study the synchronization of two spontaneously active sinoatrial node pacemaker cells [22]. In a more recent study by Nguyen et al. [23], this configuration was used to assess the interactions between an isolated patch-clamped ventricular myocyte and one or more surrounding (simulated) myofibroblasts.

Dynamic Clamp

The dynamic clamp technique is an extension of traditional intracellular recording techniques that allows for the introduction of an artificial conductance, controlled by the experimentalist, into a biological cell [1, 2, 24]. Dynamic clamp uses closed-loop feedback control between a cell's recorded membrane potential and an injected current calculated by a mathematical model (Figure 3.1). This feedback loop, when iterated quickly and accurately enough, is sufficient to mimic one or more biological conductances in the targeted cell. Consequently, a versatile dynamic clamp system allows investigators to simultaneously control many electrophysiological parameters within a single experiment.

The goal of dynamic-clamp techniques is to better study the roles of quantitatively specified conductances, synaptic inputs, and network structures on excitable cells. Often, this conductance comes from the real-time solution to a set of nonlinear differential equations that depend on time and membrane potential. Some potential experiments require an even greater level of realism, and consequently even more complex real-time algorithms. This objective is accomplished by constructing a system that can read instantaneous values of membrane potential V_m, and operate on them to generate virtual currents to be delivered at appropriately high update rates. Between the "reading" of V_m and the "writing" of applied current is an algorithm that represents any of a number of membrane mechanisms and other factors. Dynamic-clamp is not a typical control method, because it does not impose a particular behavior on the cell. Instead, dynamic-clamp is a method of studying the interactions between excitable cells and a user-specified computational model in an experimental setting. Dynamic-clamp can, for example, replicate the actions of modeled voltage-gated ion channels in excitable cells, or immerse those cells in virtual-reality-inspired neuronal networks. Thus, dynamic-clamp allows the researcher to test computationally rigorous hypotheses in living cells.

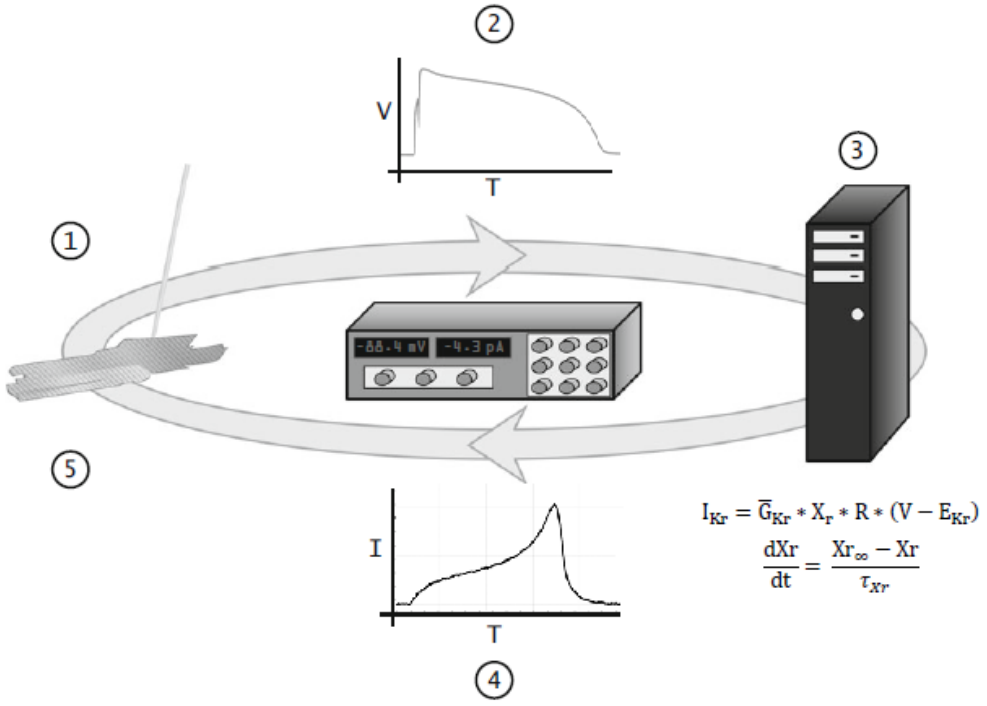

Figure 3.1. The fundamental steps of the dynamic clamp feedback loop when injecting an artifi cial conductance.

Step 1: Membrane voltage from a cardiomyocyte is measured using the patch clamp technique; step 2: sent from the amplifier to the computer's data acquisition system; step 3: voltage data is used in a computational current model to calculate current, represented here by a potassium current; step 4: calculated current data is sent to the patch clamp amplifier and step 5: injected into the cell.

Real Time eXperiment Interface

At the core of the dynamic clamp experimental setup is the software, which acts as the interface between the mathematical models and the patch-clamp hardware used to measure the parameters of the biological cell. Rapid sampling of membrane potential and fast computation of the conductance is required to adequately recapitulate a conductance [25]. Due to these requirements, real-time control is required to accomplish the dynamic clamp technique. For numerous technical reasons, real-time control is not possible on standard operating systems and software. Thus, a specialized operating system and software are required. RTXI is a fast and versatile software system adopted by many labs across many fields of electrophysiology to administer dynamic clamp experiments. The software provides real-time control using a real-time Linux operating system (Figure 3.2). Free and open-source, the platform has been tailored to fit the needs of the biological research community. RTXI uses a modular architecture, which allows investigators to construct complex experimental

protocols using a combination of built-in, community-shared, and self-made modules. More information on the software, installation, and use can be found on its Web site ([26]).

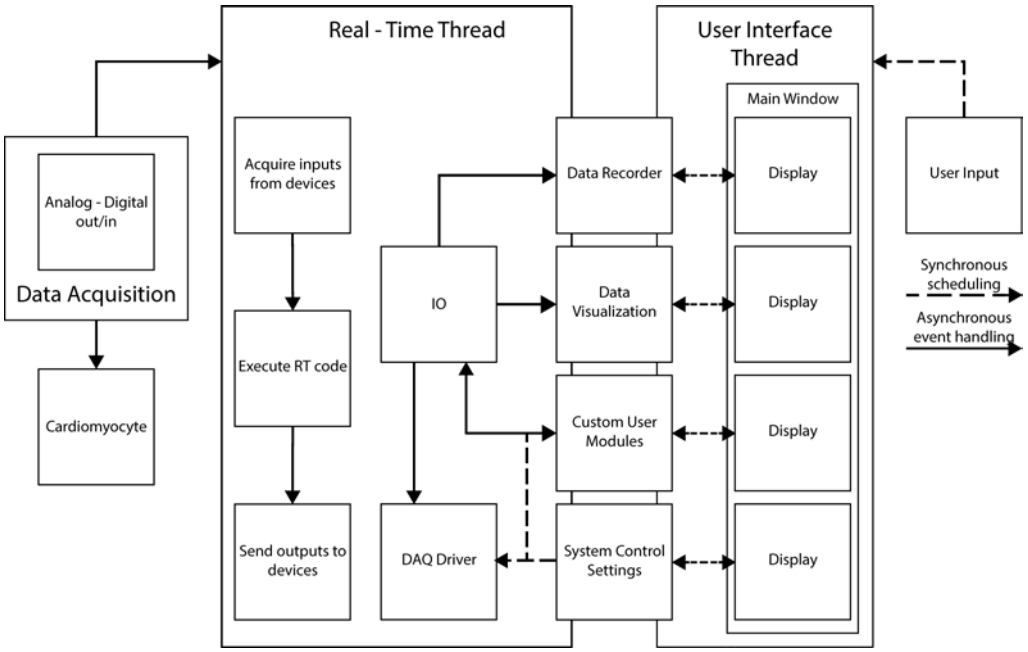

Figure 3.2. Diagram of the RTXI software architecture.

RTXI uses a two thread architecture where modules communicate and share data in real-time through a signal and slot system. On every clock cycle, a prioritized real-time thread wakes and sequentially runs its tasks - data acquisition, execution of real-time instructions of loaded modules, and signal output. Once all tasks are complete, the thread sleeps until the following cycle. Data acquisition and output is performed using the open-source COMEDI drivers, which allows RTXI to interface with many multifunction data acquisition cards. A separate user interface thread is responsible for all graphical components and user input. This approach allows for all real-time instructions to take priority over graphical components during computation.

References

[1] Robinson HPC, Kawa N. Injection of digitally synthesized synaptic conductance transients to measure the integrative properties of neurons. J Neuroscience Methods 1993;49:147-65.

[2] Sharp AA, O'Neil MB, Abbott LF, Marder E. Dynamic clamp: Computer-generated conductances in real neurons. J Neurophysiol 1993;69:992–5.

[3] Sharp AA, O'Neil MB, Abbott LF, Marder E. The dynamic clamp: Artificial conductances in biological neurons. Trends Neuroscience 1993;16:389–94.

[4] Gramoll S, Schmidt J, Calabrese RL. Stitching in the activity state of an interneuron that controls coordination of the hearts in the medicinal leech (Hirudo-medicinalis). J Exp Biol 1994;186:157–71.

[5] Hughes SW, Cope DW, Crunelli V. Dynamic clamp study of I-h modulation of burst firing and delta oscillations in thalamocortical neurons in vitro. Neuroscience (Oxford) 1998;87:541-50.

[6] Ma M, Koester J. The role of K1 currents in frequency-dependent spike broadening in Aplysia R20 neurons: A dynamic-clamp analysis. J Neuroscience 1996;16:4089–101.

[7] Jaeger D, Bower JM. Synaptic control of spiking in cerebellar Purkinje cells: Dynamic current clamp based on model conductances. J Neuroscience 1999;19:6090–101.

[8] Harsch A, Robinson HPC. Postsynaptic variability of firing in rat cortical neurons: The roles of input synchronization and synaptic NMDA receptor conductance. J Neuroscience 2000;20:6181–92.

[9] Reyes AD, Rubel EW, Spain WJ. In vitro analysis of optimal stimuli for phase-locking and time-delayed modulation of firing in avian nucleus laminaris neurons. J Neuroscience 1996;16:993-1007.

[10] Bartos M, Manor Y, Nadim F, Marder E, Nusbaum MP. Coordination of fast and slow rhythmic neuronal circuits. J Neuroscience 1999;19:6650-60.

[11] Bertram R, Previte J, Sherman A, Kinard TA, Satin LS. The phantom burster model for pancreatic beta-cells. Biophys J 2000;79:2880–92.

[12] Sharp AA, Skinner FK, Marder E. Mechanisms of oscillation in dynamic clamp constructed two-cell half-center circuits. J Neurophysiol 1996;76:867-83.

[13] Hutcheon B, Miura RM, Puil E. Models of subthreshold membrane resonance in neocortical neurons. J Neurophysiol 1996;76:698-714.

[14] Wilders R. Dynamic clamp: a powerful tool in cardiac electrophysiology. J Physiol 2006;576:349-59.

[15] Joyner RW, Sugiura H, Tan RC. Unidirectional block between isolated rabbit ventricular cells coupled by a variable resistance. Biophys J 1991;60:1038–45.

[16] Tan RC, Joyner RW. lectrotonic influences on action potentials from isolated ventricular cells. E Circ Res 1990;67:1071-81.

[17] Madhvani RV, Xie Y, Pantazis A, Garfinkel A, Qu Z, Weiss JN, et al. Shaping a new Ca 2+ conductance to suppress early afterdepolarizations in cardiac myocytes. J Physiol 2011;589:6081–92.

[18] Workman AJ, Marshall GE, Rankin AC, Smith GL, Dempster J. Transient outward K+ current reduction prolongs action potentials and promotes afterdepolarisations: a dynamic-clamp study in human and rabbit cardiac atrial myocytes. J Physiol 2012;590:4289-305.

[19] Wilders R, Verheijck EE, Kumar R, Goolsby WN, van Ginneken AC, Joyner RW, et al. Model clamp and its application to synchronization of rabbit sinoatrial node cells. Am J Physiol 1996;271:2168-82.

[20] Butera RJJ, Wilson CG, Delnegro CA, J.C. S. A methodology for achieving highspeed rates for artifi cial conductance injection in electrically excitable biological cells. IEEE Trans Biomed Eng 2001;48:1460-70.

[21] Raikov I, Preyer A, Butera RJ. MRCI: a flexible real-time dynamic clamp system for electrophysiology experiments. J Neurosci Methods 2004;30:109-23.

[22] Verheijck EE, Wilders R, Joyner RW, Golod DA, Kumar R, Jongsma HJ, et al. Pacemaker synchronization of electrically coupled rabbit sinoatrial node cells. J Gen Physiol 1998;111:95-112.

[23] Nguyen TP, Xie Y, Garfinkel A, Qu Z, Weiss JN. Arrhythmogenic consequences of myofibroblast-myocyte coupling. Cardiovasc Res 2012;93:242-51.

[24] Lin RJ, Bettencourt J, Wha Ite J, Christini DJ, Butera RJ. Real-time experiment interface for biological control applications. Conf Proc IEEE Eng Med Biol Soc 2010;1:4160-3.

[25] Bettencourt JC, Lillis KP, Stupin LR, White JA. Effects of imperfect dynamic clamp: computational and experimental results. J Neurosci Meth 2008;169:282-9.

[26] www.rtxi.org.

CHAPTER 4

Use of Dynamic – clamp for an improved identification and validation of an ionic current model

---

The content of this chapter has been published in:

Bartolucci C, Altomare C, Bennati M, Furini S, Zaza A*****, Severi S*****

Combined Action Potential- and Dynamic-Clamp for accurate computational modelling of the cardiac I_{Kr} current

Journal of molecular and cellular cardiology, vol. 79C, pp. 187–194, Nov. 2014

***** *Equal contribution to this work.*

Abstract

In the present work Action-Potential clamp (APC) and Dynamic clamp (DC) were used in combination in order to optimize the Luo-Rudy (LRd) mathematical formulation of the guinea-pig rapid delayed rectifier K^+ current (I_{Kr}), and to validate the optimized model. To this end, I_{Kr} model parameters were adjusted to fit the experimental E4031-sensitive current (I_{E4031}) recorded under APC in guinea-pig myocytes. Currents generated by LRd model (I_{LRd}) and the optimized one (I_{Opt}) were then compared by testing their suitability to replace I_{E4031} under DC.

Under APC, I_{LRd} was significantly larger than I_{E4031} (mean current densities 0.51±0.01 vs 0.21±0.05 pA/pF; $p<0.001$), mainly because of different rectification. I_{Opt} mean density (0.17±0.01 pA/pF) was similar to the I_{E4031} one (NS); moreover, I_{Opt} accurately reproduced I_{E4031} distribution along the different AP phases. Models were then compared under DC by blocking native I_{Kr} (5 µM E4031) and replacing it with I_{LRd} or I_{Opt}. Whereas injection of I_{LRd} overshortened AP duration (APD_{90}) (by 25% of its pre-block value), I_{Opt} injection restored AP morphology and duration to overlap pre-block values.

This study highlights the power of APC and DC for the identification of reliable formulations of ionic current models. An optimized model of I_{Kr} has been obtained which fully reversed E4031 effects on the AP. The model strongly diverged from the widely used Luo-Rudy formulation; this can be particularly relevant to the in silico analysis of AP prolongation caused by I_{Kr} blocking or alterations.

Introduction

Computational models of cardiac Action Potential (AP) are nowadays a very important tool to investigate the interaction between membrane ion channels with dynamically changing ionic concentrations and varying transmembrane voltage [1, 2]. These interactions are nonlinear, making the single cell a complex interactive system where a high degree of synthesis and integration occurs.

AP models combine the mathematical models of several individual membrane currents, which work in concert to induce both dramatic and subtle changes to the AP and to reproduce physiological and pathological conditions.

Ionic current models are largely based on traditional voltage clamp (V-clamp) experiments (carried out with non-physiological rectangular voltage pulses designed to study the biophysical properties of the current) and formulated with the Hodgkin-Huxley formalism [3]. Notably, current models are seldom validated against current profiles experimentally measured during the AP.

Innovative experimental approaches are now available to assess 1) the dynamic behaviour of an individual current during an imposed AP (AP-clamp technique, see e.g. [4]), and 2) the impact of a "synthetic", model-based current on freely changing AP (Dynamic-clamp, [5]).

AP-clamp is a variation of V-clamp in which the AP waveform recorded from a myocyte is used as the command potential to V-clamp the same myocyte. Under AP-clamp, individual currents are dissected from the total one by subtraction, as each current is sensitive to specific blockers [4, 6-9]. If the block is sufficiently selective and voltage-independent, the 'blocker-sensitive current' may actually provide a good estimate of the "profile" (or time-course) of the individual current during the AP. AP-clamp current profiles provide a very stringent template for the optimization of model parameters, because they recapitulate the interplay between steady-state and dynamic channel properties under the physiological voltage course.

Dynamic-clamp is a real-time hybrid computational-biological technique that has been recently developed to investigate the basic cellular mechanisms of AP formation, transfer and synchronization in physiological and pathological conditions. According to this technique a modelled current is injected into a myocyte while its effect on AP (current-clamp mode) is recorded. However, rather than being fixed as in classic "current clamp",

this current is computed from the ongoing changes in membrane potential. This is achieved by a continuous real-time loop, whereby membrane potential, recorded from the myocyte, is fed to a computer that calculates the model-based current, which is then injected back into the myocyte. The corresponding endogenous myocyte current can be pharmacologically blocked, and replaced by the modelled one. The Dynamic-clamp technique provides a unique opportunity to test the adequacy of the modelled current in the context of native electrical activity, i.e. preserving the loop interaction between the current and the membrane potential with all its determinants in place. Once the present model has been proven to adequately replace the native current in setting the membrane potential course, the AP response to specific current modifications, implemented in the model, can be tested.

In this work, for the first time, we combined AP-clamp with Dynamic-clamp in the optimization of a computational model of I_{Kr}. Obtaining accurate I_{Kr} models is of particular relevance, given the essential role of this current in cardiac repolarization and the impact of its modifications on repolarization stability. I_{Kr} plays a pivotal role in the prolongation of repolarization by drugs or genetic channel abnormalities, leading to type 2 Long QT syndrome (LQT2, [6, 10, 11]). LQT2 is commonly associated with arrhythmogenesis in general, and with the genesis of "*torsades de pointes*" ventricular tachycardias in particular.

The present work aims to 1) optimize an I_{Kr} model by fitting it to E4031-sensitive current (I_{E4031}) recorded under AP-clamp; 2) validate the model by testing its suitability to reverse E4031 effects on the AP under Dynamic-clamp; and 3) compare the optimized model to the classical Luo-Rudy formulation.

Materials and Methods

Cell isolation

Dunkin-Hartley guinea pigs were euthanized by cervical dislocation under chloral hydrate anesthesia, and ventricular myocytes were isolated using a previously published retrograde coronary perfusion method [4], with minor modifications. Rod-shaped, Ca^{2+}-tolerant myocytes were used within 12 h of dissociation. This investigation conforms to the Guide to the Care and Use of Laboratory Animals published by the US National Institutes of Health (NIH publication no. 85-23, revised 1996) and to the guidelines for Animal Care endorsed by the University of Milan.

Action-Potential Clamp

Action potential waveforms (APW) were recorded during steady-state pacing at a constant cycle length (CL) in control solution. After switching the same myocyte to V-clamp mode, the APW was applied at the same CL as the command potential, and control I_m (virtually null, except for the stimulation artefact) was recorded. Adding the I_{Kr} blocker E4031 (5 μM) to the extracellular solution elicited an inward current (compensation I_m), which was also recorded. The E4031-sensitive current (I_{E4031}, representative of I_{Kr}) was then obtained by digitally subtracting compensation I_m from control I_m. Extracellular bath solution included (in mM): 154 NaCl, 4 KCl, 2 $CaCl_2$, 1 $MgCl_2$, 5 HEPES/NaOH and 5.5 D-Glucose, at pH 7.35. Pipette intracellular solution contained (mM): 110 K^+-Aspartate, 23 KCl, 0.4 $CaCl_2$, (free Ca^{2+} = 10^{-7} M), 3 $MgCl_2$, 5 HEPES KOH, 1 EGTA KOH, 0.4 GTP-Na salt, 5 ATP-Na salt, and 5 creatine phosphate Na salt, at pH 7.3. The experiments were performed at 36°C.

I_{Kr} Model

The identification of the I_{Kr} model was based on the Luo-Rudy (LRd) formulation [12], which is nowadays the most widely used computational model of guinea pig ventricular AP. The formulation of I_{Kr} incorporates both a time-dependent activation gate, Xr, and a time-independent inactivation gate, R, to approximate the very fast inactivation process of the HERG channels:

$$I_{Kr} = \bar{G}_{Kr} * X_r * R * (V - E_{Kr}) \qquad (1)$$

$$\frac{dXr}{dt} = \frac{Xr_\infty - Xr}{\tau_{Xr}} \qquad (2)$$

$$E_{Kr} = -\frac{RT}{F} \ln \frac{[K^+]_o}{[K^+]_i} \qquad (3)$$

$$\bar{G}_{Kr} = p_1 * \sqrt{\frac{[K^+]_o}{5.4}} \qquad (4)$$

$$Xr_\infty = \frac{1}{1 + e^{\frac{-(V-p_2)}{p_3}}} \qquad (5)$$

$$R = \frac{1}{1 + e^{\frac{V-p_4}{p_5}}} \qquad (6)$$

$$\tau_{Xr} = p_6 * e^{\frac{-(V-p_7)^2}{p_8^2}} + 1 \qquad (7)$$

where V is the membrane potential, E_{Kr} is the reversal potential, and $\overline{G}_{Kr}$ represents the maximal conductance of I_{Kr}. In agreement with the experimental conditions, we set

$$[K^+]_o = 4\ \text{mM},\ [K^+]_i = 140\ \text{mM}.$$

The 8 parameters used for identification of the optimized model (I_{Opt}) were: the maximal conductance coefficient (p_1), the voltages (p_2, p_4) at which 50% of channels are activated or inactivated, the slope factors of steady state activation/inactivation (p_3, p_5) and three parameters describing the voltage dependence of the activation time constant ((p_6, p_7, p_8, Table S1). With respect to the original LRd model, the bi-exponential equation for the voltage dependence of activation time constant, τ_{Xr}, from [12] (Eqn S7b, Appendix B), was replaced with a Gaussian expression (7), in order to reduce the number of parameters to be identified. Model parameters were identified by minimizing a cost function based on the least square difference between experimental and simulated I_{Kr} time courses during AP-clamp. Minimization of the difference between the experimental and simulated $V_{@Ipeak}$, i.e. the potential at which I_{Kr} reaches its maximal amplitude, was used as a further optimization target (detailed description in the Appendix B, Text S1). Parameter space was restricted using constraints based on available physiological knowledge (Table S1, [13-16]). Two APs (recorded from two different cells at CL = 1000 ms) were used for the identification procedure.

Dynamic-Clamp

The membrane potential (V_m) of an isolated guinea-pig ventricular myocyte was continuously sampled at 5 KHz (sampling interval 0.2 ms) under whole-cell conditions and fed into a personal computer running the numerical I_{Kr} models. The latter computed I_{Kr} based on V_m input and sent the signal (after appropriate scaling) to the amplifier to command injection of modelled I_{Kr} into the myocyte (Figure 4.1). Current computation and injection were performed in real-time, i.e. they required a time shorter than the sampling interval.

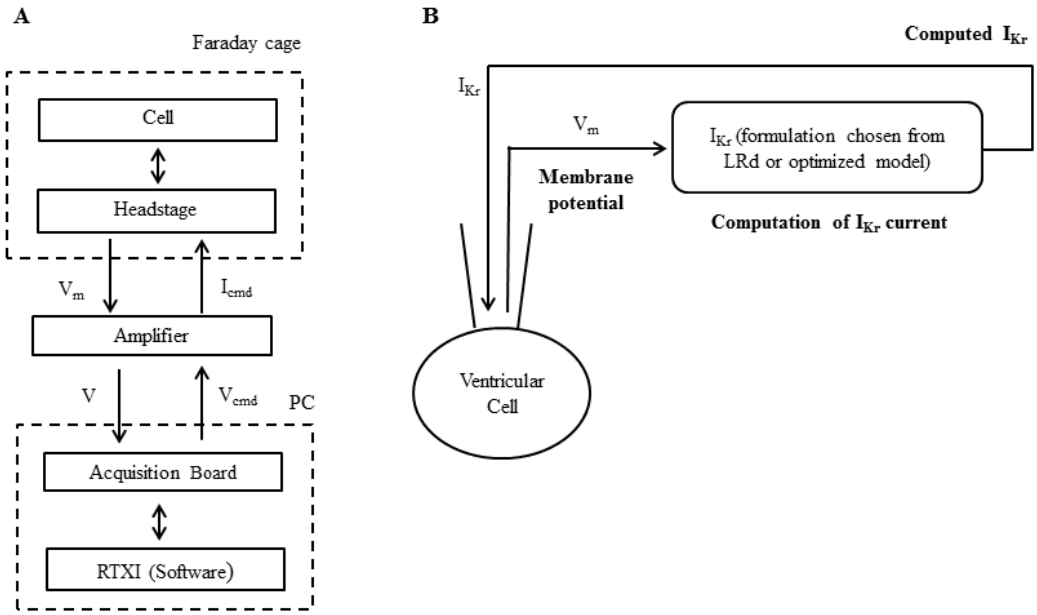

Figure 4.1. Dynamic-clamp setup

A. Block diagram of the general Dynamic-clamp system. **B.** Protocol for the injection of the model-based synthetic IKr current to substitute for the E4031-blocked sensitive current.

To implement the Dynamic-clamp, we used an amplifier (Multiclamp 700B, Axon Instruments) connected to a data acquisition board (DAQ, 6024E PCI, National Instruments) on a personal computer (Intel Celeron 3.20GHz). The experiments were performed using the open source Real-Time eXperiment Interface (RTXI, [17]), which is a real-time biological experimentation system based on Real-Time Linux. System features and custom user code were implemented as modules written in C++.

Current distribution during the AP phases

Current may affect AP duration, depending on the AP phase during which it flows [18, 19]. With the purpose of quantitatively comparing the original and optimized I_{Kr} models in terms of current distribution during the AP, repolarization was divided into 3 phases: 1) the quasi-linear plateau phase (Figure S1, P interval); 2) the quasi-linear terminal fast repolarization (Figure S1, FR interval); and 3) the knee-shaped transition between these two phases (Figure S1, K interval). To this end, a recursive routine was developed to identify the boundaries of each quasi-linear phase automatically (i.e. in an operator-independent manner); boundaries of the interposed “knee” phase were set accordingly. In brief, the routine (Matlab script file included in the Appendix B) operated by linear fitting

of the AP phase within a time-window of increasing width until the average of fitting residuals exceeded a threshold value (i.e. the AP course diverged from linearity). To delimit the P interval, only the right boundary was automatically determined, because the left one was set at the time of the AP peak. Different residual thresholds and window increments were used for P- and FR- intervals to accommodate the different repolarization velocities.

Mean current (I_{mean}) within each interval was calculated as $\frac{\int_{t1}^{t2} I*dt}{(t_2-t_1)}$ where t_1 and t_2 are interval boundaries. I_{meanP}, I_{meanK} and I_{meanFR} are the mean currents during the P, K and FR interval, respectively.

Results

Model Identification: AP-clamp

The identification results are shown in Figure 4.2: the E4031-sensitive current (I_{E4031}) obtained under AP-clamp (grey curves) was well-fitted by I_{Opt} (light grey curves). Both APs, selected to represent the extremes of APD distribution in our expectedly heterogeneous population [20], were used for the identification procedure; it can be appreciated from the figure that the same level of agreement was obtained for two APs with very different durations (left panel: APD_{90} = 94 ms, right panel: APD_{90} = 162 ms).

In contrast, I_{Kr} computed with the LRd model (I_{LRd}), under the same AP waveforms, diverged considerably from I_{E4031} (Figure 4.2, black curves). In particular, I_{LRd} was much larger during the plateau phase and slower to deactivate upon repolarization.

The bottom panels of Figure 4.2 show the dynamic current-voltage curves obtained during the AP-clamp. Membrane potentials corresponding to the peak of the current profile are also indicated: these values were similar between I_{E4031} (grey circles) and I_{Opt} (light grey circles); in contrast, the values predicted by the LRd model (black circles) were substantially more positive.

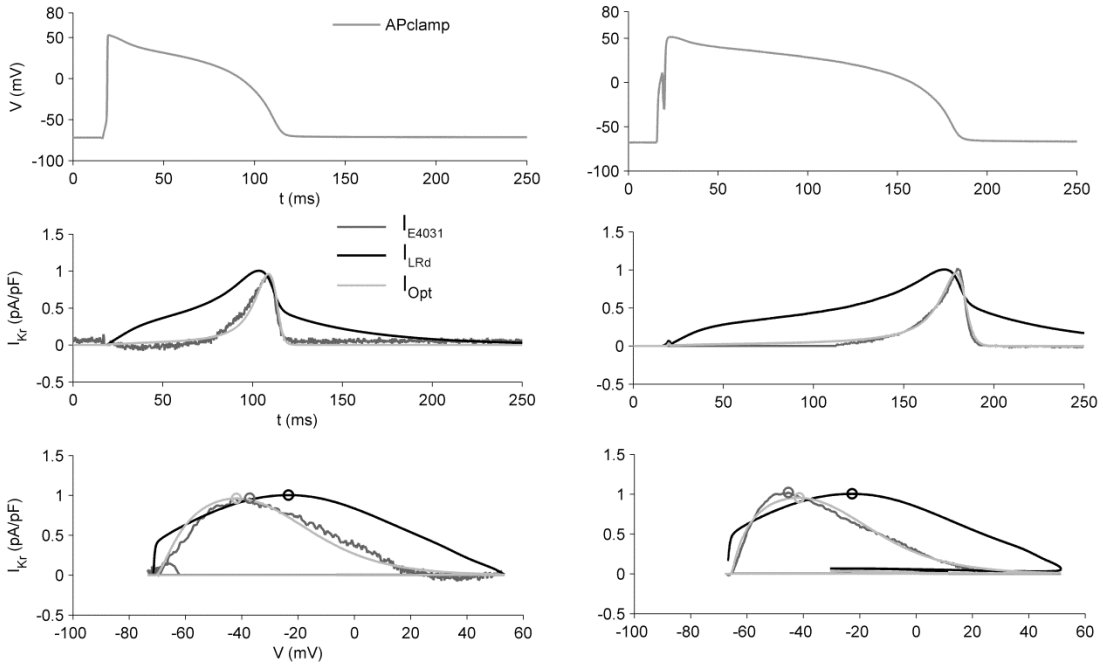

Figure 4.2. Model Identification in AP-clamp

Experimental APs used in the AP-clamp technique (top) to measure the corresponding E4031-sensitive current (grey) and to compute offline the IKr current with the LRd (black) and the optimized (light grey) model (middle). Bottom: I-V curves and V@Ipeak (circles). Both APs were recorded at CL = 1000 ms, from two different cells. See figure S2 in Appendix B for an example at CL = 300 ms.

Comparison between I_{Opt} and I_{LRd} model parameters

Model optimization, performed to fit experimentally measured $I_{E4031,}$ involved changes in its gating parameters, as detailed in the Appendix B (Table S1). The consequences of these changes are shown in Figure 4.3, where the kinetics of I_{Opt} and I_{LRd} are compared.

The main changes concerned V-dependency of steady-state inactivation and of the activation (deactivation) time constant, whereas steady-state activation was only marginally modified. The inactivation curve midpoint was shifted by -21 mV (i.e. to -30 mV) and its slope increased (Figure 4.3, left panel). The voltage dependency of the activation time constant (Figure 4.3, right panel) was shifted toward positive potentials (13 mV), its maximal value increased and its roll-off became steeper, thus slowing gating at potentials more positive than -40 mV and accelerating it at more negative ones.

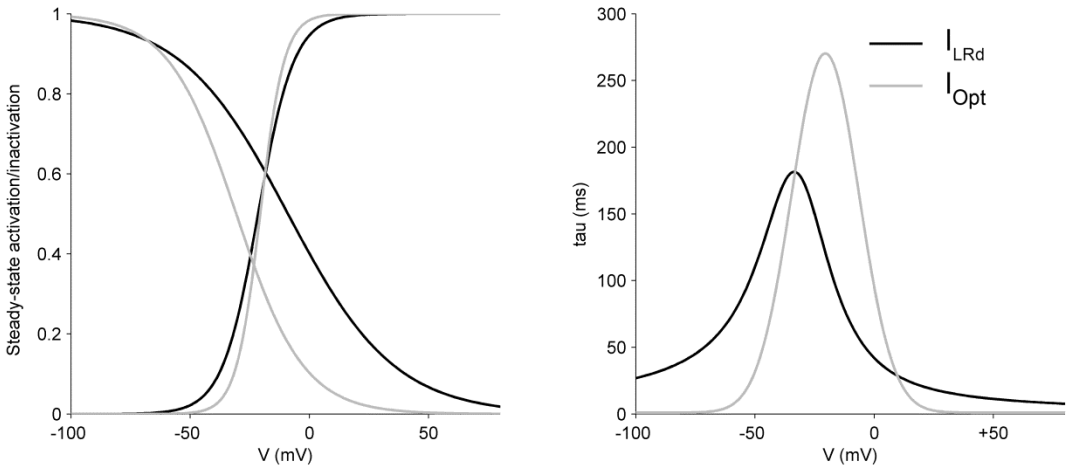

Figure 4.3. Changes in the kinetic model of IKr with respect to the LRd formulation

Steady state activation/inactivation (left) and time constant of activation (deactivation) (right) in the LRd (black) and in the optimized (grey) models.

A comprehensive and quantitative comparison between I_{E4031} and simulated currents under AP-clamp with the same waveform is reported in Table 3.1.

Table 3.1. Comparison between I_{E4031} and modelled currents under AP-clamp

I_{Kr} features of experimental current (I_{E4031}) and those simulated by LRd and Opt optimized models under AP-clamp conditions. $V_{@Ipeak}$, membrane potential in correspondence to the current peak; Imax, current peak; Imean, mean current during the AP; TTP, time to peak; ImeanP, mean current during the plateau; ImeanK, mean current during the AP "knee"; ImeanFR, mean current during the fast repolarization. Data reported as mean±standard error. *p<0.05, ***p<0.001 vs. Exp.

	CL = 1000 (n = 11)			CL = 300 (n = 9)		
	I_{E4031}	I_{LRd}	I_{Opt}	I_{E4031}	I_{LRd}	I_{Opt}
V_{peak} (mV)	-44 ± 2.4	-22 ± 0.4***	-42 ± 0.2	-47 ± 3	-23 ± 0.2***	-42 ± 0.2
I_{peak} (pA/pF)	0.93 ± 0.08	1 ± 0.04	0.96 ± 0.01	0.75 ± 0.08	0.90 ± 0.06	0.88 ± 0.06
I_{mean} (pA/pF)	0.21 ± 0.05	0.51 ±0.01***	0.17 ± 0.01	0.17 ± 0.04	0.49 ± 0.03***	0.21 ± 0.02
TTP (ms)	165 ± 16	156 ± 15***	165 ± 16	82 ± 5	75 ± 5***	81 ± 5
I_{mean}P (pA/pF)	0.05 ± 0.03	0.31 ± 0.01***	0.03 ± 0.004	0.02 ± 0.01	0.31 ± 0.01***	0.04 ± 0.001
I_{mean}K (pA/pF)	0.32 ± 0.07	0.70 ± 0.02***	0.22 ± 0.02	0.27 ± 0.06	0.78 ± 0.02***	0.3 ± 0.02
I_{mean}FR (pA/pF)	0.68 ± 0.08	0.73 ± 0.02	0.65 ± 0.02	0.47 ± 0.06	0.70 ± 0.01***	0.63 ± 0.01*

The optimized model reproduced all the experimental I_{E4031} features at CL = 1000 ms very well, while the LRd model diverged significantly in several ways. The latter consisted of more positive $V_{@Ipeak}$, larger I_{mean}, and longer TTP. In particular, the optimized model accurately reproduced the current distribution during the different AP phases, with a higher mean current in the fast repolarization, a decreased amount of current during "knee" phase and only a very small contribution during the plateau. All these results were confirmed in experiments at CL = 300 ms (see figure S2 in the Appendix B for an example), with the LRd even more far from I_{E4031} and only a small difference in the amount of current during fast repolarization between I_{Opt} and I_{E4031}.

Model Validation: Dynamic-clamp experiments

The ability of I_{Opt} and I_{LRd} to restore AP changes induced by I_{Kr} blockade (E4031, 5 µM) was tested by Dynamic-clamp during stimulation at CL = 1000, CL = 500 and 300 ms. The AP was recorded, within each myocyte, in control conditions, during I_{Kr} blockade and during its replacement by modelled current; measurements were taken after the AP had achieved a steady-state configuration under each condition. Illustrative examples of the results obtained with this protocol at the two CLs are shown in Figure 4.4.

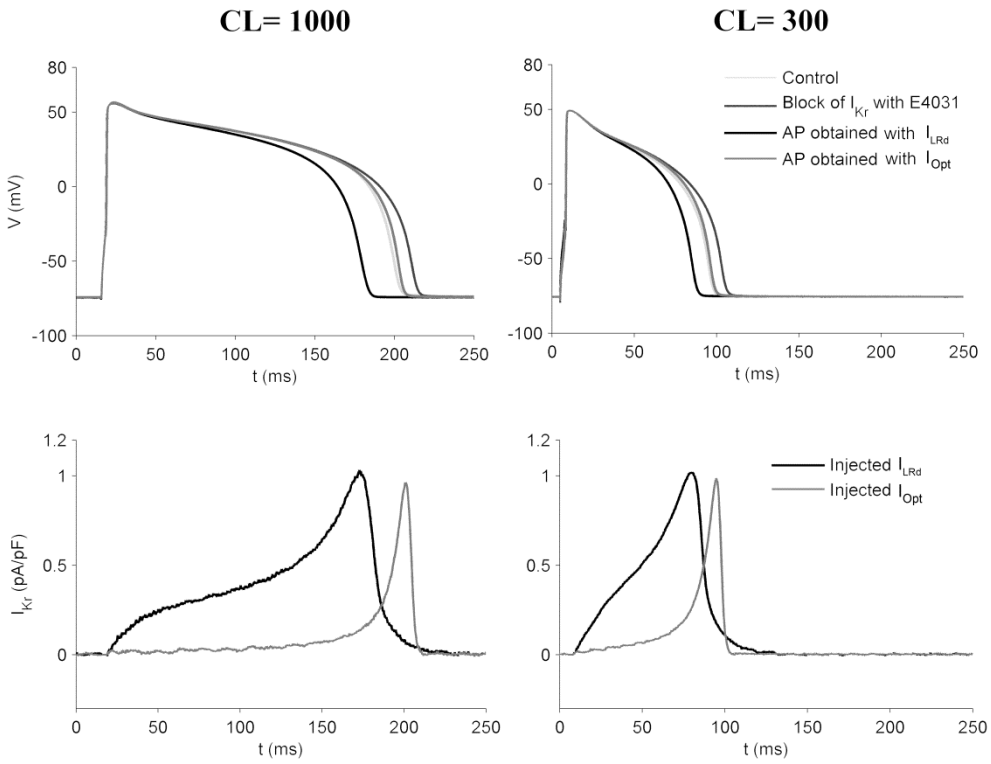

Figure 4.4. Model Validation: example of Dynamic clamp experiments

Top panels: 4 AP traces (control, under I_{Kr} block, after the injection of LRd and optimized model). Bottom panels: different injected currents, LRd (black) and optimized (grey).

AP duration was, as expected, prolonged by E4031. Whereas injection of I_{Opt} restored the AP to a profile almost overlapping that of the control, injection of I_{LRd} shortened it well below the control's. These observations are supported by the statistics of AP parameters reported in Table 3.2.

Table 3.2. AP characteristics under Dynamic clamp

Action potential features during the Dynamic clamp experiments: APDx (x = 90%, 50%, and 30% of repolarization), action potential duration; PD, plateau duration; VrepMax, maximum velocity repolarization. Data reported as mean±standard error. *p<0.05, **p<0.01, ***p<0.001 *vs.* Control.

CL (ms)		APD_{90} (ms)	APD_{50} (ms)	APD_{30} (ms)	PD (ms)	VrepMax (mV)
1000 (n = 8)	Control	204 ± 23	181 ± 21	144 ± 18	103 ± 11	-53 ± 1
	I_{Kr} Block	222 ± 4***	192 ± 1***	146 ± 17	107 ± 10	-53 ± 1
	I_{LRd} injection	150 ± 19*	136 ± 19*	114 ± 18*	80 ± 9	-49 ± 1
	I_{Opt} injection	201 ± 22	179 ± 20	143 ± 17	102 ±11	-50 ± 2
500 (n = 4)	Control	76 ± 6	62 ± 5	29 ± 2	49 ± 4	-45 ± 3
	I_{Kr} Block	99 ± 13**	82 ± 11*	36 ± 4**	65 ± 9**	-45 ± 2
	I_{LRd} injection	63 ± 5	50 ± 6	25 ± 2	39 ± 3	-43 ± 3
	I_{Opt} injection	78 ± 7	65 ± 4	32 ± 3	50 ± 5	-42 ± 2
300 (n = 8)	Control	82 ± 4	65 ± 4	46 ± 4	40 ± 2	-54 ± 1
	I_{Kr} Block	92 ± 5***	71 ± 5***	50 ± 4***	44 ± 3*	-56 ± 1
	I_{LRd} injection	75 ± 4***	60 ± 4**	44 ± 4	36 ± 2*	-54 ± 2
	I_{Opt} injection	83 ± 5	68 ± 4*	49 ± 3**	42 ± 3	-55 ± 2

Data in Table 3.2 show that the I_{Kr} blockade mostly prolonged APD_{50}, which incorporates the P- and K-intervals, while VrepMax was not affected. Marked reduction of APD_{30}, reflecting to a larger extent the P-interval, mainly accounted for the excessive APD shortening observed with injection of I_{LRd}.

Comparison of I_{Opt} and I_{LRd} in the context of a numerical AP model

This section aims to assess the differences produced by I_{Kr} model optimization in the generation of AP waveforms by a completely numerical AP model, the Luo-Rudy dynamic model [12], in which either I_{Opt} or I_{LRd} were incorporated. Figure 4.5A compares the two models (I_{LRd} black, I_{Opt} grey) in terms of contribution of the current to different AP phases, as assessed by measuring the "mean I_{Kr}" flowing during each phase (see Methods) at CL 1000 ms. The pattern of I_{Opt} distribution during AP is similar to the one recorded during AP-clamp experiments (see Table 3.1); I_{LRd} caused a larger I_{Kr} contribution during the plateau phase and maximal expression during the K-interval.

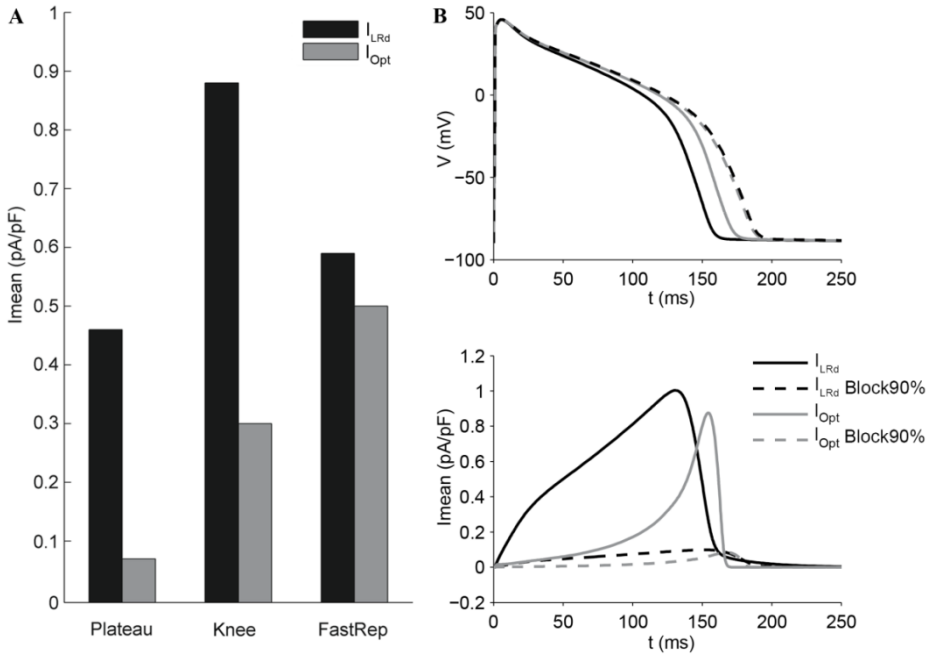

Figure 4.5. Comparison of Opt and LRd I_{Kr} models in the context of a numerical AP model

A. Comparison of the original LRd (black) and Opt (grey) I_{Kr} models in terms of contribution of the current to different AP phases. **B**. Consequence of I_{Kr} blockade on AP contour with both numerical models, in control (continuous lines) and with 90% reduction of maximal conductance (dotted line).

Figure 4.5B shows the consequence of I_{Kr} blockade (90% reduction of maximal conductance) on AP contour. When I_{Opt} was used, APD_{90} prolongation induced by simulated I_{Kr} blockade was comparable for the AP model (ΔAPD_{90} = 17 ms, equal to 9%) and Dynamic-clamp experiments (ΔAPD_{90} = 18 ms, equal to 8%, see Table 3.2). When I_{LRd} was used instead, the AP model overestimated the change in APD_{90} induced by I_{Kr} blockade (ΔAPD_{90} = 29 ms, equal to 16%).

Discussion

In this paper, two advanced experimental approaches, AP-clamp and Dynamic-clamp, were used in combination to reformulate the I_{Kr} LRd model equations in order to fit the experimental data and to validate the optimized I_{Kr} model.

The results of the AP-clamp experiments (see, e.g., Figure 4.2) show that the E4031-sensitive current profile was very different from that predicted by the LRd model. This led us to the identification of an optimized I_{Kr} model, generating a current (I_{Opt}) which more reliably reproduces the experimental recordings (Figure 4.2 and Table 3.1). In Dynamic-clamp experiments, replacing the current blocked by E4031 with I_{Opt}, but not with I_{LRd}, fully restored AP contour (Figure 4.4 and Table 3.2). This provides a robust and novel confirmation that known I_{Kr} properties, i.e. those incorporated in I_{Opt}, are adequate to account for the physiological role of the current blocked by E4031, largely representative of I_{Kr}.

The most important difference of I_{Opt}, with respect to the original LRd model, is in the voltage dependence of inactivation (often called “rectification” in the case of I_{Kr}). In particular, I_{Opt} inactivation starts at more negative potentials (about -60 mV) and is almost complete at 10 mV (Figure 4.3, left panel). This results in a sharp reduction of current amplitude during the plateau phase of the AP, as required to fit I_{E4031} profile recorded under AP-clamp. The observation that, under Dynamic-clamp, I_{LRd} injection grossly overshot the AP changes induced by E4031 (Figure 4, bottom, black trace), indicates that such a difference in rectification has a strong impact on AP course.

A discrepancy in the extent of rectification between the LRd model and I_{Kr} measured by Rocchetti et al. under AP-clamp [4] has been already pointed out by Silva and Rudy ([21], Appendix). They attributed this discrepancy to the properties of ErgTx, the specific HERG channel blocker [22] used to identify I_{Kr} under AP-clamp. Indeed, ErgTx block displays

mild voltage-dependence, being relieved at positive membrane potentials [14]; this would lead to underestimating I_{Kr} during the plateau phase.

In the present study I_{Kr} was identified by E4031 blockade. For this agent block is favoured by persistence of membrane potential at values at which channels are inactivated [23]. In particular, block requires channel opening [24], the drug is trapped by the closed state and a very long time is required for unbinding from closed channels at diastolic potentials [25]. As a consequence, at physiological duty-cycle, about 20 cycles may be required for block to achieve its steady-state; however, once established, block remains constant within each cycle [26]. Thus, provided that measurements are made at steady-state, block cannot dissipate during the AP plateau, therefore I_{E4031} cannot underestimate plateau current (i.e. overestimate rectification) and looks best suited for an unbiased estimation of I_{Kr} profile. Further rationale for I_{Kr} model optimization on I_{E4031} is provided by considering that E4031 is easily accessible and has been widely used to assess I_{Kr}‘s physiological role. Formulation of the LRd model (used for I_{LRd}) was actually based on voltage clamp measurements of I_{E4031}. Therefore, even if it slightly diverged from I_{Kr}, I_{Opt} would be relevant to the interpretation of the large amount of data concerning the effect of E4031 on electrical activity.

Silva and Rudy [21] also reported that stronger rectification would conflict with the seminal I_{Kr} description by Sanguinetti and Jurkiewicz [16], on whose data the LRd model formulation was based. Scrutiny of the literature up to the present date reveals that data on I_{Kr} in guinea pig ventricular myocytes are limited ([13-16]) and the voltage-dependency of inactivation was assessed only in the original description by Sanguinetti and Jurkiewicz [16], which is thus assumed as the “golden-standard”. Nevertheless, assessment of I_{Kr} inactivation gating in native myocytes by classic V-clamp protocols is necessarily only indirect, i.e. based on “subtraction” of activation gating [16]. As such, it implies significant assumptions, which may limit its reliability. Notably, several data on heterologous systems ([10, 27-32]) and nodal myocytes ([33, 34]) are reported where the half-maximal inactivation ranges between -20 and -80 mV, i.e. is substantially more negative than that reported by Sanguinetti and Jurkiewicz (-9 mV) [16]. In a subsequent work, Sanguinetti et al. [35] also found in Xenopus oocytes that the $V_{1/2}$ was more negative (-49 mV) and attributed this difference to the difficulty in dissecting I_{Kr} from I_{K1} in ventricular myocytes. They claimed that the absence of overlapping current in rabbit nodal cells ([33, 34]) and in oocytes expressing HERG allowed more accurate measure of the voltage dependence of channel inactivation. Difficulties inherent to inactivation assessment in native myocytes might also contribute to the reported discrepancy. Single-channel analysis would enable a more reliable description of voltage-

dependent gating, but given the small conductance of HERG channels, elementary currents can be measured only in a narrow range of membrane potentials. Nevertheless, in single channel I_{Kr} recordings, opening events were very seldom observed during sustained depolarization, thus suggesting strong and fast channel inactivation [36].

Taken together, these considerations support the idea that I_{E4031} may truly provide a reasonable estimate of the I_{Kr} dynamic behaviour and that currently adopted mathematical formulation of I_{Kr} needs to be revisited. The results of the present analysis suggest that the proposed "optimized model" is a significant improvement in this direction.

Crucial information on the dynamic behaviour of currents during cardiac repolarization, suitable to validate model predictions, has been provided by the AP-clamp technique [4, 7], more recently applied to sequential analysis of multiple ionic currents within the same cell [9]. However, even in its more recent developments, AP-clamp remains a "open loop" approach, i.e. it fails to consider feed-back interaction between current and membrane potential, which may have a strong impact on the ultimate effect of current modifications on electrical stability. Complementing AP-clamp with Dynamic-clamp, which incorporates current-voltage feed-back, overcomes such limitation. A caveat to be considered in interpreting Dynamic-clamp results is that the numerical model replaces the native current in terms of charge flux, but not ion molar flux. This may be relevant when the latter is likely to affect other conductances by contributing to the sub-sarcolemmal ionic milieu, as in the case of Ca^{2+} and Na^{+} currents. Sub-sarcolemmal K^{+} has a smaller impact on other conductances, therefore this limitation may be less relevant when K^{+} currents ar**e** evaluated. Moreover, many ionic currents are sensitive to Ca^{2+} (not just to membrane potential), but Dynamic-clamp cannot measure the Ca^{2+} concentration in real time during AP to use it as further model input. Since I_{Kr} is not sensitive to Ca^{2+} [9, 37] this limitation does not affect our results. However, when Ca^{2+}-sensitive currents are studied, attention has to be paid to this aspect.

Limitations

A potential limitation of the presented model is the lack of inactivation time-dependency (i.e. inactivation and its recovery were considered instantaneous). This actually follows current modelling approaches [12, 16], and reflects the difficulty in resolving I_{Kr} inactivation kinetics in myocytes at physiological temperature. Model

optimization of I_{E4031}, recorded in guinea-pig myocytes by AP-clamp and during voltage-ramps, suggested inactivation time constants ranging from 1 to 4 ms over a physiologically significant range of potentials [4]. Introducing such inactivation kinetics causes a relatively small (16%) decrease of peak I_{Opt} which, being confined to phase 3 repolarization, may have little impact on overall repolarization rate (3 ms APD_{90} prolongation vs instantaneous inactivation; A. Zaza, unpublished observations). Considering the predictably small impact of inactivation time-dependency on repolarization and the uncertainty of kinetic estimates, we chose not to diverge from LRd model structure under this aspect, focusing instead on parameter identification. Nevertheless, introducing inactivation time-dependency may represent a further refinement of the model.

Conclusions

In conclusion, this study provides an optimized I_{Kr} model able to reproduce AP- and Dynamic- clamp experimental data. The main change in the optimized model with respect to the original is a more pronounced inactivation. A positive message conveyed by the present results is that, once a reliable numerical I_{Kr} model is developed, it can be expected to accurately reproduce the native I_{Kr} behaviour in the context of myocyte complexity. This is particularly relevant in consideration of the peculiar role of I_{Kr} in repolarization and of the high cost of biological tests currently used to assess the drug arrhythmogenic potential due to I_{Kr} alterations. An increasing role in this area is being played by *in-silico* simulations using ventricular cardiomyocyte models. The potential of numerical modelling has been recently acknowledged by pharmaceutical industry, and the US Food and Drug Administration has recently announced inclusion of *in-silico* methods in a new paradigm for drug safety assessment [38]. In order for this approach to be effective, a stringent revision of mathematical formulations compared to experimental data is warranted.

The optimized model can be integrated into action potential models to explore the effects of changes in individual kinetic parameters on cardiac repolarization, and to implement the *in silico* assessment of pathology- or drug-induced I_{Kr} alterations.

References

[1] Roberts BN, Yang PC, Behrens SB, Moreno JD, Clancy CE. Computational approaches to understand cardiac electrophysiology and arrhythmias. Am J Physiol Heart Circ Physiol 2012;303:766-83.

[2] Severi S, Rodriguez B, Zaza A. Computational cardiac electrophysiology is ready for prime time. Europace 2014;16:382-3.

[3] Hodgkin AL, Huxley AF. A quantitative description of membrane current and its application to conduction and excitation in nerve. J Physiol 1952;117:500-44.

[4] Rocchetti M, Besana A, Gurrola GB, Possani LD, Zaza A. Rate dependency of delayed rectifier currents during the guinea-pig ventricular action potential. J Physiol 2001;534:721-32.

[5] Wilders R. Dynamic clamp: a powerful tool in cardiac electrophysiology. J Physiol 2006;576:349-59.

[6] Benhorin J, Moss AJ, Bak M, Zareba W, Kaufman ES, Kerem B, et al. Variable expression of long QT syndrome among gene carriers from families with five different HERG mutations. Ann Noninvasive Electrocardiol 2002;7:40-6.

[7] Rocchetti M, Freli V, Perego V, Altomare C, Mostacciuolo G, Zaza A. Rate dependency of beta-adrenergic modulation of repolarizing currents in the guinea-pig ventricle. J Physiol 2006;574:183-93.

[8] Zaza A, Micheletti M, Brioschi A, Rocchetti M. Ionic currents during sustained pacemaker activity in rabbit sino-atrial myocytes. J Physiol 1997;505:677-88.

[9] Banyasz T, Horvath B, Jian Z, Izu LT, Chen-Izu Y. Sequential dissection of multiple ionic currents in single cardiac myocytes under action potential-clamp. J Mol Cell Cardiol 2011;50:578-81.

[10] Ficker E, Thomas D, Viswanathan PC, Dennis AT, Priori SG, Napolitano C, et al. Novel characteristics of a misprocessed mutant HERG channel linked to hereditary long QT syndrome. Am J Physiol Heart Circ Physiol 2000;279:1748-56.

[11] Moss AJ, Zareba W, Kaufman ES, Gartman E, Peterson DR, Benhorin J, et al. Increased risk of arrhythmic events in long-QT syndrome with mutations in the pore region of the human ether-à-go-go-related gene potassium channel. Circulation 2002;105:794-9.

[12] Zeng J, Laurita KR, Rosenbaum DS, Rudy Y. Two components of the delayed rectifier K+ current in ventricular myocytes of the guinea pig type. Theoretical formulation and their role in repolarization. Circ Res 1995;77:140-52.

[13] Bryant SM, Wan X, Shipsey SJ, Hart G. Regional differences in the delayed rectifier current (IKr and IKs) contribute to the differences in action potential duration in basal left ventricular myocytes in guinea-pig. Cardiovasc Res 1998;40:322-31.

[14] Gurrola GB, Rosati B, Rocchetti M, Pimienta G, Zaza A, Arcangeli A, et al. A toxin to nervous, cardiac, and endocrine ERG K+ channels isolated from Centruroides noxius scorpion venom. The FASEB Journal 1999;13:954-62.

[15] Heath BM, Terrar DA. Protein kinase C enhances the rapidly activating delayed rectifier potassium current, IKr, through a reduction in C-type inactivation in guinea-pig ventricular myocytes. J Physiol 2000;522:391-402.

[16] Sanguinetti MC, Jurkiewicz NK. Two components of cardiac delayed rectifier K+ current. Differential sensitivity to block by class III antiarrhythmic agents. J Gen Physiol 1990;96:195-215.

[17] Hodgkin AL, Huxley AF. *Action potentials recorded from inside a nerve fibre*. Nature 1939;144:710-1.

[18] Zaza A. Control of the cardiac action potential: The role of repolarization dynamics. J Mol Cell Cardiol 2010;48:106-11.

[19] Bányász T, Horváth B, Virág L, Bárándi L, Szentandrássy N, Harmati G, et al. Reverse rate dependency is an intrinsic property of canine cardiac preparations. Cardiovasc Res 2009;84:237-44.

[20] Main MC, Bryant SM, Hart G. Regional differences in action potential characteristics and membrane currents of guinea-pig left ventricular myocytes. Exp Physiol 1998;83:747-61.

[21] Silva J, Rudy Y. Subunit Interaction Determines IKs Participation in Cardiac Repolarization and Repolarization Reserve. Circulation 2005;112:1384-91.

[22] Possani LD. Structure of Scorpion Toxins. In: Tu AT, editor. Handbook of Natural Toxins. New York: Marcel Dekker, Inc.; 1984 p. 513-50.

[23] Gessner G, Heinemann SH. Inhibition of hEAG1 and hERG1 potassium channels by clofilium and its tertiary analogue LY97241. Br J Pharmacol 2003;138:161-71.

[24] Spector PS, Curran ME, Keating MT, Sanguinetti MC. Class III antiarrhythmic drugs block HERG, a human cardiac delayed rectifier K+ channel. Open-channel block by methanesulfonanilides. Circ Res 1996;78:499-503.

[25] Ishii K, Nagai M, Takahashi M, Endoh M. Dissociation of E-4031 from the HERG channel caused by mutations of an amino acid results in greater block at high stimulation frequency. Cardiovasc Res 2003;57:651-9.

[26] Hancox JC, Levi AJ, Witchel HJ. Time course and voltage dependence of expressed HERG current compared with native "rapid" delayed rectifier K current during the cardiac ventricular action potential. Pflügers Arch 1998;436:843-53.

[27] Wang S, Liu S, Morales MJ, Strauss HC, Rasmusson RL. A quantitative analysis of the activation and inactivation kinetics of HERG expressed in Xenopus oocytes. J Physiol 1997;502:45-60.

[28] Zou A, Xu QP, Sanguinetti MC. A mutant in the pore region of HERG K+ channels expressed in Xenopus oocytes reduces rectification by shifting the voltage dependence of inactivation. J Physiol 1998;509:129-37.

[29] Vandenberg JI, Varghese A, Lu Y, Bursill JA, Mahaut-Smith MP, Huang CL-H. Temperature dependence of human ether-a`-go-go-related gene K currents. Am J Physiol Cell Physiol 2006;291:165-75.

[30] Wang HZ, Shi H, Liao SJ, Wang Z. Inactivation gating determines nicotine blockade of human HERG channels. Am J Physiol 1999;277:1081-8.

[31] Walker BD, Singleton CB, Bursill JA, Wyse KR, Valenzuela SM, Qiu MR, et al. Inhibition of the human ether-a-go-go-related gene (HERG) potassium channel by cisapride: affinity for open and inactivated states. Br J Pharmacol 1999;128:444-50.

[32] Berecki G, Zegers JG, Verkerk AO, Bhuiyan ZA, de Jonge B, Veldkamp MW, et al. HERG Channel (Dys)function Revealed by Dynamic Action Potential Clamp Technique. Biophys J 2005;88:566-78.

[33] Carmeliet E. Voltage- and Time-Dependent Block of the Delayed K+ Current in Cardiac Myocytes by Dofetilide. J Pharmacol Exp Ther 1992;262:809-17.

[34] Shibasaki T. Conductance and kinetics of delayed rectifier potassium channels in nodal cells of the rabbit heart. J Physiol 1987;387:227-50.

[35] Sanguinetti MC, Jiang C, Curran ME, Keating MT. A mechanistic link between an inherited and an acquired cardiac arrhythmia: HERG encodes the IKr potassium channel. Cell 1995;81:299-307.

[36] Zou A, Curran ME, Keating MT, Sanguinetti MC. Single HERG delayed rectifier K+ channels expressed in Xenopus oocytes. Am J Physiol 1997;272:1309-14.

[37] Banyasz T, Jian Z, Horvath B, Khabbaz S, Izu L, Chen-Izu Y. Beta-adrenergic stimulation reverses the IKr-IKs dominant pattern during cardiac action potential. Pflugers Arch - Eur J Physiol 2014:1-10.

[38] Sager PT, Gintant G, Turner JR, Pettit S, Stockbridge N. Rechanneling the cardiac proarrhythmia safety paradigm: a meeting report from the Cardiac Safety Research Consortium. American Heart Journal 2014;167:292–300.

CHAPTER 5

Use of Dynamic – clamp for a sensitivity analysis of the current parameters on the AP features

---

The content of this chapter has been submitted to:

Altomare C, **Bartolucci C**, Sala L, Rocchetti M, Mostacciuolo G, Severi S*****, Zaza A*****,

IKr impact on repolarization and its variability assessed by Dynamic-Clamp

Circulation: Arrhythmia and Electrophysiology

Abstract

***Background**: repolarization and its stability are exquisitely sensitive to I_{Kr} features. Information on the relative importance of specific I_{Kr} abnormalities is missing and would assist in the evaluation of arrhythmogenic risk.*

***Methods and Results:** in single guinea-pig myocytes, endogenous I_{Kr} was replaced by modelled I_{Kr} (mI_{Kr}) by Dynamic-Clamp (DC) at a cycle length of 1 s. mI_{Kr} parameters were systematically modified and the resulting changes in action potential duration (APD) and its short term variability (SD1) were measured. We observed that: 1) I_{Kr} blockade increased SD1 more than expected by its dependency on APD; 2) mI_{Kr} completely reversed APD and SD1 changes caused by I_{Kr} blockade; 3) repolarization was most sensitive to inactivation shifts, which affected APD and SD1 concordantly; 4) activation shifts of the same magnitude had marginal impact on APD but, only when reducing mI_{Kr}, they significantly increased SD1; 5) changes in maximal conductance resulted in a pattern similar to that of activation shifts.*

***Conclusions:** the largest effect on repolarization and its stability are expected from changes in I_{Kr} inactivation. APD is less sensitive to changes in other I_{Kr} gating parameters, which are better revealed by SD1 changes. SD1 may be more sensitive than APD in detecting I_{Kr}-dependent repolarization abnormalities.*

Introduction

Abnormalities of the rapid component of the "delayed rectifier" K^+ current ($I_{Kr,}$ HERG channel) are associated with remarkable prolongation and instability of repolarization. Both these conditions entail arrhythmic risk [1], as epitomized by the phenotype of HERG loss-of-function mutations (type 2 Long-QT syndrome; LQT2).

One of the major challenges of translational electrophysiology remains prediction of the functional phenotype associated with a given channel abnormality. Even once specific functional defects have been identified in heterologously expressed channels, their impact on cell electrical activity remains difficult to predict. This is because the action potential (AP) is determined by feed-back interplay between membrane potential, many current components, intracellular Ca^{2+} and, likely, further unknown factors. "Dynamic-clamp" (DC) is a promising approach to this problem, because it allows to test how the properties of a numerically modelled current affect the AP generated by a real myocyte [2, 3]. An individual ionic current is orders of magnitude simpler to model that the whole AP; thus, DC is expectedly more reliable than whole AP modeling in predicting the outcome of a current abnormality.

This work exploits DC to systematically analyze the effect of changes in I_{Kr} conductance and gating properties on guinea-pig AP duration (APD) and its time-variability, an index of electrical instability [1, 4, 5]. The results provide information, potentially of general value, on the weight of individual I_{Kr} gating features in determining repolarization course and stability. Once clinically validated, such information might be instrumental to risk assessment and clinical management of I_{Kr} mutations.

Methods

Cell isolation

Dunkin-Hartley Guinea pigs were euthanized by cervical dislocation under 800 mg/Kg chloral hydrate intraperitoneally anesthesia. Ventricular myocytes were isolated by using a retrograde coronary perfusion method previously published [6], with minor modifications. Rod-shaped, Ca^{2+}-tolerant myocytes were used within 12 h from dissociation. This investigation conforms to the Guide to the Care and Use of Laboratory Animals published by

the US National Institutes of Health (NIH publication no. 85-23, revised 1996) and to the guidelines for Animal Care endorsed by the University of Milano-Bicocca.

I_{Kr} numerical model

A deterministic, Hodgkin-Huxley-type (HH), model of I_{Kr} was developed by optimizing the Luo-Rudy model [7, 8] against I_{Kr} profile recorded under AP-clamp conditions. To this end, we developed a parameter optimization routine based on the least square difference between experimental and simulated I_{Kr} time courses during AP-clamp. Inactivation and its recovery were considered instantaneous, as in the Luo-Rudy model. Preliminary simulations (Appendix B) indicated that this simplification slightly increased peak I_{Kr} amplitude, but failed to impact on APD and, more importantly, on the effect of other parameter changes. Model code was implemented by using the Real-Time eXperiment Interface (RTXI; www.rtxi.org). Baseline model parameter values are listed in Appendix B Table S1, their modifications are described in the relevant sections of Results.

Electrophysiology

Recordings were carried out on single myocytes, superfused with standard Tyrode's solution (Appendix B Table S2) by patch clamp in the whole-cell configuration at 36.5 °C. Ca^{2+} and EGTA concentrations were calculated to achieve free pipette Ca^{2+} = 10^{-7} M with minimal buffering of systolic transients, as indicated by persistence of sharp myocyte contractions. I_{Kr} was completely and selectively blocked by 5 μM E4031 [9] added to Tyrode solution.

Action potentials (AP) were recorded (I-clamp mode) at pacing cycle length (CL) of 1s and subsequently applied at the same CL as command potential in V-clamp mode (AP-clamp), as previously described [10]. I_{Kr} was identified as E4031-sensitive current (I_{E4031}) after achievement of steady-state block. I_{E4031} profile was then used as a template for optimization of I_{Kr} model parameters [11].

Dynamic clamp

In DC, APs, recorded from the myocytes, were acquired at a sampling rate of 5 KHz into the computer to drive the numerical I_{Kr} model. Modelled I_{Kr} (mI_{Kr}) was calculated in real-time

(within one sampling interval) and injected into the myocyte during continued AP recording. Endogenous I_{Kr}, blocked by E4031, was thus replaced by mI_{Kr}, while leaving in place all the other determinants of myocyte electrical activity. APs were recorded at a CL = 1 s for at least 3 minutes after achieving a steady AP profile. 5 μM E4031 was then applied to block endogenous I_{Kr}. mI_{Kr} injection was then activated (under continuous E4031 superfusion) and the resulting AP changes recorded.

After verifying that mI_{Kr} injection restored the AP to control profile, the relevant model parameters were changed and the ensuing AP changes recorded within the same myocyte. APD variability measurements (SD1 and SD2, see subsequent subsection) were performed over at least 40 beats after AP profile had fully adapted under each condition.

Data analysis and statistics

APD was measured at the 90% repolarization level; beat-to-beat measurements were automatically performed by a custom software routine.

SD1 (ms, also referred to as STV) [12], graphically defined in APD_n *vs* APD_{n+1} (Poincaré) plots as the mean of orthogonal deviations from the identity line, was calculated as [12]:

$$SD1 = \sum \frac{|APD_{n+1} - APD_N|}{n_{beats} \cdot \sqrt{2}}$$

where APD_n and APD_{n+1} indicate APD of the n^{th} and $n+1^{th}$ APs respectively, and n_{beats} denotes the total number of consecutive beats analyzed.

SD2 (ms, also referred to as LTV) [12], graphically defined in Poincaré plots as the mean of deviations along the identity line, was calculated as [12, 13]:

$$SD2 = \sum \frac{|APD_{n+1} + APD_N - 2APD_{mean}|}{n_{beats} \cdot \sqrt{2}}$$

According to a numerical analysis presented in the Appendix B, while both SD1 and SD2 are measures of variability, their ratio (SD1/SD2) is independent from variability magnitude, but proportional to its frequency content. Put in simple terms, whereas a high SD1/SD2 ratio

indicates prevalence of beat-to-beat APD variability (SD1/SD2= ∞ in 1:1 "alternans"), a low one implies that a larger number of cycles is required for the same APD change (see Appendix B text and Figures S1 and S2 for more detail). Whereas SD1 and SD2 covariate in most circumstances, SD1/SD2 carries independent information; therefore, variability will be expressed in terms of SD1 and SD1/SD2 ratio.

To analyze I_{Kr} distribution during the AP, repolarization was divided in 3 phases: Phase 1: the quasi-linear plateau phase, Phase 3: the quasi-linear terminal fast repolarization and Phase 2: the transition between these two phases. Proximal and distal boundaries of each quasi-linear phase were determined with a custom-made recursive routine (i.e. in an operator-independent manner) detecting divergence from linearity [11].

Boundaries of the interposed phase 2 were set accordingly. Mean current (I_{mean}) within each phase was calculated as

$$I_{mean} = \frac{\int_{t_1}^{t_2} I * dt}{(t_2 - t_1)}$$

where t_1 and t_2 are phase boundaries.

Means were compared by paired t-test or ANOVA, as appropriate; Bonferroni's test was used for post-hoc comparisons. Correlation coefficients were estimated by linear or non-linear models (GraphPad Prism 5), as suggested by theoretical considerations and data appearance. $P< 0.05$ was used to define significance. Data are presented as mean±SEM.

Results

I_{E4031} replacement by mI_{Kr}

Action potentials were recorded at a cycle length of 1s (Figure 4.1) in control conditions (ctr). E4031 superfusion prolonged APD (+ 10.4 ± 2.1 %; $p<0.05$). As can be visually appreciated from Poincaré plots, E4031 significantly increased SD1 only (+ 38.6 ± 5.6 %; $p<0.05$) and SD1/SD2 became accordingly larger (+ 33.1 ± 10.4 %; $p<0.05$). This indicates that I_{Kr} blockade preferentially augmented the "faster" (beat-to-beat) component of APD variability (see also Appendix B). DC was then activated in the continuing presence of E4031 and mI_{Kr} was injected. This shortened APD by 13.1 ± 1.5% and fully restored action potential profile, to make it precisely overlap control one (inset Figure 4.1a). mI_{Kr} injection reduced

SD1 (-31.1 ± 3.2 % p <0.05 *vs* E4031) back to control (NS *vs* control) and SD2 below control (-10.6 ± 6.2 %; p<0.05 vs control). Thus, mI_{Kr} failure to restore SD1/SD2 was only apparent, reflecting further elimination of a slower component of variability, rather than the persistence of the faster component. Only for this subtle aspect mI_{Kr} diverged from native I_{Kr}.

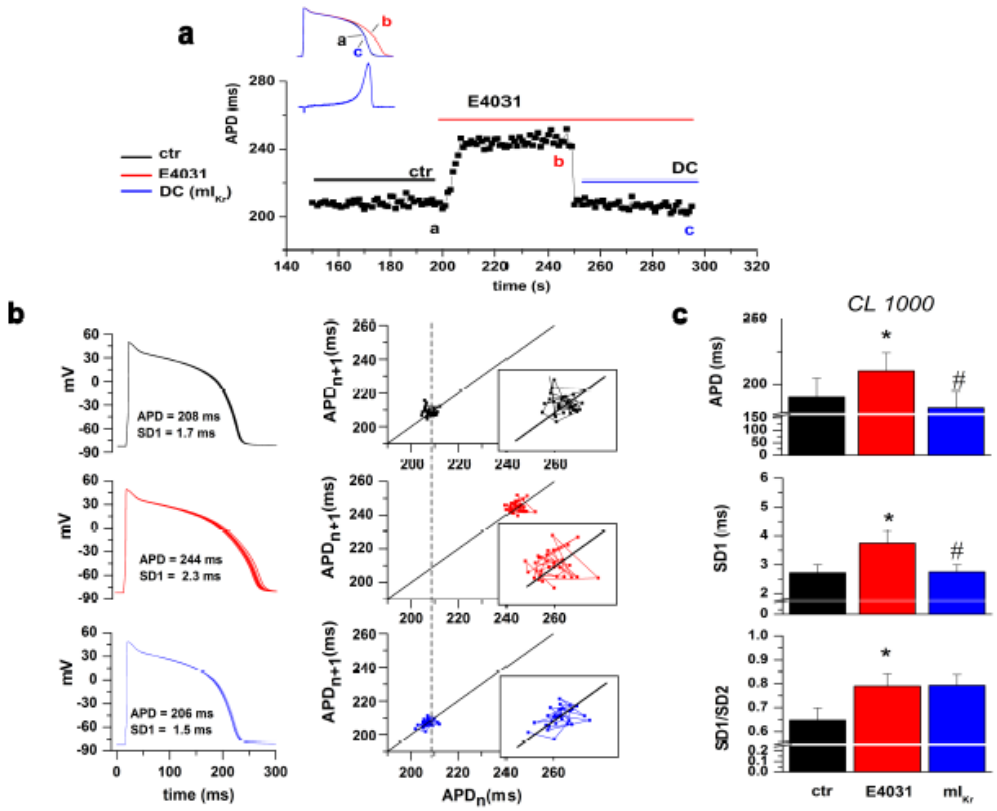

Figure 4.1. mI_{Kr} injection reverts E4031 effects

a) Representative time series of APD in control (a, black), during superfusion of E4031 (b, red) and during injection of mI_{Kr} (c, blue). In the inset, example of red and blue traces showing the injection of mI_{Kr} which reverts APD prolongation in the presence of E4031; **b)** 10 AP aligned waveforms, recorded in the three conditions, are shown with APD and SD1 average values; Poincaré plots, in parallel, evidence the dispersion of all APD values respect to the identity line (insets) and the mean APD referred to the control condition (dot line); **c)** statistics of APD, SD1 and SD1/SD2in all experimental conditions (p<0.05; **vs* ctr, # *vs* E4031; n= 23).

Correlation between APD and its variability

Proportionality between SD1 and mean APD is an *intrinsic* system property (see introduction) and can thus be expected. To investigate whether such proportionality was perturbed by I_{Kr} blockade and restored to control by mI_{Kr} injection, single SD1 values

recorded under the three conditions (control, E4031, mI_{Kr}) were pooled and plotted against the corresponding mean APD values (Figure 4.2a). Pooled data were then fitted by a linear function and raw residuals (i.e. with their sign; rR) were summed separately for each condition. Bar graphs (panel b) show that the sum of raw residuals (ΣrR) was close to null for control and mI_{Kr}, to become large and positive for E4031. This implies that, under I_{Kr} blockade, SD1 dependency on mean APD deviated from the general pattern. SD1 vs APD relationships were then fitted separately for each condition. The regression coefficient (slope) was similar between control and mI_{Kr}, but significantly larger for E4031; intercept values were similar in all conditions (Figure 4.2c). This indicates that, under I_{Kr} blockade, SD1 increment was larger than that expected from its intrinsic dependency on mean APD. Nevertheless, mI_{Kr} injection restored the control pattern; thus, the stabilizing effect of I_{Kr}, unveiled by this analysis, was necessarily based on I_{Kr} properties represented in the numerical model.

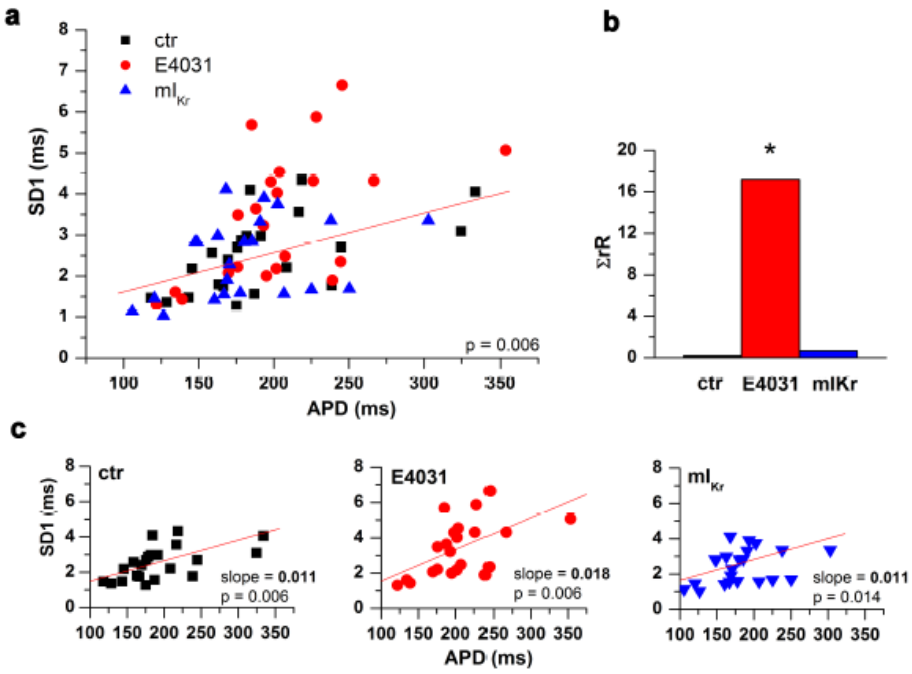

Figure 4.2. APD vs SD1 correlation

a) Plot of data pooled from all experimental conditions with the overall regression line; **b)** sum of raw residuals (ΣrR) from the plot in a; **c)** plots of data for each condition with the respective regression lines.

Impact of mI_{Kr} features on APD and its variability

In this section, different mI_{Kr} versions were prepared by changing gating parameters symmetrically around their value obtained from model optimization (control). The different models were applied under DC in the presence of E4031; APD and SD1 were measured from 40 APs in each condition; in all Figures control is represented in black, the negative parameter change in red and the positive change in blue. Maximal conductance (g_{max}), mid-potentials for steady-state activation ($V_{0.5}A$) and inactivation ($V_{0.5}I$) and activation/deactivation time-constant (τ) were considered.

Changes in maximal conductance (g_{max})

To evaluate the impact of I_{Kr} conductance, g_{max} was changed by ± 30 % (± Δ) from its control value (0.032 mS/µF).

A representative example of the effect of g_{max} changes in a single myocyte is shown in Figure 4.3a-c. Panel a shows time series of APD values under control (0.032 mS/µF), -Δ and +Δ. In this myocyte, -Δ did not change APD appreciably, but increased its variability; +Δ slightly reduced APD, but not its variability (average APD and SD1 values for this myocyte are shown under the traces in panel b). Panel c illustrates average mI_{Kr} profile of the myocyte under the three conditions; mI_{Kr} is plotted as function of time (I/t plot aligned with the corresponding average AP waveform) and as a function of V_m (I/V plot). The increase in mI_{Kr} amplitude can be appreciated from both plots. The I/V plot shows that g_{max} changes simply "scaled" current amplitude (I_{peak}), without affecting current profile; indeed, the voltage at which mI_{Kr} was maximal was unchanged (V_{peak}; Table 4.1). Therefore, the apparent shift of mI_{Kr} observed in the I/t plot was secondary to the slight AP shortening/prolongation occurring in this myocyte.

Statistics from 15 cells (Figure 4.3d) indicate that a 30% decrease of g_{max} did not affect APD significantly, but caused an appreciable increase of both SD1 (red *vs* black) and SD2, SD1/SD2remaining unchanged (Table 4.1). Neither APD, nor its variability were significantly changed by a g_{max} increment of the same magnitude (+Δ).

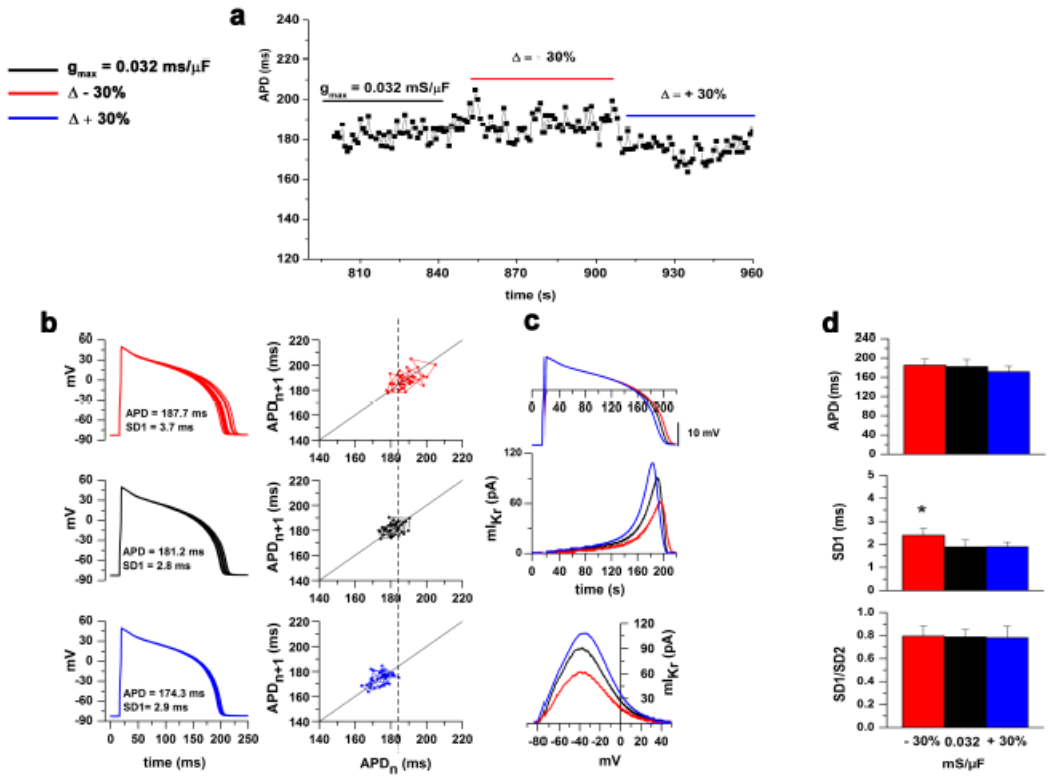

Figure 4.3. Changes in maximal conductance

Recordings performed at three values of g_{max} (0.032 mS/µF and Δ ± 30% in colour) are shown as: **a)** example of 40 APD over time; **b)** 10 AP aligned waveforms are shown with APD and SD1 average values; Poincaré plots, in parallel, evidenced the dispersion of all APD values respect to the identity line and the mean APD referred to the control condition (dot line); **c)** mI_{Kr} profile aligned with the corresponding average AP waveform represented as I/t and I/V_m plots; **d)** statistics of APD, SD1 and SD1/SD2 in all experimental conditions (*p<0.05 *vs* ctr, n = 11).

Table 4.1. Effect of changes in model parameters (g_{max}, $V_{0.5}A$, τA, $V_{0.5}I$) on mI_{Kr} features, APD and its variability.

Model parameters	**-Δ**	**DC**	**+Δ**	**# cells**
g_{max} (mS/µF)	**-30%**	**0.032**	**+30%**	
V_{peak} (mV)	-40.8 ± 0.47	-41.7 ± 0.24	-41.8 ± 0.21	
I_{peak} (pA/pF)	0.69 ± 0.04 *	0.91 ± 0.04	1.24 ± 0.03 *	≥ 8
TTP (ms)	196.3 ± 12	196.5 ± 11.9	180.4 ± 11.4 *	
$V_{0.5}A$	**-15 mV**	**-20.6**	**+15 mV**	
V_{peak} (mV)	-41.8 ± 1.4	-41.6 ± 0.3	-33.5 ± 0.26 *	
I_{peak} (pA/pF)	0.97 ± 0.01 *	0.93 ± 0.01	0.76 ± 0.01 *	= 8
TTP (ms)	182.2 ± 13	175.9 ± 11.3	177.5 ± 13.7	
$V_{0.5}I$	**-15 mV**	**-30.7**	**+15 mV**	
V_{peak} (mV)	-49.7 ± 0.38 *	-41.5 ± 0.24	-31.3 ± 0.17 *	
I_{peak} (pA/pF)	0.66 ± 0.004 *	0.97 ± 0.007	1.33 ± 0.003 *	≥ 7
TTP (ms)	184.3 ± 10.1	172.6 ± 11.5	133.9 ± 7.04 *	
τA	**100 ms**	**270**	**400 ms**	
V_{peak} (mV)	-39.6 ± 0.5 *	-42 ± 0.1	-42.6 ± 0.1	
I_{peak} (pA/pF)	0.88 ± 0.01 *	0.96 ± 0.01	0.98 ± 0.01	≥ 5
TTP (ms)	163.5 ± 12	164.6 ± 10.9	166 ± 12.9	

Changes in mid-activation voltage ($V_{0.5}A$)

To evaluate the impact of changes in the V-dependency of steady-state activation, the midpoint of the mI_{Kr} activation curve ($V_{0.5}A$) was shifted by ± 15 mV (± Δ) from its control value (-20.6 mV). According to simple reaction kinetics, shifts in the distribution of states at equilibrium may be associated to similar shifts in the velocity of transitions between states. Therefore, the curves defining V-dependency of activation time constants (τ) were concomitantly shifted by ±15 mV (Figure 4.4a). The less likely alternative condition, in which

shifts in steady-state activation occur without concomitant changes in V-dependency of τ, was tested in a separate series of experiments reported in the Appendix B (Figure S3 and Table S3).

An example of the effect of changes in $V_{0.5}A$ is shown in Figure 4.4b-d. Panel b shows time series of APD values under control (-20.6 mV), -Δ and +Δ. In this myocyte, +Δ slightly prolonged APD and measurably increased its variability; -Δ failed to affect APD and its variability appreciably. Panel d illustrates the average mI_{Kr} profile of the myocyte under the three conditions. The I/V plot shows that mI_{Kr} profile was markedly changed by +Δ and, to a lesser extent, by -Δ. Indeed, +Δ, decreased peak mI_{Kr} and shifted V_{peak} to less negative potentials ($p<0.05$); -Δ only slightly increased mI_{Kr} availability at potentials corresponding to repolarization phase 3 (I_{peak} and V_{peak} in Table 4.1). Because of the small changes in APD, mI_{Kr} traces almost overlap in the I/t plot, where only a change in peak current amplitude can be appreciated for +Δ.

Statistics from 8 cells (Figure 4.4e) indicated that a -15 mV shift in $V_{0.5}A$ (accompanied by shifts in τ curves) failed to affect APD, SD1 and SD1/SD2significantly. A positive shift in $V_{0.5}A$ also failed to affect APD, but increased SD1; SD1/SD2 also showed a trend to increase, very close to statistical significance.

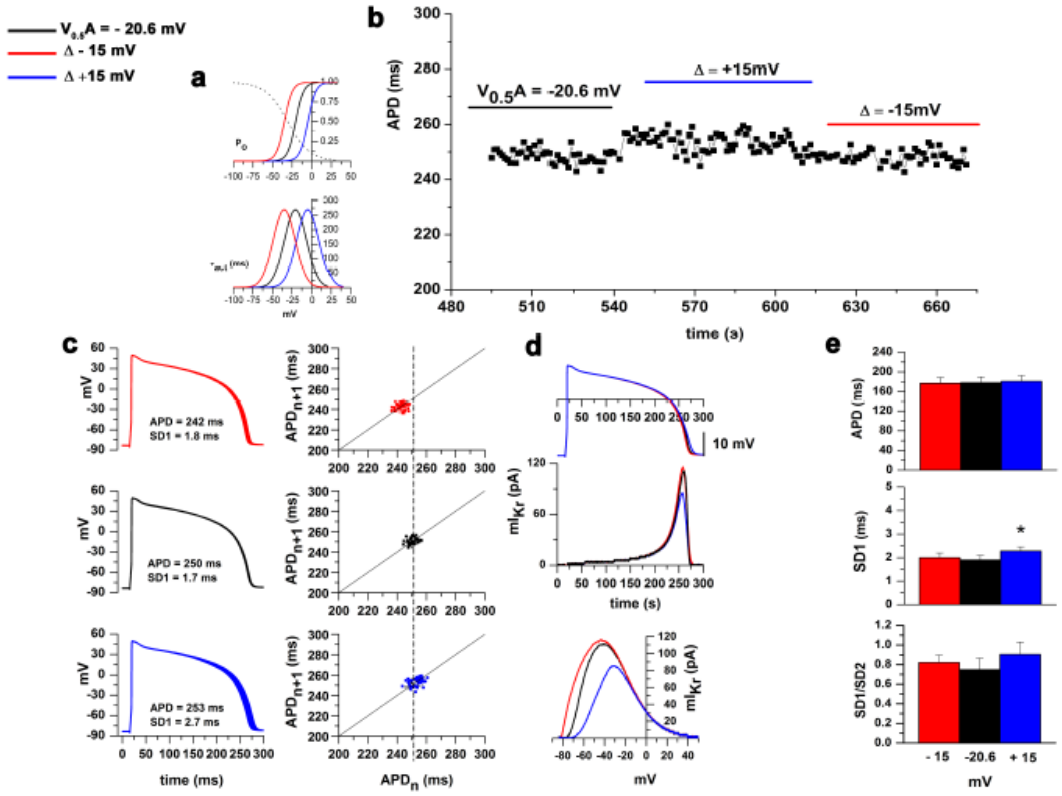

Figure 4.4. Changes in steady-state activation

Recordings performed at $V_{0.5}A$ = -20.6 mV and with Δ ± 15 mV are shown as: **a)** Steady-state activation (Po) and $\tau_{act/deact}$ V-dependency curves computed by the model in three conditions (colour); inactivation curve are superimposed as dot line; **b)** representative time course of APD recorded at three values of $V_{0.5}A$; **c)** example of 10 APs for each conditions with relative APD and SD1 values and Poincaré plot at the right of panel; ctr APD is evidenced as dot line; **d)** mI_{Kr} profile aligned with the corresponding average AP waveform represented as I/t and I/V_m plots; **e)** statistics of APD , SD1 and SD1/SD2in all experimental conditions (* *vs* control value; $p<0.05$, n = 8).

Changes in mid-inactivation voltage ($V_{0.5}I$)

To evaluate the impact of changes in the V-dependency of steady-state inactivation, the midpoint of the mI_{Kr} inactivation curve ($V_{0.5}I$) was shifted by ± 15 mV (± Δ) from its control value (-30.7 mV, Figure 4.5a, black line). Because mI_{Kr} inactivation was instantaneous, no kinetic considerations apply to this section.

An example of the effect of changes in $V_{0.5}I$ is shown in Figure 4.5b-d. Panel b shows time series of APD values under control (-30.7 mV), -Δ and +Δ. -Δ strongly prolonged APD and its variability; +Δ produced quantitatively similar changes but of opposite direction, i.e. it shortened APD and decreased its variability. Panel d illustrates average mI_{Kr} profile under the

three conditions; mI_{Kr} is plotted as function of time and as a function of V_m (I/V plot). The I/V plot shows that, at variance with activation (above), positive and negative shifts of inactivation changed mI_{Kr} profile almost symmetrically. According to statistics from 10 myocytes, +Δ increased peak mI_{Kr} ($p<0.05$) and shifted V_{peak} by +10.2 mV ($p<0.05$); -Δ decreased peak mI_{Kr} ($p<0.05$) and shifted V_{peak} by – 8.2 mV ($p<0.05$), i.e to a value corresponding to the steeper portion of phase 3 repolarization (I_{peak} and V_{peak} in Table 4.1). As shown in Figure 4.5e, this resulted in significant concordant changes in both APD and SD1 (when APD prolonged SD1 increased and viceversa). SD1/SD2was unchanged in the case of -Δ, and showed only a trend to decrease for +Δ.

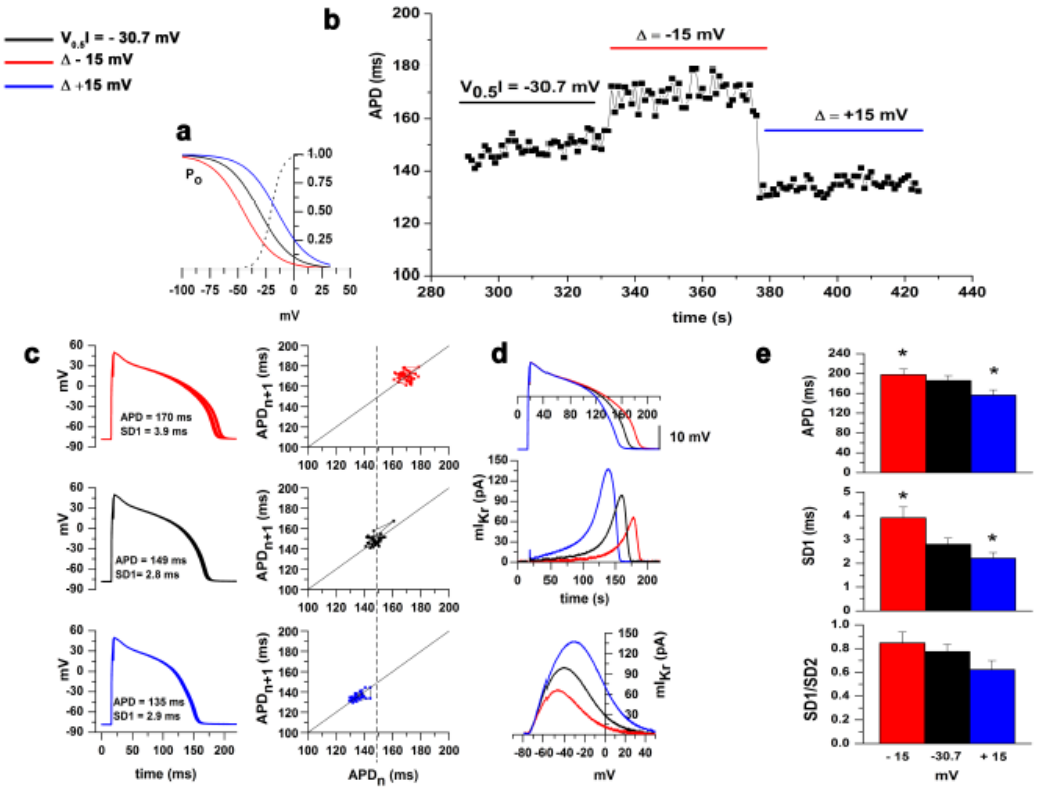

Figure 4.5. C**hanges in steady-state inactivation**

Recordings performed at $V_{0.5}A$ = -30.7 mV and with Δ ± 15 mV are shown as: **a)** Steady-state inactivation (Po) V-dependency curves computed by the model in three conditions (colour); activation curve are superimposed as dot line; **b)** representative time course of APD recorded at three values of $V_{0.5}I$; **c)** example of 10 APs for each conditions with relative APD and SD1 values and Poincaré plot at the right of panel; ctr APD is evidenced as dot line; **d)** mI_{Kr} profile aligned with the corresponding average AP waveform represented as I/t and I/V_m plots; **e)** statistics of APD , SD1 SD1/SD2in all experimental conditions (* *vs* control value; $p<0.05$, n = 12).

Changes in activation/deactivation time constant (τ)

To evaluate the impact of I_{Kr} activation/deactivation kinetics, the time constant (τ) was scaled at all potentials to 400 ms (+Δ) or 100 ms (-Δ) from its control value (270 ms, Figure 4.6 black line). All the parameters analyzed in the previous sections were not affected by the changes in τ, except for the voltage at which peak mI_{Kr} was achieved (V_{peak}), which was shifted from -42 ± 0.1 to -39.6 ± 0.5 mV by -Δ (n=5 $p<0.05$) and was unaffected by +Δ.

Statistics from 10 cells (Figure 4.6e) indicated that these rather wide τ changes did not measurably affect APD, SD1 or SD1/SD2.

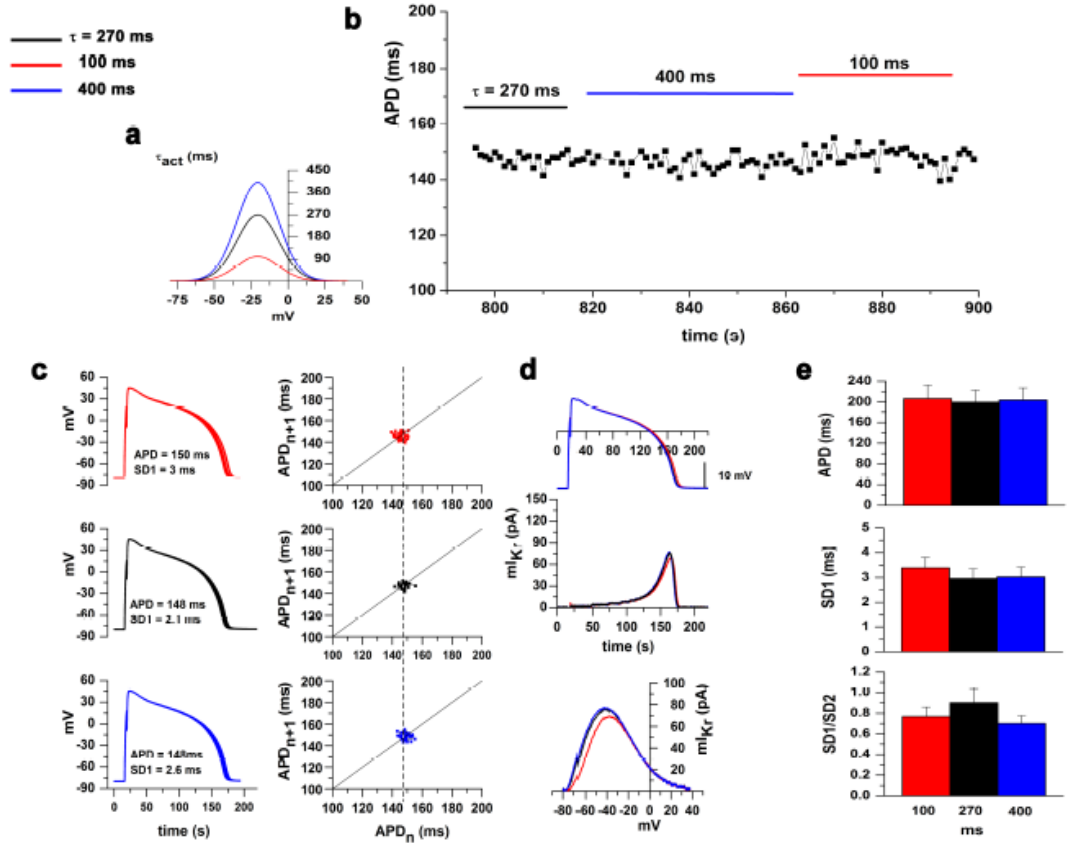

Figure 4.6 Changes in activation/deactivation kinetics

Recordings performed at τ = 270, 100 and 400 ms are shown as: **a)** $\tau_{act/deact}$ V-dependency curves computed by the model (colour); **b)** representative time course of APD recorded at three values of τ; **c)** example of 10 APs for each conditions with relative APD and SD1 values and Poincaré plot at the right of panel; ctr APD is evidenced as dot line; **d)** mI_{Kr} profile aligned with the corresponding average AP waveform represented as I/t and I/V_m plots; e) statistics of APD , SD1 and SD1/SD2 in all experimental conditions (* *vs* control value; $p<0.05$, n = 8).

Changes in mI_{Kr} distribution during repolarization

Repolarization course was divided in 3 phases, as described in Methods and shown at the top of Figure 4.7. mI_{Kr} present within each phase was quantified as mean current (I_{mean}) in a representative subset of myocytes (n=5). Figure 4.7a reports the changes of I_{mean} produced within each phase (1, 2 or 3) by changes in mI_{Kr} parameters; the corresponding changes in overall I_{mean} (I_{mean}tot) are shown in the insets of each panel. Under baseline conditions (black), I_{mean} increased from phase 1 to 3. Modulation of g_{max} (left; -Δ red, +Δ blue) similarly affected I_{mean} throughout the 3 phases; the effect was asymmetrical, i.e. larger for g_{max} reduction. Modulation of $V_{0.5}$A (center), almost exclusively concerned I_{mean} during Phase 3, with larger effect resulting from the positive shift (blue). Modulation of $V_{0.5}$I affected to some extent I_{mean} during all phases but, unlike g_{max}, sharply prevailed during Phase 1; negative (red) and positive (blue) $V_{0.5}$I shifts exerted roughly symmetrical effects .

Comparison of Figure 4.7a with Figure 4.7b allows to relate the above I_{mean} distribution patterns to APD and SD1 modulation (shown in Figures 4.3-4.6), represented for this purpose as % change from baseline values. For all parameters, the extent of APD changes correlated with changes in I_{mean} during Phase 2. On the other hand, the extent of SD1 changes correlated with changes in I_{mean} during Phase 3.

The format used in Figure 4.7b also highlights that, whereas significant changes in APD were achieved only by modulating $V_{0.5}$I, SD1 was affected by modulation of all parameters. Furthermore, the effects of symmetrical changes in g_{max} or $V_{0.5}$A produced strongly asymmetrical effects on SD1.

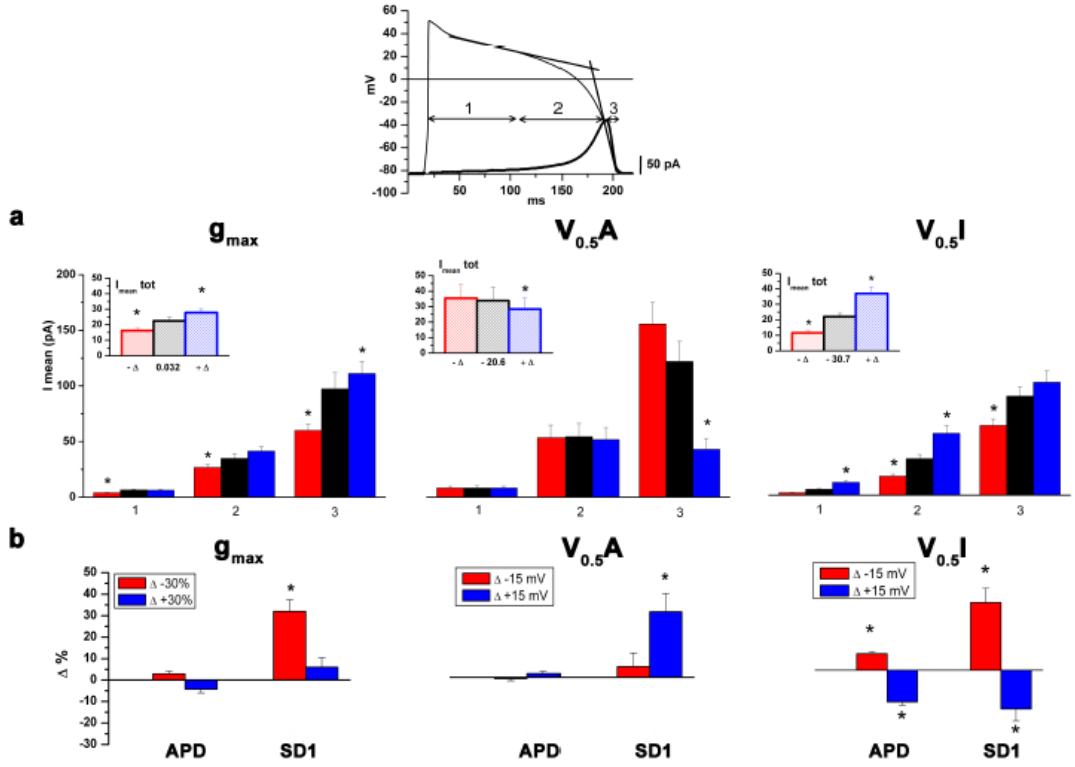

Figure 4.7. **Relationship between mI_{Kr} distribution and repolarization changes**

Quantification of mI_{Kr} (I_{mean}) during three AP phases (1, 2 or 3 as shown at the top). **a)** effect of changes (Δ) in mI_{Kr} parameters (g_{max}, $V_{0.5}A$, $V_{0.5}I$) on I_{mean} within each AP phase . (black = baseline, red = – Δ and blue = + Δ); changes in overall I_{mean} (I_{mean}tot) are shown in the inset of each panel (n = 5); **b)** response of APD and SD1 (as Δ% vs control) to changes in mI_{Kr} parameters (as above). * $p<0.05$ vs baseline.

Discussion

The main findings of this study include: 1) injection of modelled I_{Kr} (mI_{Kr}) fully reversed the increments in APD and its variability induced by I_{Kr} blockade; 2) repolarization was most sensitive to inactivation shifts, which concordantly affected APD and its variability; 3) similar changes in activation gating had marginal impact on APD but, when leading to mI_{Kr} decrement, significantly increased APD variability; 4) a similar pattern was observed for changes in maximal conductance. 5) even if SD1 showed a clear-cut dependency on APD, I_{Kr} blockade increased SD1 more than expected by APD prolongation alone (Figure 4.2); moreover, some among I_{Kr} perturbations changed SD1 without affecting APD significantly.

A question addressed by the present study is whether some yet unidentified properties of HERG channels may account for the major impact of I_{Kr} modulation on APD and its stability.

Adequacy of mI_{Kr} injection in reversing the effects of endogenous I_{Kr} blockade suggests that I_{Kr} properties incorporated in the model are sufficient to account for I_{Kr} functional contribution, except for what concerns the frequency content of APD variability (mI_{Kr} failed to restore SD1/SD2, Figure 4.1c). The present results also show that rather substantial changes in I_{Kr} V-dependency, e.g. those caused by activation shifts (Figure 4.4), may have a negligible impact on APD. Therefore, mean APD is a rather lax reporter of I_{Kr} abnormalities, APD variability being remarkably more sensitive. Notably, a fully deterministic I_{Kr} model, such as mI_{Kr}, also reversed the effects of endogenous I_{Kr} blockade on APD variability. This might suggest that the latter may not arise primarily from intrinsic (stochastic) I_{Kr} variance; however, specifically designed experiments may be required to define this aspect.

As previously reported [13], I_{Kr} blockade increased APD variability, mainly its beat-to-beat component (increased SD1/SD2). mI_{Kr} restored SD1 but not the SD1/SD2 ratio; this was because mI_{Kr} returned SD1 to control values, but further reduced SD2 ($p<0.05$, not shown). This observation may suggest failure of mI_{Kr} to reproduce sensitivity of native I_{Kr} to yet unidentified factors exerting their effect over multiple cycles (e.g. changes in the intracellular milieau) and thus contributing mostly to SD2.

SD1 has been identified as a powerful predictor of Torsade de Pointes [13], leading to the suggestion that beat-to-beat APD variability may favor arrhythmogenesis. However, because of their strong covariance (see Appendix B), SD1 and SD2 can hardly discriminate between beat-to-beat and slower forms of APD variability. Indeed, their ability to identify torsadogenic conditions is reported to be at least grossly similar by other studies [12, 13]. The numerical simulation reported in the Appendix B indicate that the SD1/SD2 ratio may provide a better chance to identify changes in beat-to-beat variability selectively; however, its prognostic value remains to be assessed.

The strong and concordant sensitivity of APD and its variability to inactivation shifts points to “rectification” as the I_{Kr} gating property which, if altered, is most likely to result in overt repolarization abnormality. Notably, APD shortening by positive inactivation shift was larger than APD prolongation resulting from the symmetrical negative shift (Figure 4.5b and 4.5e); this is consistent with incomplete rectification being the only mechanism thus far identified for Short-QT syndromes linked to HERG mutations [14]. SD1 changes were more conspicuous for the negative inactivation shift instead (Figure 4.5b and 4.5e), thus reinforcing the view that effects on APD and on its variability are not necessarily concordant. Negative inactivation shifts are a common feature of the subset of LQT2 mutants in which loss of

function is caused primarily by gating abnormalities, i.e. those in which channel density is preserved [15].

When including shifts in τ V-dependency, activation shifts had a clearly discernible effect on mI_{Kr} I/V plots, but a surprisingly small one on APD (Figure 4.4e). Nevertheless, the positive shift, which resulted in a clear-cut reduction in peak mI_{Kr}, significantly increased SD1. Notably, when the V-dependency of τ remained unchanged, the effects of activation shifts on SD1 disappeared, thus suggesting the importance of parallel changes in steady-state and kinetic behavior.

Down-regulation of channel expression or channel blockade (both represented by g_{max} reduction) are the most common I_{Kr} abnormality underlying QT prolongation [16]; therefore, the relatively small effect of g_{max} changes on APD (Figure 4.3d) was unexpected. Possibly the g_{max} changes considered here (± 30%) are small as compared to those occurring when QT prolongation is observed. Whereas g_{max} reduction increased significantly SD1, the latter was not affected by g_{max} increment (Figure 4.3d). While the association of I_{Kr} deficiency with increased APD variability is a well-established notion, this asymmetry was unexpected and a further example of how symmetrical changes in channel properties may result in asymmetrical AP responses. SD1/SD2 ratio did not significantly increase in response to decrements in g_{max}; this contrasts with its increment following blockade of native I_{Kr}. Again, this suggests that mI_{Kr} may not be fully representative of native I_{Kr} in terms of sensitivity to the type of perturbations reflected by SD2.

Mechanistic interpretation

The AP profile is ultimately determined by a feed-back loop linking membrane potential to the many (V-dependent) conductances contributing to total membrane current (I_m). Such a loop is preserved in DC mode; therefore, AP changes following modulation of an individual component of I_m (I_{Kr} in the present case) might be either buffered or boosted by the feed-back response of other components. We will refer to this phenomenon as "*active*" response of AP to I_{Kr} perturbation. An additional factor to be considered in interpreting the observed effects is non-linearity of the relationship between I_m ($\propto dV/dt$) and APD ($\propto (dV/dt)^{-1}$). Being merely numerical, this has been referred to as an "*intrinsic*" property of the system, of general value and independent of the components underlying the "*active*" response [17, 18]. A relevant

consequence of the *intrinsic* property is that a given change in I_m is expected to affect APD more if it occurs during a slow phase of repolarization (Figure 5 in ref [17]) .

During phase 1, current balance is dominated by the match between non-inactivating I_{CaL} and I_{Na} components and I_{Ks} onset, which yields a relatively small I_m, i.e. slow repolarization. The fragility of this phase resides precisely in the fact that, being I_m small (in the order of 0.3 pA/pF), it can be easily doubled, or halved, by even minor current changes. Since dV/dt and I_m are linearly related, the same applies to repolarization rate. Thus, high APD sensitivity to I_{Kr} changes occurring in this phase is expected as the consequence of system's *intrinsic* property [18].

Current theories on the genesis of early-afterdepolarizations (EADs) points to phase 2 as the one in which *active* responses are in a more delicate balance. Indeed, in this phase, the outward current surge supported by I_{Kr} matches the inward "resurgent" components of I_{CaL} and $I_{Na,,}$ which are prone to autoregenerative reactivation. Furthermore, rather dramatic changes in sub-sarcolemmal ionic (Ca^{2+} and Na^{+}) concentrations occur in this phase and even subtle changes in their match with membrane potential may affect the sign and magnitude of the current carried by NCX. Thus, we would expect Phase 2 to be a major source of SD1 through system's *active* property [12].

With its large dV/dt, resulting from auto-regenerative recovery of inward-rectifying K^{+} currents (I_{Kr} and I_{K1}), Phase 3 would be expected to be relatively immune to current perturbations.

Analysis of the patterns shown in Figure 4.7 are largely, but not entirely coincident with such theoretical expectations. The only intervention changing APD substantially was modulation of inactivation midpoint ($V_{0.5}I$), i.e. the one with the largest effect on mI_{Kr} during Phase 1. This fulfills the expectation that current changes during slow repolarization may have a larger impact on APD (*intrinsic* property; see above). On the other hand, contrary to the expectations discussed above, SD1 was more affected by mI_{Kr} changes during Phase 3 than by those occurring during Phase 2. This discrepancy might be at least in part explained by observing that mI_{Kr} was substantially larger, and more strongly affected by the interventions considered, during Phase 3 than during Phase 2. Nevertheless, this finding argues against a role of I_{Kr} in setting the stability of repolarization during Phase 2.

Limitations

The whole experimental approach used in this study relies on the assumption that I_{E4031}, on which mI_{Kr} was optimized, accurately reflects I_{Kr}. This requires E4031 selectivity for I_{Kr} and constancy of E4031 block throughout the electrical cycle. Whereas at the concentration used, E4031 is indeed selective [19], block voltage-dependency might theoretically distort the current profile during the AP. Nevertheless, the kinetics of V-dependent E4031 binding and unbinding are very slow [20], thus ensuring that, after block has achieved steady-state during repetitive depolarization at physiological cycle lengths, it will remain constant throughout the electrical cycle [21]. I_{E4031} recordings under AP-clamp were obtained under conditions allowing achievement of steady-state E4031 blockade. Thus, under the present conditions, close similarity between I_{E4031} and I_{Kr} can be reasonably assumed. A further issue is how accurately mI_{Kr} reproduces I_{E4031} properties. In this study mI_{Kr} parameters were optimized on I_{E4031} recorded during AP-clamp. This approach is more stringent than parameter estimation from traditional V-clamp protocols, because the current profile during AP-clamp closely depends on gating kinetic properties that might be otherwise incorrectly estimated.

Whereas native I_{Kr} inactivates with a time constant in the 1-4 ms range, in the sake of computational speed, mI_{Kr} inactivation was made instantaneous. This choice was motivated by the result of numerical simulations, presented in the Appendix B, showing that even large changes in inactivation time constant had a small impact on mI_{Kr} profile and no measurable effect on AP profile. Also, the effect of changes in activation time constant was similar whether inactivation was considered instantaneous or time-dependent (not shown).

Implications

Identification of the relative impact of I_{Kr} gating properties may provide a new framework for predicting the consequences of I_{Kr} mutations on APD and its variability, two quantities strongly associated with arrhythmogenic risk. If validated by correlation with clinical observations, such a framework would be of obvious practical use.

The present results point to a surprising lack of APD sensitivity in detecting I_{Kr} abnormalities and identify SD1 as a more sensitive index. This may be relevant to the choice of risk identifiers to be applied in mutation or drug screening. While the prognostic significance of SD1/SD2 awaits to be tested, its suitability to report on the frequency content of variability may help in the identification of the underlying mechanisms.

Being tested in the context of a real guinea-pig myocyte, the outcome of I_{Kr} modulation may represent a reference for validation of guinea-pig AP numerical models; detection of possible discrepancies would likely provide valuable information for overall model optimization.

Finally, by confirming/challenging theoretical expectations, the present results have refined our interpretation of the complex relation between current and repolarization abnormalities.

References

[1] Zareba W, Bayes d. QT dynamics and variability. Ann Noninvasive Electrocardiol 2005;10:256-62.

[2] Ortega FA, Butera RJ, Christini DJ, White JA, Dorval AD. Dynamic clamp in cardiac and neuronal systems using RTXI. Methods Mol Biol 2014;1183:327-54.

[3] Wilders R. Dynamic clamp: a powerful tool in cardiac electrophysiology. The Journal of physiology 2006;576:349-59.

[4] Flore V, R. W. T-wave alternans and beat-to-beat variability of repolarization: pathophysiological backgrounds and clinical relevance. Acta Cardiol 2012;67:713-8.

[5] Thomsen MB, Oros A, Schoenmakers M, van Opstal JM, Maas JN, Beekman JD, et al. Proarrhythmic electrical remodelling is associated with increased beat-to-beat variability of repolarisation. Cardiovasc Res 2007;73:521-30.

[6] Zaza A, Rocchetti M, Brioschi A, Cantadori A, Ferroni A. Dynamic Ca2+-induced inward rectification of K+ current during the ventricular action potential. Circ Res 1998;82:947-56.

[7] Luo CH, Rudy Y. A dynamic model of the cardiac ventricular action potential. I. Simulations of ionic currents and concentration changes. Circulation Research 1994a;74:1071–96.

[8] Zeng J, Laurita KR, Rosenbaum DS, Rudy Y. Two components of the delayed rectifier K+ current in ventricular myocytes of the guinea pig type. Theoretical formulation and their role in repolarization. Circ Res 1995;77:140-52.

[9] Wettwer E, Scholtysik G, Schaad A, Himmel H, Ravens UJ. Effects of the new class III antiarrhythmic drug E-4031 on myocardial contractility and electrophysiological parameters. Cardiovasc Pharmacol 1991;17:480-7.

[10] Rocchetti M, Besana A, Gurrola GB, Possani LD, Zaza A. Rate dependency of delayed rectifier currents during the guinea-pig ventricular action potential. The Journal of physiology 2001;534:721-32.

[11] Bartolucci C, Altomare C, Bennati M, Furini S, Zaza A, Severi S. Combined Action Potential and Dynamic-Clamp for accurate computational modelling of the cardiac IKr current. J Mol Cell Cardiol 2014;79:187-94.

[12] Heijman J, Zaza A, Johnson DM, Rudy Y, Peeters RL, Volders PG, et al. Determinants of beat-to-beat variability of repolarization duration in the canine ventricular myocyte: a computational analysis. PLoS Comput Biol 2013;9:e1003202.

[13] Thomsen MB, Verduyn SC, Stengl M, Beekman JD, de Pater G, van Opstal J, et al. Increased short-term variability of repolarization predicts d-sotalol-induced torsades de pointes in dogs. Circulation 2004;110:2453-9.

[14] Brugada R, Hong K, Dumaine R, Cordeiro J, Gaita F, Borggrefe M, et al. Sudden death associated with short-QT syndrome linked to mutations in HERG. Circulation 2004;109:30-5.

[15] Shao C, Lu Y, Liu M, Chen Q, Lan Y, Liu Y, et al. Electrophysiological study of V535M hERG mutation of LQT2. J Huazhong Univ Sci Technolog Med Sci 2011;31:741-8.

[16] Mehta A, Sequiera GL, Ramachandra CJ, Sudibyo Y, Chung Y, Sheng J, et al. Re-trafficking of hERG reverses long QT syndrome 2 phenotype in human iPS-derived cardiomyocytes. Cardiovasc Res 2014;102:497-506.

[17] Bányász T, Horváth B, Virág L, Bárándi L, Szentandrássy N, Harmati G, et al. Reverse rate dependency is an intrinsic property of canine cardiac preparations. Cardiovasc Res 2009;84:237-44.

[18] Zaza A. Control of the cardiac action potential: The role of repolarization dynamics. J Mol Cell Cardiol 2010;48:106-11.

[19] Sanguinetti MC, Jurkiewicz NK. Two components of cardiac delayed rectifier K+ current. Differential sensitivity to block by class III antiarrhythmic agents. The Journal of general physiology 1990;96:195-215.

[20] Spector PS, Curran ME, Keating MT, Sanguinetti MC. Class III antiarrhythmic drugs block HERG, a human cardiac delayed rectifier K+ channel. Open-channel block by methanesulfonanilides. Circ Res 1996;78:499-503.

[21] Hancox JC, Levi AJ, Witchel HJ. Time course and voltage dependence of expressed HERG current compared with native "rapid" delayed rectifier K current during the cardiac ventricular action potential. Pflügers Arch 1998;436:843-53.

CHAPTER 6

Use of Dynamic – clamp to compare different species: how a guinea – pig becomes dog

---

The content of this chapter has been published in:

Sala L, Hegyi B, **Bartolucci C**, Altomare C, Rocchetti M, Mostacciuolo G, Severi S, Szentandrassy N, Nanasy PP, Zaza A

Effects of species-dependent differences in action potential shape in setting β-adrenergic-stimulation induced current

Computing in Cardiology 2013, vol. 40, pp 381-384.

Abstract

In canine (D) and human, but not guinea pig (GP), ventricular myocytes, a spike-and-dome profile (SaD), supported by Ito, characterizes ventricular repolarization. β - adrenergic stimulation (by isoprenaline, ISO) shortens action potential (AP) duration (APD) in D (and human) myocytes, but prolongs it in GP ones.

***Aim**: The aim of this work was to clarify whether SaD is the main factor determining the direction of APD response to β - adrenergic stimulation.*

***Methods**: AP-clamp with D epicardial, D endocardial, and GP waveforms was applied at different diastolic intervals (DI) to measure ISO-induced current (I_{iso}) in GP myocytes. Dynamic Clamp was used to test the effect of I_{to} introduction, and of the resulting dog-like SaD, on ISO modulation of GP repolarization.*

***Results**: In AP-clamp at DI 1750 ms, I_{iso} was more inward with both D and GP waveforms. In Dynamic-Clamp, SaD introduction failed to change the direction of ISOinduced APD changes in GP myocytes.*

***Conclusions**: SaD profile alone may not account for differences between D and GP in terms of APD response to β - adrenergic-stimulation. Further differences of AP profile and/or diverse contributions of Ca^{2+} and K^{+} currents between the two species may be involved.*

Introduction

In cardiac myocytes, the action potential (AP) repolarization profile is species-dependent, reflecting differences in the underlying ionic currents. In human and canine (D) myocytes, but not guinea-pig (GP) ones, a spike-and-dome (SaD) profile characterizes initial repolarization. SaD consists of fast initial repolarization (supported by I_{to}), followed by a secondary depolarization, caused by the sum of I_{to} decay (inactivation) and ensuing I_{CaL} (re-activation). I_{to} expression and SaD prevail in sub-epicardial myocytes and, mainly because of slow I_{to} recovery, SaD magnitude is rate-dependent. The β - adrenergic agonist isoproterenol (ISO) elicits opposite effects on AP duration (APD) depending on cell type and pacing rate (see Figure 6.1) [1] . In canine epicardial (D-Epi) myocytes, with large SaD, ISO shortens APD; this is associated with marked elevation of the whole plateau phase. In canine endocardial (DENDO) myocytes, with small SaD, ISO leaves APD almost unchanged, with the dome only mildly elevated [1]. In GP myocytes, ISO prolongs APD with only minor effects on the early plateau level [2]. ISO effects on APD are larger at slow pacing rate, thus matching SaD rate-dependency.

Since AP contour results from a feed-back interplay between current and membrane potential, the effect of current modulation may well depend on the initial AP contour. Therefore, the correlation between SaD magnitude and APD response to ISO suggests that the two aspects might be causally related [1]. However, this hypothesis has never been directly tested. The aim of this work is to clarify whether the AP contour, in particular the presence of the SaD, may account for APD variations under β - adrenergic stimulation. If this was the case, conditions or interventions affecting SaD magnitude would be expected to deeply affect APD response to sympathetic activation, a conclusion of practical relevance.

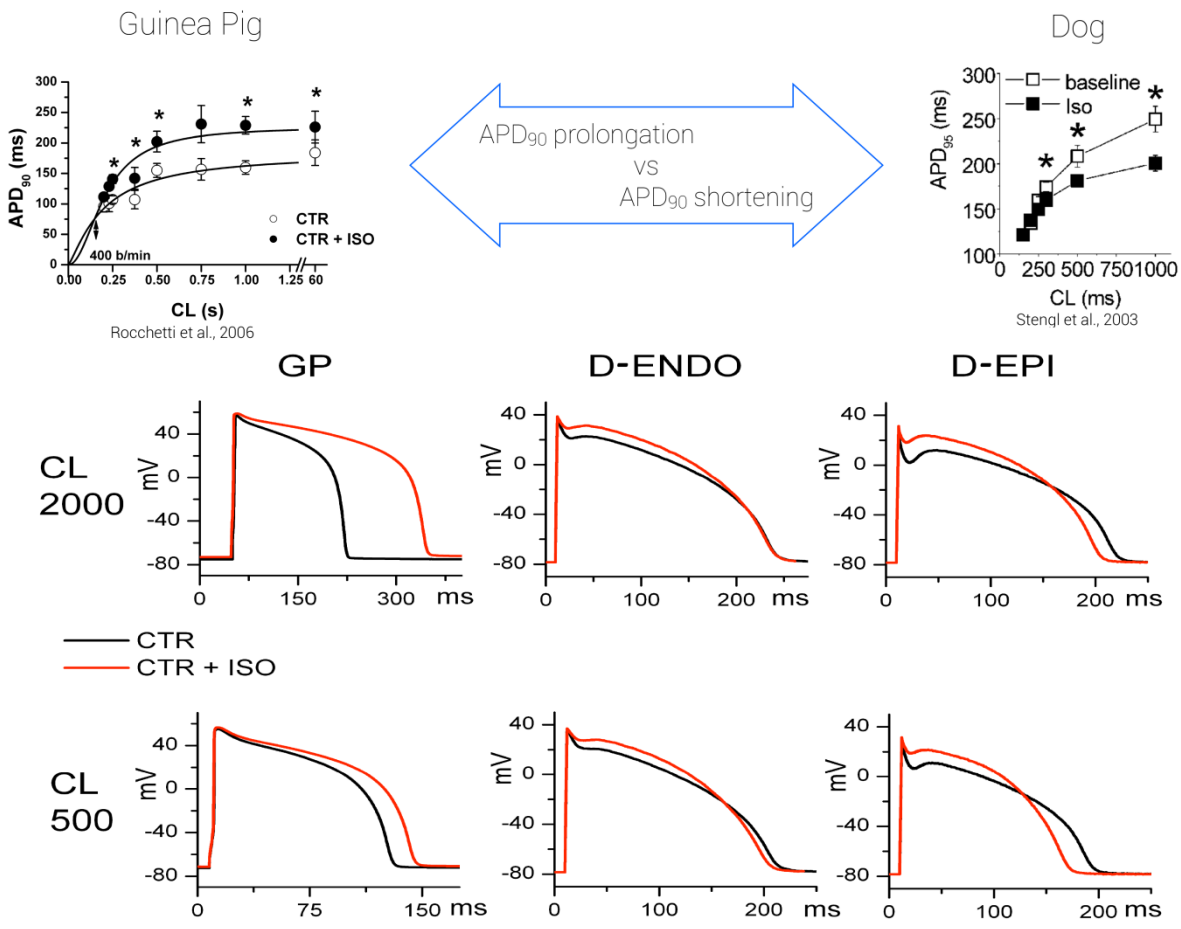

Figure 6.1. Comparison between the effects of ISO on action potential duration in guinea pig (GP) cardiomyocytes and in canine (D) ones.

Methods

This investigation conforms to the Guide to the Care and Use of Laboratory Animals published by the US National Institutes of Health (NIH publication no. 85-23, revised 1996) and to the guidelines for Animal Care endorsed by the Universities of Milan and Debrecen.

Adult Dunkin-Hartley GP were anesthetized by 100 mg/kg sodium thiopental and euthanised by cervical dislocation. Ventricular myocytes were isolated by using a retrograde coronary perfusion method previously published [2], with minor modifications.

Adult beagle dogs were anesthetized with intramuscular injection of 10 mg/kg ketamine HCl + 1 mg/kg xylazine HCl. Ventricular myocytes were dissociated by using the segment perfusion technique [1].

Membrane potential and current measurements

Measurements were performed by the patch-clamp technique in the whole-cell configuration at 36.5 ± 0.5°C. The pipette solution contained (mM): 100 K^+ Aspartate, 45 KCl, 0.4 $CaCl_2$, 3 $MgCl_2$, 5 HEPES, 1 EGTA, 0.4 $GTPNa^+$, 5 $ATP\text{-}K^+$, and 5 creatine phosphate Na^+, adjusted to pH 7.2 with KOH. Extracellular solution was composed (mM) by 144 NaCl, 5.6 KCl, 1.2 $MgCl_2$, 2.5 $CaCl_2$, 5 HEPES, 11 Glucose. pH was adjusted to 7.4 with NaOH. ISO was dissolved in this solution to obtain 10 nM concentration. Membrane capacitance (126.4 ± 19 pF) and series resistance were measured in every cell.

Current-clamp experiments

GP, DEPI and DENDO myocytes were paced at cycle length (CL) of 2000 ms. Action potentials were recorded (I-clamp mode; I =0) before and during steady-state exposure to ISO (10 nM). APD was measured at 90% repolarization. Average AP waveforms were obtained from at least 7 cells for each group after normalizing each record timescale to APD measured at 90% repolarization.

Action-potential clamp

Average AP waveforms from the different myocyte types (GP, DEPI and DENDO) were applied in V-clamp mode, at the relevant CLs, to GP myocytes. To avoid any influence of diastolic interval (DI), the latter was kept constant, i.e. made independent of APD changes, by suitably adjusting CLs. At steady-state stimulation, ISO (10 nM) was applied and ISO-induced current (I_{iso}) was evaluated by subtraction (I in ISO - I in control) [3].

Dynamic clamp

GP myocytes do not express I_{to}. A modelled I_{to}, suitable to reproduce canine SaD, was injected in GP myocytes by the dynamic-clamp technique [4]. In brief: an I_{to} numerical model was derived from Heijman's one [5], by considering only the I_{to1} component and adjusting parameters to reproduce in GP myocytes the SaD profile peculiar of DEPI myocytes at a CL of 2000 ms. Electrical activity was recorded from the GP myocyte at CL 2000 ms, fed to the I_{to} model; the modeled current was injected in the myocyte in a virtually real-time loop. The

response of myocyte AP to ISO could thus be recorded in the absence and presence of the SaD profile respectively.

Results

Current-clamp experiments: ISO effects on APD

This set of experiments tests the effect of ISO on spontaneously generated AP profiles in different cell types. Under this setting, reproducing the physiological condition, the feed-back between membrane current and potential is intact; thus both primary and secondary effects contribute to set the final AP contour (closed-loop condition). At CL 2000 ms, the effect of ISO on APD differed among GP, DEPI and DENDO cardiomyocytes. In GP myocytes ISO prolonged APD by 21 ± 2.5% ($p<0.05$). In DEPI myocytes ISO shortened APD by 15.4 ± 3.3% ($p<0.05$). In DENDO myocytes, ISO did not affect APD significantly (+1.58 ± 4.8%; NS).

AP-clamp experiments: ISO effects on membrane current

This set of experiments tests the effect of AP profile on the primary ISO-induced modification of membrane current, expressed as I_{iso}. As the AP profile is clamped, current cannot feed-back on AP to determine its secondary changes (open-loop condition). Repetition CL was adapted to keep DI constant at 1750 ms at the value observed in control at CL of 2000 ms. At this preliminary stage, AP-clamp data are available for GP myocytes only, i.e. the different AP profiles (GP, DENDO and DEPI) were all applied only to GP myocytes.

At DI 1750 ms I_{iso} profile markedly differed between native (GP) or canine waveforms. For all waveforms I_{iso} had an early inward ($-I_{iso}$) and a late outward ($+I_{iso}$) component. Under the GP waveform I_{iso} occurred through most of repolarization, and peaked at the transition between phases 2 and 3. $+I_{iso}$ was observed only during terminal phase 3. Under canine AP waveforms, I_{iso} appeared as a transient just after the AP upstroke, and it was significantly larger for the DENDO than for the DEPI waveform (mean $-I_{iso}$ 5.68 ± 0.67 vs 3.73 ± 0.53 pA/pF; $p<0.05$). $+I_{iso}$ appeared close to phase 2-3 transition (i.e. when $-I_{iso}$ was maximal under the GP waveform) and was comparable between DEPI and DENDO waveforms (mean $+I_{iso}$ 0.49 ± 0.07 vs 0.45 ± 0.12 pA/pF, NS).

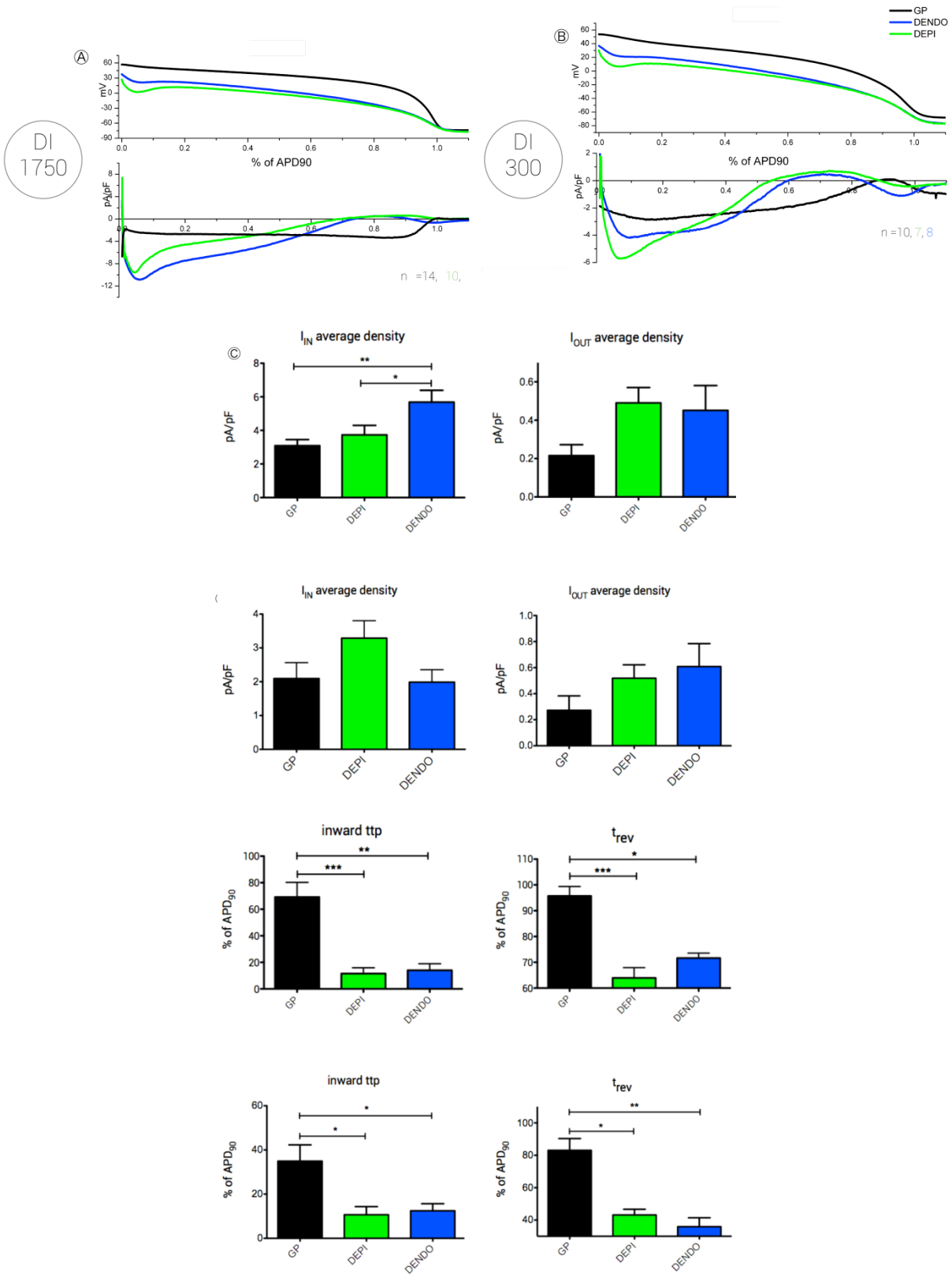

Figure 6.2. Action Potential - clamp: impact of AP contour on ISO-induced current

I_{ISO} recorded under GP (black), DENDO (blue) and DEPI (green) AP waveforms at two DIs (upper panels 1750 ms, lower panels 300 ms). **A** and **B**: sample I_{ISO} recordings at the two DIs; **C** and **D**: statistics of I_{ISO} features: I_{IN} = inward I_{ISO} component; I_{OUT} = outward I_{ISO} component; ttp = time to peak of I_{IN}; t_{rev}= time of reversal from I_{IN} to I_{OUT}. Times expressed as % of APD90.

Dynamic-clamp experiments: impact of SaD profile on APD response to ISO

In this set of experiments, albeit membrane current is changed by modelled current injection, the myocyte AP is recorded in I-clamp mode. Therefore this is again a closed-loop condition. In control conditions, introduction of the DEPI-like SaD profile shortened GP APD by 5.7 ± 3.4%, a result consistent with the APD prolonging effect of I_{to} blockade in canine myocytes [6]. Thus far, only preliminary data are available for the impact of SaD profile on ISO-induced APD modulation in GP myocytes at a CL of 2000 ms. According to these data, ISO prolonged GP APD similarly whether or not the SaD profile was introduced (+20.7 ± 1.8% vs +21.4 ± 2.5%; NS).

Moreover I_{to} injection, i.e. introduction of the "notch" in the GP AP did not modify ISO-induced APD prolongation (Figure 6.3). This suggests that the "notch" is not the only factor that influence ISO-induced APD variations.

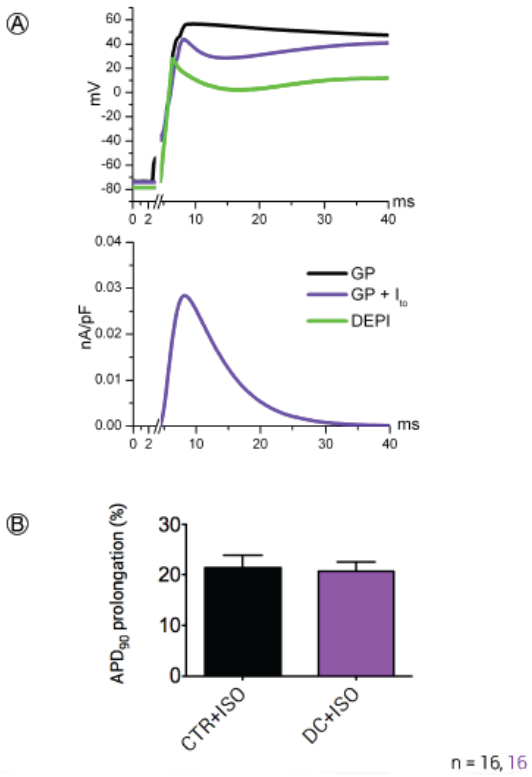

Figure 6.3. Impact of "notch" on modulation of APD by ISO

A and **B**: The effect of 10 nM ISO on APD of a GP myocyte stimulated at CL = 2000 ms was tested in control and during injection of modeled I_{to}.

Discussion

The data obtained can be summarized as follows: 1) in closed-loop conditions, ISO effects on APD are opposite between GP and DEPI myocytes; DENDO has an intermediate response; 2) in open-loop conditions, within a single species (GP) I_{iso} profile under GP, DEPI and DENDO waveforms substantially differs. The differences are concordant with the species-difference observed in close-loop conditions (i.e. the transition between inward and outward I_{iso} occurs earlier during the AP, as expected to shorten APD, when canine waveforms are applied; 3) introduction of the SaD profile is not adequate to switch GP APD response to ISO from prolongation to shortening.

Closed-loop (I-clamp) vs open-loop (AP-clamp) ISO effects

In GP myocytes, ISO changed plateau potentials only slightly, but markedly prolonged APD. This is consistent with $-I_{iso}$ being relatively small, but persisting almost to repolarization end. In canine myocytes, ISO-induced APD shortening correlates with the earlier switch between inward and outward Iiso, but occurs in spite of the prominent inward I_{iso} observed during the plateau phase. Although with differences in current magnitude, the I_{iso} pattern, shown here when DEPI waveforms were applied to GP myocytes, is very similar to that previously shown by applying DEPI waveforms to the canine myocytes from which they were recorded [1]. Therefore, I_{iso} pattern (or time-course) seems to be dictated mostly by AP profile, rather than by species differences in the kinetics of repolarizing currents.

On the other hand, I_{CaL} density is larger in GP myocytes [7, 8], thus accounting for the larger inward I_{iso} observed in GP (present data) as compared to dog [1]. Repetition of AP-clamp experiments in canine myocytes under conditions strictly uniform with those of the present study is currently ongoing to confirm this preliminary conclusion.

The mismatch between the prominent $+I_{iso}$ occurring during the plateau of DEPI waveform (open-loop) and ISO-induced APD shortening (closed-loop) necessarily calls into play secondary changes occurring as a consequence of membrane potential feed-back on current. Large inward I_{iso} is consistent by the observed ISO-induced plateau elevation; we speculate that the latter may in turn enhance I_{Ks} activation, thereby leading to overall APD shortening. Specifically designed experiments are required to confirm this hypothesis.

Role of the SaD in determining ISO effects on APD

Although preliminary, the present results seem to negate a central role of SaD in dictating APD response to ISO. This is apparently in contrast with [1] the recent observation that in midmyocardial myocytes I_{to} blockade (by 4-AP), and the consequent reduction of SaD magnitude, blunts ISO-induced APD shortening. While the role of 4-AP ancillary effects cannot be ruled out, the discrepancy deserves a more careful discussion. In the present experiments, SaD was introduced in the context of a GP action potential, featuring a plateau phase substantially positive as compared to that of DEPI myocytes. Moreover, whereas ISO globally elevated the plateau in DEPI myocytes, it only affected its repolarization velocity in GP myocytes. The impact of SaD may theoretically differ between the two contexts. Furthermore, as judged from the differences in I_{iso} profile between GP and canine waveforms (Figure 6.2A), SaD, possibly in combination with the lower plateau, strongly enhances early inward current, but it accelerates its reversal, an effect indeed compatible with APD shortening. Therefore, from the present preliminary data we can at best conclude that SaD insertion per se is not adequate to shift APD response in GP myocytes. This, in fact, does not negate a role of SaD (and I_{to}) in ISO-induced APD shortening in canine myocytes. Experiments results designed to assess the role plateau level in determining APD response to ISO are shown in Figure 6.4-5.5. More negative plateau levels enhanced inward I_{iso} components during early repolarization and accelerated its decay. Nevertheless, I_{iso} reversal was not significantly anticipated, thus suggesting that I_{IN} enhancement by the “notch”, as in Figure 6.2, may be required. In DC condition, a plateau level close to canine values did not alter the response to ISO, indicating that the plateau elevation following ISO superfusion is mandatory to short APD_{90}. Furthermore, DC data confirmed AP-clamp data in Figure 6.4.

The previously reported contribution of SaD in setting I_{CaL} time-course [7] is confirmed by the present AP-clamp recordings (Figure 6.2) showing larger but more quickly reversing inward I_{iso} under canine AP waveforms.

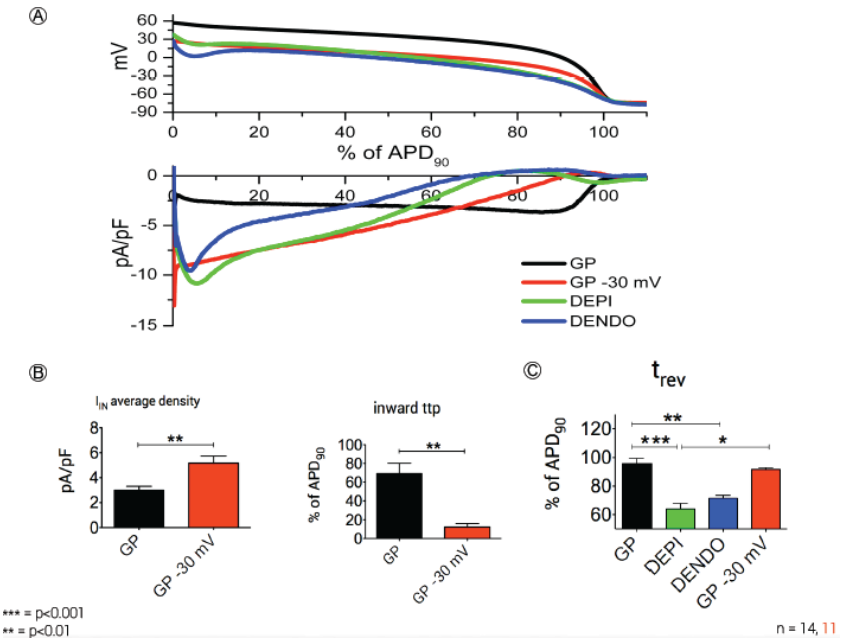

Figure 6.4. Impact of plateau voltage on ISO-induced current

Comparison of I_{iso} between normal GP AP (black) and after "lowering" its plateau phase to voltages comparable to those peculiar of DEPI AP (cyan). **A**: sample I_{iso} recordings; **B** and **C**: statistics of I_{iso} features. I_{IN} = inward I_{iso} component; I_{OUT} = outward I_{iso} component; ttp = time to peak of I_{IN}; trev= time of reversal from I_{IN} to I_{OUT}. Times expressed as % of APD90.

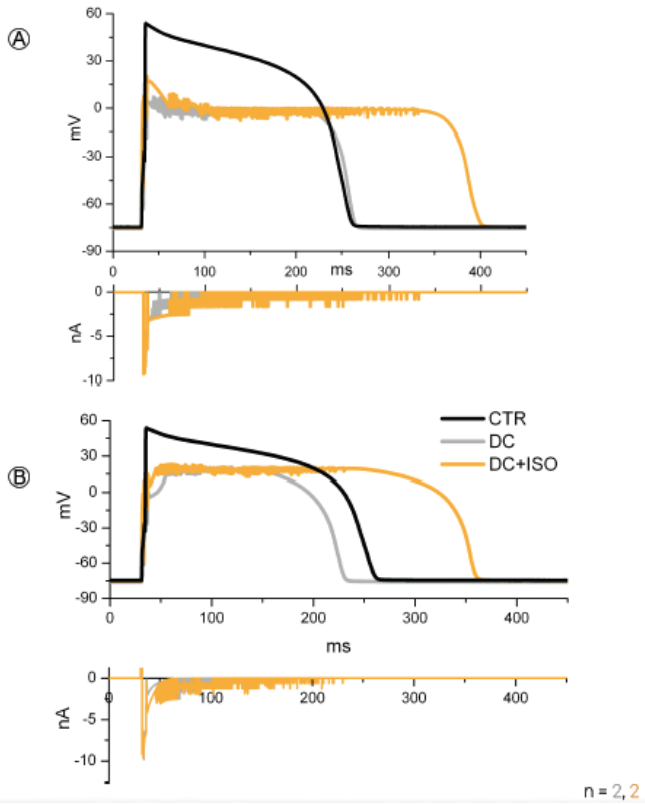

Figure 6.5. Impact of plateau voltage on modulation of APD by ISO

A and **B**: Preliminary results showing the effect of a low plateau level in DC conditions. The plateau level was fixed with DC respectively to 0 mV and +20 mV and we tested the effect of ISO superfusion on APD.

Conclusion

Summarizing: 1) action potential contour modulates APD response to ISO; 2) a lower plateau potential and the "notch" anticipate I_{iso} reversal during repolarization and may thus favor APD shortening over prolongation in response to β-adrenergic agonists; 3) as measured in AP-clamp (open loop), I_{iso} is largely inward (even in D myocytes, [1]), as such it is unsuitable to account directly for APD shortening. Therefore, further modulation of currents by the membrane potential response to I_{iso} may be required to account for the APD shortening effect (closed loop). For this reason, AP-clamp sometimes can give informations completely in contrast to IC/DC.

References

[1] Szentandrássy N, Farkas V, Bárándi L, Hegyi B, Ruzsnavszky F, B. H, et al. Role of action potential configuration and the contribution of Ca and K currents to isoprenaline-induced changes in canine ventricular cells. British Journal of Pharmacology 2012;167:599-611.

[2] Rocchetti M, Freli V, Perego V, Altomare C, Mostacciuolo G, Zaza A. Rate dependency of beta-adrenergic modulation of repolarizing currents in the guinea-pig ventricle. The Journal of physiology 2006;574:183–93.

[3] Rocchetti M, Besana A, Gurrola GB, Possani LD, Zaza A. Rate dependency of delayed rectifier currents during the guinea-pig ventricular action potential. The Journal of physiology 2001;534:721-32.

[4] Bébarová M. Advances in patch clamp technique: towards higher quality and quantity. General physiology and biophysics 2012;31:131-40.

[5] Decker KF, Heijman J, Silva JR, Hund TJ, Rudy Y. Properties and ionic mechanisms of action potential adaptation, restitution, and accommodation in canine epicardium. American Journal of Physiology Heart and Circulatory Physiology 2009;296:1017-26.

[6] Virág L, Jost N, Papp R, Koncz I, A. K, Kohajda Z, et al. Analysis of the contribution of I(to) to repolarization in canine ventricular myocardium. British Journal of Pharmacology 2011;164:93-105.

[7] Bányász T, Fülöp L, Magyar J, Szentandrássy N, Varró A, Nánási PP. Endocardial versus epicardial differences in Ltype calcium current in canine ventricular myocytes studied by action potential voltage clamp. Cardiovascular Research 2003;58:66-75.

[8] Linz KW, Meyer R. Profile and kinetics of L-type calcium current during the cardiac ventricular action potential compared in guinea-pigs, rats and rabbits. Pfluegers ArchivEuropean Journal of Physiology 2000;439:588-99.

CHAPTER 7

Use of Dynamic – clamp to analyse the autonomic modulation of the AP

The content of this chapter has been presented as poster to:

Ravagli E, Bucchi A, **Bartolucci C**, Baruscotti M, DiFrancesco D, Severi S

How "funny" is cardiac pacemaking? A quantitative analysis based on dynami clamp recordings

Biophysical Meeting 2014

Abstract

A typical feature of sinoatrial (SA) node pacemaker cells is the presence of an ionic current that activates upon hyperpolarization. The quantitative role of this hyperpolarization-activated current known as the 'funny current', I_f, in the spontaneous pacemaker activity of SA nodal cells remains a matter of intense debate. We aimed to characterize the impact of I_f as implemented in recent conflicting mathematical models of rabbit SA node pacemaker cells by using the Dynamic Clamp technique.

Experiments were performed using the Real-Time eXperiment Interface (RTXI, [1]) which is a real-time biological experimentation system based on Real-Time Linux. The time course of I_f was dynamically reconstructed from the experimentally recorded action potentials of a single isolated rabbit SA nodal pacemaker cell according to the mathematical models of Maltsev and Lakatta [2] and Severi et al. [3]. Two different protocols were implemented: i) selective I_f block by Ivabradine (3μM, [4, 5]) and substitution with the "syntethic" I_f ii) comparison of the effects of a virtual isoprenaline (ISO)-induced shift (7.5 mV) of I_f activation with the real effects of 1μM ISO [5].

In relation to the substitution of the Ivabradine-sensitive current, the model of Severi et al. (SDiF) allowed to restore the control pacemaking rate (Ctrl [Hz]: 2.86 ± 0.22 Vs SDif: 2.72 ± 0.19, N.S.), whereas Maltsev and Lakatta's (ML) induced only a smaller recovery from current-blocking conditions (Control [Hz]: 2.86 ± 0.22 vs ML: 2.37 ± 0.23, $p<0.05$). Preliminary results on the virtual ISO-induced shift produced a rate increase comparable to the real drug effect (+19.9% vs +30.8%, N.S.), suggesting that I_f accounts for most of the ISO-induced rate increase. Dynamic Clamp results are in agreement with the quantitative description of the I_f impact on the modulation of cardiac pacemaking provided by our recent computational sinoatrial model [3].

Introduction

The sinoatrial node (SAN) is the normal pacemaker of the mammalian heart and generates the electrical impulse for the regular, rhythmic contraction of the heart. The intrinsic pacemaker activity, or spontaneous electrical activity, of an SA nodal pacemaker cell is based on the spontaneous diastolic depolarization that depolarizes the cell towards the action potential threshold. During this diastolic depolarization phase, there is a tiny net inward current across the cell membrane of no more than a few picoamps in amplitude. Animal studies, almost exclusively carried out on cells isolated from rabbit heart, have learned that this net inward current is the result of a complex interaction of multiple inward and outward ion currents, including a hyperpolarization-activated current of mixed ionic nature, known as "funny current," I_f. In line with its activation at hyperpolarized membrane potentials [6], thus generating an inward current during diastole, its enhancement by direct binding of cyclic AMP (cAMP) [7], and its principal presence in primary [8] and secondary pacemakers [9, 10], I_f is traditionally also named "pacemaker current." Of note, the pore-forming subunits of the I_f channel are encoded by members of the HCN gene family, with members HCN1-4.

In recent years, I_f has regained interest in several fields. First, I_f has become a target for pharmacological reduction of heart rate, which may be beneficial for heart failure patients. This reduction is achieved through the specific I_f blocker ivabradine (66% current block and 16% pacemaking rate decrease at 3μM [4, 5]), which has become available for clinical use, and represents a new approach in selective heart rate reduction [11]. Second, mutations in the HCN4 gene, encoding the major HCN isoform of the human SA node [12], have been associated with hereditary SA nodal dysfunction in several families [13-17]. Third, HCN channels are used in engineering a biological pacemaker, as summarized in numerous review papers, for example, [18-21]. In all of these fields, an appropriate quantitative model of the electrical activity of I_f is a desirable tool.

The cellular basis of the pacemaker activity of the SAN, and specifically the degree of contribution of the different mechanisms involved, is still debated ([22-26]). The contribution of I_f to pacemaking has been recently put into question by the development of mathematical models of SAN action potentials (AP) with quantitatively different If intensity, the Severi 2012 (SDiF, [3]) and Maltsev-Lakatta 2009 (ML, [2, 27]) models.

To investigate both models, we have used the Dynamic Clamp (DC), an electrophysiological investigation technique based on a real-time recalculation of the current to inject into the cell under study [28].

The aims of this study are: 1) the model validation, which of two conflicting mathematical models of rabbit SA node pacemaker cells, with largely different I_f intensities (SDiF, ML), better restore the basal condition when used to calculate the DC-based re-injection of I_f blocked by Ivabradine?; 2) the study of the physiological mechanisms of rate modulation: which amount of isoprenaline-induced pacemaking rate increase can be ascribed to the known ISO-induced I_f activation shift?

Methods

Cell preparation

Single rabbit SAN cells were obtained by an enzymatic and mechanical procedure. Spontaneous activity was recorded by perforated-patch. External (Tyrode) solution (mM): 140 NaCl, 5.4 KCl, 1.8 $CaCl_2$, 1 $MgCl_2$, 5 HEPESNaOH, 10 D-glucose, pH 7.4. Pipette solution (mM): 130 K-Aspartate, 10 NaCl, 2 $CaCl_2$, (pCa=7), 2 $MgCl_2$, 10 HEPES, 5 EGTA, 2 ATP(Na-salt), 0.1 GTP, 5 Creatine Phosphate, pH 7.2. Both solutions were prepared as in [5]. Amphotericin B (100–250 μg/ml) was added to the pipette solution. T = 37 ± 0.5 °C.

Experimental Setup

The experimental setup used in this work consists in a combination of classic electrophysiology instrumentation and additional hardware and software for the implementation and use of the necessary dynamic clamp protocols.

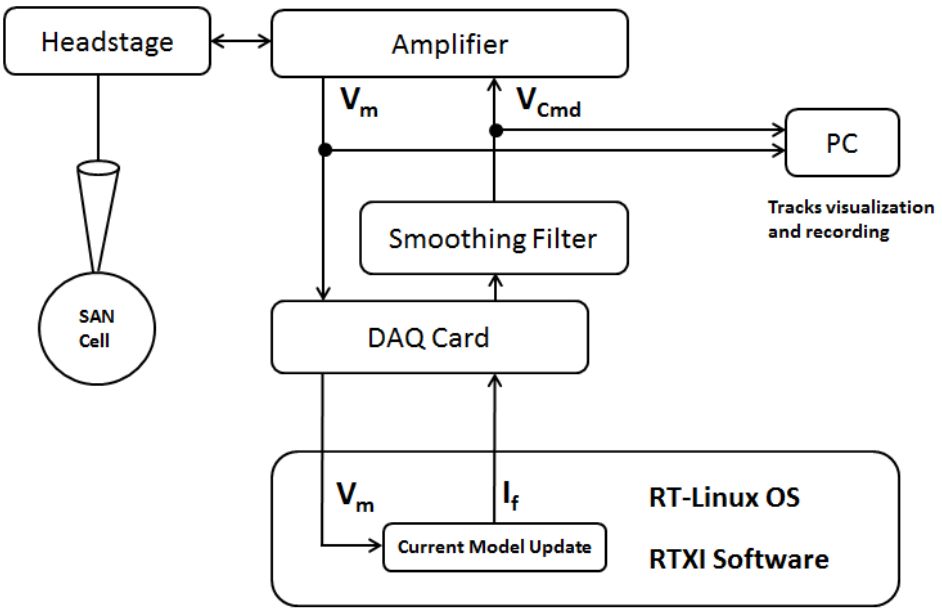

Figure 7.1. Dynamic clamp protocols

An Axopatch 200B Amplifier (Axon Instruments) was set in current clamp mode, to inject a stimulus current and record cellular activity in the form of membrane potentials. The External Command connector was used to pilot the stimulus current shape and intensity in real-time.

Both signals (V_m, V_{Cmd}) were acquired by a PC running PCLAMP software (Molecular Devices), for the visualization and recording of current and potential tracks. Action potentials (APs) were recorded at a sampling rate of 2 kHz and processed with custom software for rate evaluation.

Axon's V_m and V_{Cmd} channels were also connected to a data acquisition board (DAQ, National Instruments), outfitted with 16-bit resolution analog I/O channels. The board was integrated in a second PC with the RT-Linux Operative System installed. The RTXI (Real-Time eXperiment Interface, [1]) software platform was used to implement and run the dynamic clamp protocols described in the following paragraphs. Before each test, membrane capacitance is measured to allow for the injection of the correct current density.

As a general description, valid for each protocol, the custom RTXI code acquires the membrane potential from the DAQ board input channel, updates the model value for the stimulus current and return a voltage signal to pilot the Axon's External Command. The system's update frequency was set to 1 KHz, meaning that every 1 millisecond the current value is updated, several orders of magnitudes faster than the simulated process. Model

updating includes numerical integration of simple differential equations (gating variables formulation). The forward-Eulero method was used, and 100 integration steps are performed for each sampling step.

An additional scaling factor, $g_{Scaling}$ was defined for the output current: as each cell presents an I_f current density which deviates from the average value due to biological heterogeneity, it is necessary to tune the current model to avoid injection of extremely high or low current. The $g_{Scaling}$ parameter is computed with a custom RTXI module that acquires control APs at the beginning of each test and returns the estimated scaling factor, used for the rest of the experiment. The estimation is based on the SDiF SAN cell model [3]: changing the maximum I_f conductance g_F by a scaling factor, it is possible (for a reasonable frequency range) to map the connection between $g_{Scaling}$ and Cycle Length:

$$g_{Scaling} = K_1 + K_2 \cdot e^{-\frac{Cycle\ Lengh}{\tau}}$$

Protocols

Two different test protocols were implemented using custom RTXI modules. Each one is based on the real-time acquisition of the cell's membrane potential, the recalculation of an injection current, and a fast closed-loop response. This feedback mechanism was used in conjunction with Ivabradine (IVA protocol) and isoprenaline (ISO protocol) drugs.

1. IVA protocol

This protocol was defined to investigate the I_f current intensity as described by two different models, the Severi-DiFrancesco model (SDiF) and the Maltsev-Lakatta model (ML), and its effect on basal pacemaking rate. The protocol (Figure 7.2) starts with the acquisition of control AP recordings to evaluate basal pacemaking rate, then 3 µM Ivabradine is applied. At this concentration, the drug only interacts with the cell by blocking the majority of I_f channels (66% [5], slowing pacemaking down [4, 5]. The following step is the activation (by the Dynamic Clamp SW interface) of the synthetic current injection, whose value is computed real-time using one of the two models. The current value is scaled to reproduce the non-total channel block caused by Ivabradine. APs recording continue in this new condition for a time sufficient to detect any pacemaking rate change and then current injection is disabled. Consequently, control APs are recorded again to check for any change from the slowing down condition (due to Ivabradine application), and then current injection with the second model is carried out.

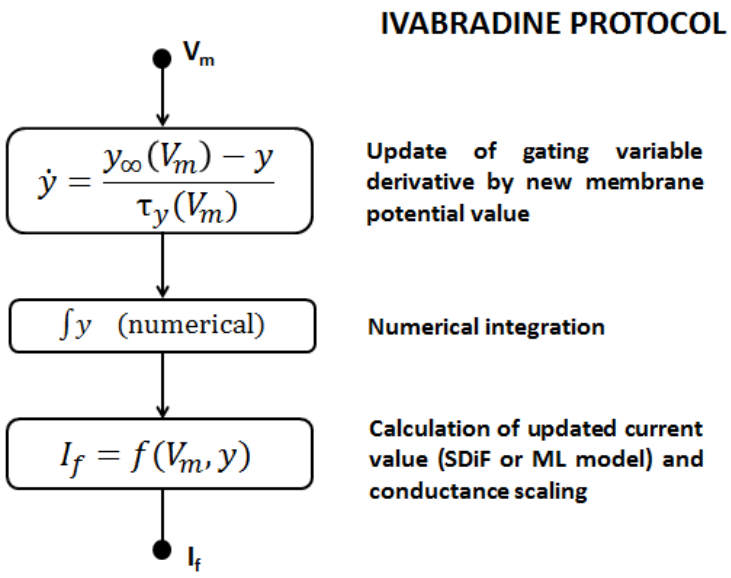

Figure 7.2. Ivabradine protocol diagram

Injection of an artificial model-based I_f to substitute for the current blocked by Ivabradine.

2. ISO protocol

This protocol was built to study the accuracy of an I_f model in describing pacemaking changes due to autonomic modulation drugs. Differently from the previous protocol, synthetic current effect and drug effect are evaluated separately, with no direct superposition in time.

As the experiment with Ivabradine showed a quantitative difference between the SDiF and ML model in terms of current intensity needed to restore control pacemaking rate, the SDif I_f model was chosen for the experiments involving isoprenaline.

As for the IVA protocol, a control AP track is acquired. Then, SDiF synthetic current is injected and APs are recorded to search for pacemaking rate changes. The influence of isoprenaline on I_f is described mathematically as a potential shift in gating variable kinetics, specifically on the steady-state and time constant curves. The influence of isoprenaline is modeled as a +7.5 mV shift [29]. Our custom SW modules update in real-time the current equation and gating kinetics of both a control and shifted I_f current. The first is then subtracted from the second, leading to the injection of a differential DELTA I_f value. Assuming the calculated control current value is roughly comparable to the real I_f in intensity and shape, the injection leaves as the only effective current the shifted I_f, simulating the drug's effect (Figure 7.3).

$$\Delta I_f = I_{f,Shifted} - I_{f,Control}$$

$$I_{f,real} + \Delta I_f = I_{f,real} + I_{f,Shifted} - I_{f,Control} \approx I_{f,Shifted}$$

After AP track recording, current injection is disabled, control APs are acquired again, and then real drug is applied to compare its effect on pacemaking rate with our simulated drug application.

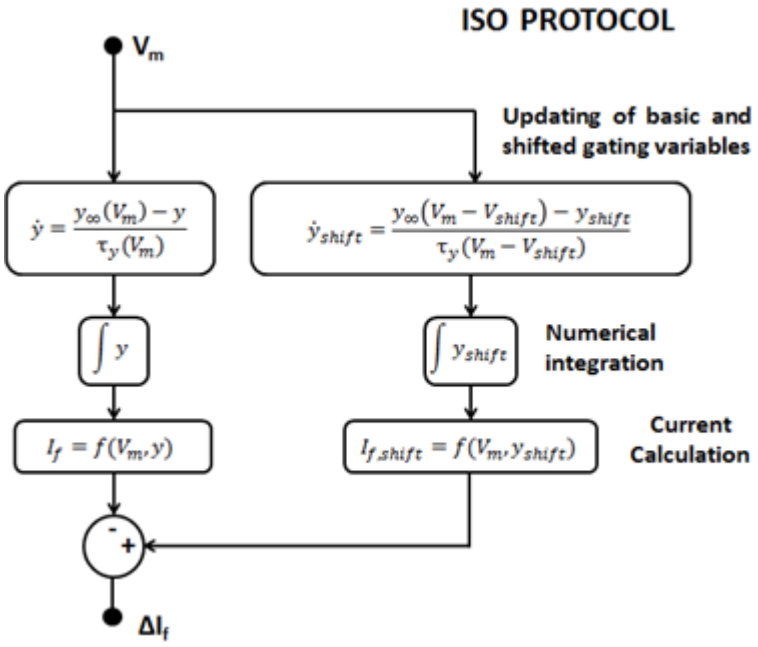

Figure 7.3. Isoprenaline protocol diagram

Injection of a differential model-based current to simulate application of isoprenaline.

Data processing and statistical analysis

AP recordings were undersampled from 2 KHz to 500 Hz and exported in ASCII format on custom software for the evaluation of pacemaking rate evolution in time.

After the extraction of a rate value for each protocol state (Control, drug, current injection, etc.), control rate was used as an input for the conductance scaling algorithm, to check for relevant differences from the real-time estimated value.

Current injection recordings were subject to N-Points smoothing to remove residual noise effects.

For each protocol, rate groups were subject to ANOVA test for repeated measures (F-Test Alpha = 0.05, Assumption Alpha = 0.1). After checking for ANOVA significance, rates were subject to Tukey-Kramer test for multiple comparisons, with p = 0.05.

Results

The ability of the injected current modelled with both SDiF and ML mathematical formulation to restore AP changes induced by I_f blockade (Iva, 3 µM) was tested by Dynamic-clamp. The AP was recorded, within each myocyte, in control conditions, during I_f blockade and during its replacement by modelled current; measurements were taken after the AP had achieved a steady-state configuration under each condition. Illustrative examples of the results obtained with the ivabradine protocol are shown in Figure 7.3 A-B (superimposed AP traces and model-based currents injection, respectively).

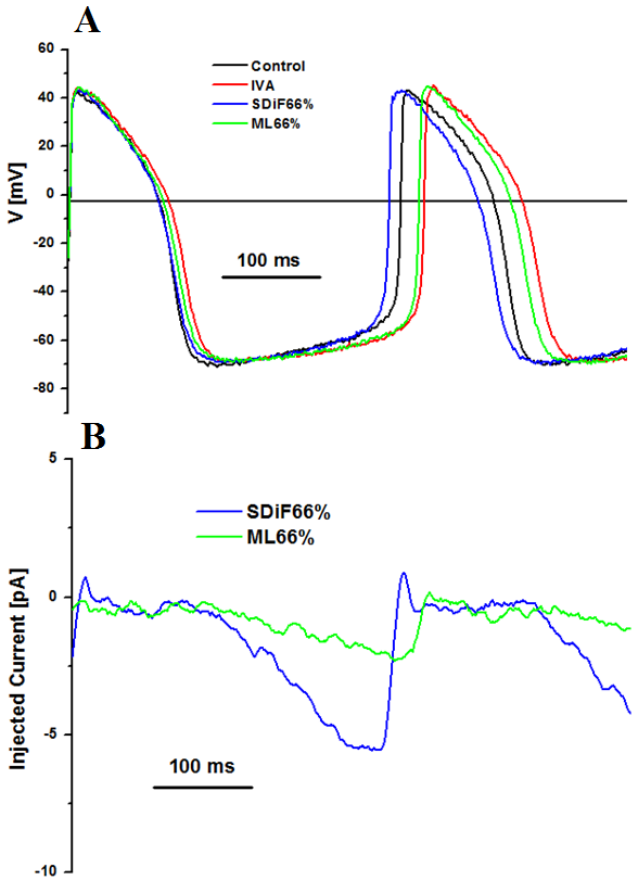

Figure 7.3. A. Example of superimposed AP traces recorded during the different stages of the IVA protocol. **B.** Example of model-based currents injected through Dynamic-Clamp.

The control pacemaking rate (2.86 ± 0.22 Hz) is significantly reduced after application of 3µM Ivabradine (2.27 ± 0.26 Hz, $p<0.05$). The rate decrease (-20.6%) is comparable with values reported in literature (-23.8 ± 3.9% [30], -16.2 ± 1.5% [5]).

As already described in the Methods Section, the conductance scaling values for these tests (66%) were chosen in accordance with reported percentages of channel blockage by ivabradine (65.9 ± 2.4%, [5]). The injection of the SDiF66 synthetic current increases the average pacemaking rate from the ivabradine level, restoring control value (2.72 ± 0.19, N.S. vs Control), while the injection of ML66 synthetic current doesn't show significant alterations (2.37 ± 0.23, N.S. vs ivabradine). This result is displayed on Figure 7.4.

To check for the effectiveness of our investigation regarding the ML model, an additional test with 100% scaling value was carried out (ML100, n = 7), equivalent to the injection of the total calculated synthetic I_f current, which adds to the unblocked remaining current. The increase in current intensity in ML100 leads to a rate value significantly different from the ivabradine level (2.37±0.20, $p<0.05$) but not high enough to reach control value.

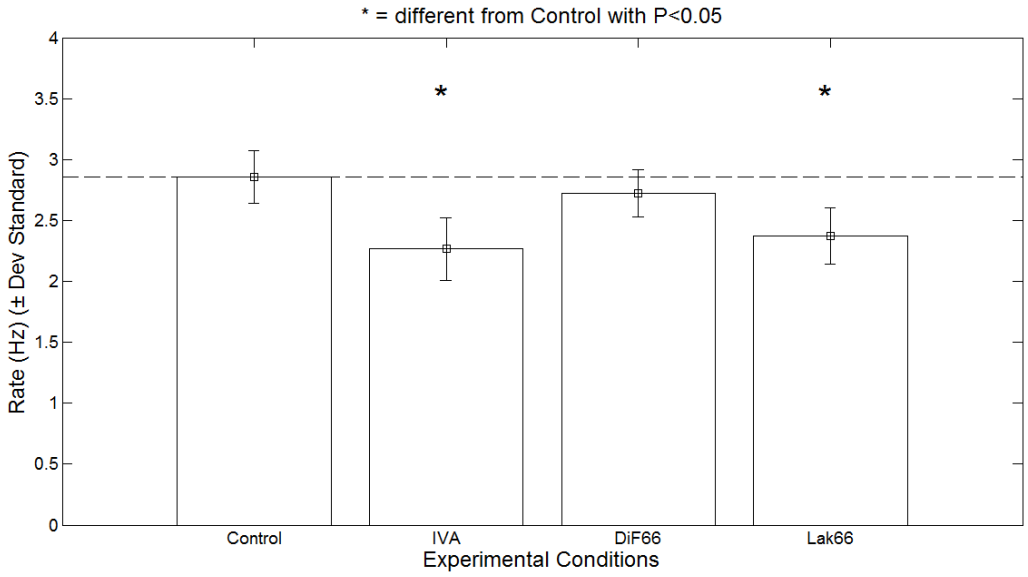

Figure 7.4. Injection of I_f calculated using the SDiF model restores control rate (Ctrl [Hz]: 2.86 ± 0.22 vs SDiF: 2.72 ± 0.19, NS). When the ML model I_f is injected, rate recovery is significantly smaller (ML: 2.37± 0.23, $p<0.05$). n = 8.

An example of the isoprenaline protocol, as described in Methods, is shown in Figure 7.6 A-B (superimposed AP traces and model-based currents injection, respectively).

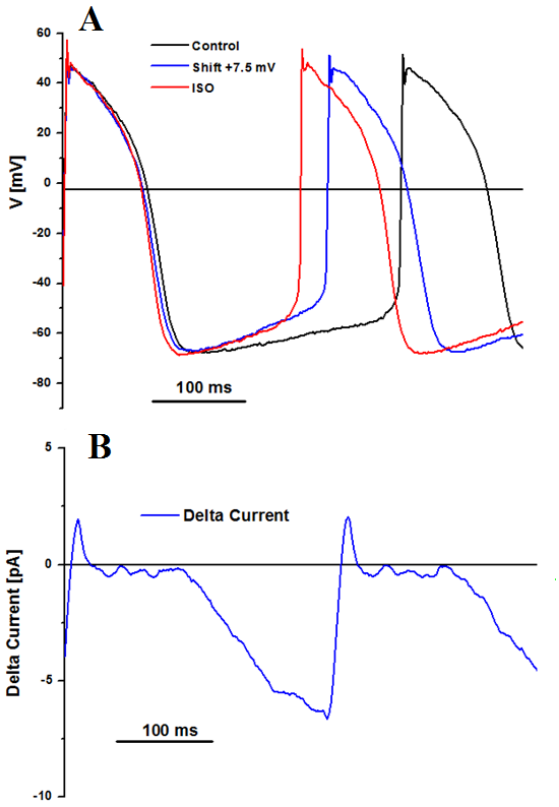

Figure 7.6. A. Example of superimposed AP traces recorded during the different stages of the ISO protocol. **B.** Example of model-based currents injected through Dynamic-Clamp.

Starting from a Control value of 2.81 ± 0.37, the injection of the synthetic ISO shift simulated with the SDiF current model leads to a significant increase in pacemaking rate (3.37 ± 0.50, $p<0.05$). Applying real isoprenaline also induces an increase of pacemaking rate (3.67 ± 0.27, $p<0.05$). There is no significant difference between the pacemaking rate reached by the use of our synthetic current and the real drug ($p<0.05$), Figure 7.7.

The 19.9% rate increase caused by current injection and the 30.8% increase caused by isoprenaline are both comparable to the reported literature values (26.3 ± 5.4%, [5]) for isoprenaline.

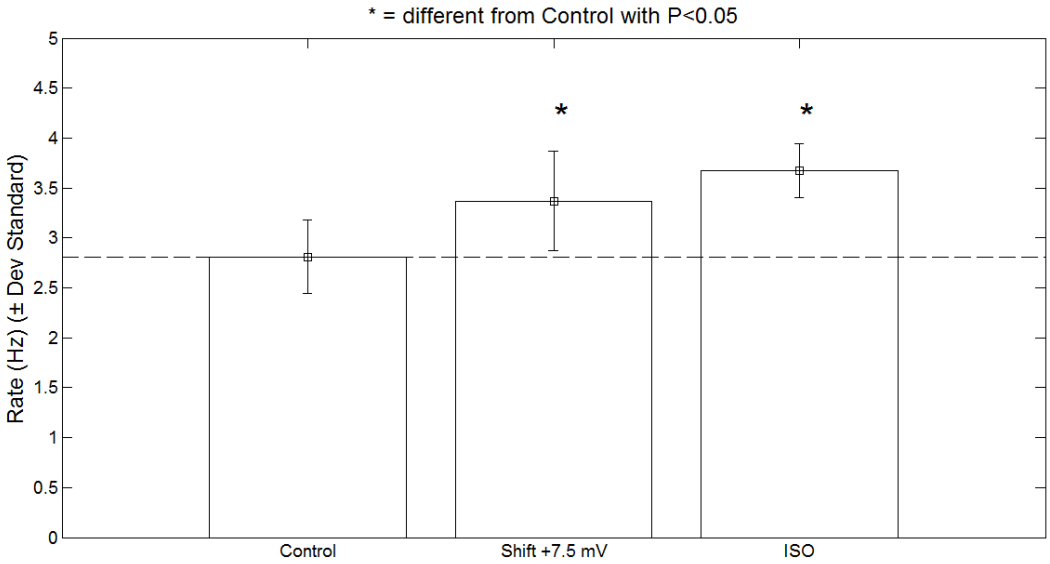

Figure 7.7. The rate increase due to virtual ISO-induced shift its comparable to the real drug effect (Shift [Hz]: 2.88 ± 0.15 vs. ISO [Hz]: 3.09 ± 0.18, NS). n = 5.

Discussion

This work has two aims: the Dynamic clamp was used to prove which model formulation is closer to the real current and for investigate the I_f weight on the pacemaking modulation of the SAN cells. In particular we were interested in a comparison between two I_f mathematical formulations, the Severi [3] and the Maltsev-Lakatta model [2] in order to validate which is the best. Respect to other studies ([31, 32]), this is the first application of the advanced experimental approach, Dynamic clamp, to the I_f current.

The first protocol was used to validate the models: in particular the I_f current was blocked with the ivabradine and replaced with the two formulations. Analyzing the rate, the results supports the idea that the SDiF formulation is closer to the real current contribution in the myocyte (Ctrl [Hz]: 2.86 ± 0.22 vs SDif: 2.72 ± 0.19, N.S.); instead, the ML model was quantitatively insufficient as it wasn't able to restore the rate frequency (ML: 2.37 ± 0.23, $p<0.05$), (see Figure 7.5). In a previous work [3], in order to validate the computational model, the specific pharmacological agent used in experiments and its dose–response characteristic has been considered. This observation, which is obviously valid for any current or mechanism under study, indicates that the weight of I_f has been significantly underestimated in previous models, since the expected amount of I_f block from available experimental data is only partial. The results, reported in [3], demonstrate that it is possible to

reproduce realistic I_f rate modulation properties without dramatically change other model components. The lack of sensitivity to I_f block in previous models can therefore be a consequence of incorrect estimation of membrane currents during diastolic depolarization, but not only of the I_f current [33]. For example, the sensitivity to I_f block may be 'masked' in previous models by the overestimation of other inward currents such as the sodium background current or the sustained sodium current.

Isoprenaline could influence different cellular mechanisms, not only the funny current and it is difficult to dissect experimentally the effects on each one. Its effect was simulated in the SDiF model by shifting the I_f activation curve and modifying other components in accordance with available experimental data. Computational separation of the effects allowed to point out that I_f is the dominant mechanism for ISO-induced rate increase in the range up to 30% and the second protocol goes in this direction: studying the physiological mechanisms of rate modulation, trying to understand which amount of isoprenaline-induced pacemaking rate increase can be ascribed to the known ISO-induced I_f activation shift. We have decided to test only the Severi model, because from the ivabradine experiments it is closer to the I_f native current. Also for this analysis, we used the Dynamic clamp, but with a different approach: we injected in the myocyte a "synthetic" current which corresponds to the difference between a new modelled current where we simulated the isoprenaline effects with a positive shift of the activation (+7.5 mV) and the SDiF I_f in order to cancel the native current (see Methods). A crucial point of this procotol is the assumption that our I_f mathematical model corresponding with the SAN native current. The shift simulated using the Dynamic clamp causes a frequency effect in the same direction of the isoprenaline suggesting that I_f accounts for most of the ISO-induced rate increase.

Conclusions

The SDiF mathematical model of rabbit SA node pacemaker cells, due to the larger I_f intensity, allows to restore the basal condition when used to calculate the DC-based re-injection of I_f blocked by Ivabradine whereas the ML model can only minimally compensate for the I_f block.

The known isoprenaline-induced I_f activation shift accounts for most of the ISO-induced pacemaking rate increase. This result is consistent with the simulation of I_f activation shift in the SDiF sinoatrial AP model [3]

References

[1] http://www.rtxi.org/.

[2] Maltsev VA, Lakatta EG. Synergism of coupled subsarcolemmal Ca2+ clocks and sarcolemmal voltage clocks confers robust and flexible pacemaker function in a novel pacemaker cell model. Am J Physiol Heart Circ Physiol 2009;296:594-615.

[3] Severi S, Fantini M, Charawi LA, DiFrancesco D. An updated computational model of rabbit sinoatrial action potential to investigate the mechanisms of heart rate modulation. J Physiol 2012;590:4483-99.

[4] Bucchi A, Baruscotti M, DiFrancesco D. Current-dependent block of rabbit sino-atrial node I(f) channels by ivabradine. J Gen Physiol 2002 120:1-13.

[5] Bucchi A, Baruscotti M, Robinson RB, DiFrancesco D. Modulation of rate by autonomic agonists in SAN cells involves changes in diastolic depolarization and the pacemaker current. J Mol Cell Cardiol 2007;43:39-48.

[6] Brown H, DiFrancesco D. Voltage-clamp investigations of membrane currents underlying pace-maker activity in rabbit sino-atrial node. Journal of Physiology 1980;308:331-51.

[7] DiFrancesco D, Tortora P. Direct activation of cardiac pacemaker channels by intracellular cyclic AMP. Nature 1991;351:145-7.

[8] Brown HF, DiFrancesco D, Noble SJ. How does adrenaline accelerate the heart? Nature 1979;280:235-6.

[9] DiFrancesco D. Journal of Physiology. A study of the ionic nature of the pace-maker current in calf Purkinje fibres 1981;314:377-93.

[10] Noma A, Irisawa H, Kokobun S. Slow current systems in the A-V node of the rabbit heart. Nature 1980;285:228-9.

[11] Roubille F, Tardif JC. New therapeutic targets in cardiology: heart failure and arrhythmia: HCN channels. Circulation 2013;127:1986-96.

[12] Chandler NJ, Greener ID, Tellez JO, Inada S, Musa H, Molenaar P, et al. Molecular architecture of the human sinus node insights into the function of the cardiac pacemaker. Circulation 2009;119:1562-75.

[13] Duhme N, Schweizer PA, Thomas D, Becker R, Schröter J, Barends TR, et al. Altered HCN4 channel C-linker interaction is associated with familial tachycardia-bradycardia syndrome and atrial fibrillation. Eur Heart J 2013;34:2768-75.

[14] Milanesi R, Baruscotti M, Gnecchi-Ruscone T, DiFrancesco D. Familial sinus bradycardia associated with a mutation in the cardiac pacemaker channel. The New England Journal of Medicine 2006;354:151-7.

[15] Nof E, Luria D, Brass D, Marek D, Lahat H, Reznik-Wolf H, et al. Point mutation in the HCN4 cardiac ion channel pore affecting synthesis, trafficking, and functional expression is associated with familial asymptomatic sinus bradycardia. Circulation 2007;116:463-70.

[16] Schulze-Bahr E, Neu A, Friederich P, Kaupp UB, Breithardt G, Pongs O, et al. Pacemaker channel dysfunction in a patient with sinus node disease. J Clin Invest 2003;111:1537-45.

[17] Ueda K, Nakamura K, Hayashi T, Inagaki N, Takahashi M, Arimura T, et al. Functional characterization of a trafficking-defective HCN4 mutation, D553N, associated with cardiac arrhythmia. J Biol Chem 2004;279:27194-8.

[18] Cho HC, Marban E. Biological therapies for cardiac arrhythmias: can genes and cells replace drugs and devices? Circulation Research 2010;106:674-85.

[19] Li R. Gene- and cell-based bio-artificial pacemaker:what basic and translational lessons have we learned? Gene Therapy 2012;19:588-95.

[20] Robinson RB, Brink PR, Cohen IS, Rosen MR. If and the biological pacemaker. Pharmacological Research 2006;53:407-15.

[21] Rosen MR, Robinson RB, Brink PR, Cohen IS. The road to biological pacing. Nature Reviews Cardiology 2011;8:656-66.

[22] DiFrancesco D. The role of the funny current in pacemaker activity. Circ Res 2010;106:434-46.

[23] Lakatta EG, DiFrancesco D. What keeps us ticking: a funny current, a calcium clock, or both? J Mol Cell Cardiol 2009;47:157-70.

[24] Maltsev VA, Lakatta EG. The funny current in the context of the coupled-clock pacemaker cell system. Heart Rhythm 2012;9:302-7.

[25] Rosen MR, Nargeot J, Salama G. The case for the funny current and the calcium clock. Heart Rhythm 2012;9:616-8.

[26] Verkerk AO, Wilders R. Relative importance of funny current in human versus rabbit sinoatrial node. J Mol Cell Cardiol 2010;48:799-801.

[27] Yaniv Y, Stern MD, Lakatta EG, Maltsev VA. Mechanisms of beat-to-beat regulation of cardiac pacemaker cell function by Ca^{2+} cycling dynamics. Biophys J 2013;105:1551-61.

[28] Wilders R. Dynamic clamp: a powerful tool in cardiac electrophysiology. J Physiol 2006;576:349-59.

[29] Zaza A, Rocchetti M, DiFrancesco D. Modulation of the hyperpolarization-activated current (I(f)) by adenosine in rabbit sinoatrial myocytes. Circulation 1996;94:734-41.

[30] Thollon C, Cambarrat C, Vian J, Prost JF, Peglion JL, Vilaine JP. Electrophysiological effects of S 16257, a novel sino-atrial node modulator, on rabbit and guinea-pig cardiac preparations: comparison with UL-FS 49. Br J Pharmacol 1994;112:37-42.

[31] Klöckner U, Rueckschloss U, Grossmann C, Ebelt H, Müller-Werdan U, Loppnow H, et al. Differential reduction of HCN channel activity by various types of lipopolysaccharide. J Mol Cell Cardiol 2011;51:226-35.

[32] Verkerk AO, Wilders R, Coronel R, Ravesloot JH, Verheijck EE. Ionic remodeling of sinoatrial node cells by heart failure. Circulation 2003;108:760-6.

[33] van Ginneken AC, Giles W. Voltage clamp measurements of the hyperpolarization-activated inward current If in single cells from rabbit sino-atrial node. J Physiol 1991;434:57-83.

CONCLUSION

My research activity has been focusing on the mathematical modeling and numerical simulation, applied to the cardiac electrophysiology analysis at a single cell level and on the Dynamic clamp technique application with the aim of gaining a clearer insight into the origin of the dynamics of electrophysiological models.

The second chapter has concerned the simulation of a novel mutation (responsible for short QT syndrome) using two human AP models, the ten Tusscher -Panfilov and the O'Hara Rudy. The simulation results predicted a similar shortening of the AP than observed in the patient, and were useful to strengthen the experimental results.

All the other works used DC in different applications. The first application was aimed to: 1) optimize the Luo-Rudy mathematical formulation of the guinea-pig rapid delayed rectifier K^+ current (I_{Kr}) and 2) validate the new model, analyzing the effects of the current block (using the specific blocker E4031) and of the modelled current injection on the AP duration. We were able to provide an optimized I_{Kr} model able to reproduce AP- and Dynamic- clamp experimental data. A positive message conveyed by the results is that, once a reliable numerical I_{Kr} model is developed, it can be expected to accurately reproduce the native I_{Kr} behaviour in the context of myocyte complexity. This is particularly relevant in consideration of the peculiar role of I_{Kr} in repolarization and of the high cost of biological tests currently used to assess the drug arrhythmogenic potential due to I_{Kr} alterations. The optimized model has been integrated into action potential models to explore the effects of changes in individual kinetic parameters on cardiac repolarization.

The second study invastigated the I_{Kr} impact on repolarization and its variability using the optimized model (obtained as described in chapter 3). Identification of the relative impact of I_{Kr} gating properties may provide a new framework for predicting the consequences of I_{Kr} mutations on APD and its variability, two quantities strongly associated with arrhythmogenic

risk. If validated by correlation with clinical observations, such a framework would be of obvious practical use.

The third study regarded the comparison between different species (dog and guinea-pig) for what concerns the transient outward K^+ current (I_{to}) presence. We investigated whether a spike – and – dome profile (SaD) is the main factor determing the direction of APD response to β – adrenergic stimulation. The possibility to inject in a guinea pig a "synthetic" I_{to} current (which is absent) has allowed to examine 1) the ISO effects on APD (in guinea-pig and canine myocyte); 2) the presence of AP spike – and – dome profile.

The last DC application regards the "funny" current I_f present in the sinoatrial node pacemaker cells. This work has shown that the I_f formulation by Severi et al. 2012 allows to restore the basal condition when used to calculate the DC-based re-injection of I_f blocked by Ivabradine whereas the Maltsev-Lakatta 2009 model can only minimally compensate for the I_f block. In addition the study of the physiological mechanisms of rate modulation has revealed that the known isoprenaline-induced I_f activation shift accounts for most of the ISO-induced pacemaking rate increase.

In conclusion, our results can assert that dynamic clamp is a promising approach as it allows to test how the properties of a numerical model affect the AP generated by a real myocyte and they show how mathematical approach is suitable to provide new insights into the cardiac AP mechanisms in physiological and pathological conditions.

LIST OF PUBLICATIONS

Journal Articles

Bartolucci C, Altomare C, Bennati M, Furini S, Zaza A*****, Severi S***.** Combined Action Potential- and Dynamic-Clamp for accurate computational modelling of the cardiac I_{Kr} current. *Journal of molecular and cellular cardiology, vol. 79C, pp. 187–194, Nov. 2014*

Altomare C, **Bartolucci C**, Sala L, Rocchetti M, Mostacciuolo G, Severi S*, Zaza A*. IKr impact on repolarization and its variability assessed by Dynamic-Clamp. Submitted to *Circulation: Arrhythmia and Electrophysiology*.

Moreno C, Oliveras A, Muñoz C, de la Cruz A, **Bartolucci C**, Salar E, Gimeno-Blanes JR, Severi S, Felipe A, Lambiase P, Valenzuela C. New KCNQ1 mutation responsible of short QT syndrome located at the S5 segment. Submitted to *Cardiovascular Research*.

Conference proceedings

Sala L, Hegyi B, **Bartolucci C**, Altomare C, Rocchetti M, Mostacciuolo G, Severi S, Szentandrassy N, Nanasi P.P., Zaza A. Effects of species-dependent differences in action potential shape in setting β-adrenergic-stimulation induced current. EHRA EUROPACE 2013, Athens (Greece), 22-23 July 2013.

Altomare C, Sala L, **Bartolucci C**, Mostacciuolo G, Severi S*, Zaza A*. IKr impact on repolarization and its variability assessed by Dynamic-Clamp. ESCANDE Symposium 2013, Amsterdam, 30 August 2013.

Bartolucci C, Altomare C, Bennati M, Furini S, Zaza A, Severi S**.** Combined Action Potential- and Dynamic-Clamp for Accurate Computational Modeling of the Kinetics of Cardiac IKr Current. Compunting in Cardiology 2013, Zaragoza (Spain), 25 September 2013.

Altomare C, Sala L, **Bartolucci C**, Mostacciuolo G, Severi S, Zaza A. IKr impact on repolarization and its variability assessed by Dynamic-Clamp. Computing in Cardiology 2013, Zaragoza (Spain), 25 September 2013.

Sala L, Hegyi B, **Bartolucci C**, Altomare C, Rocchetti M, Mostacciuolo G, Severi S, Szentandrassy N, Nanasi PP, Zaza A. Effects of species-dependent differences in action potential shape in setting β-adrenergic-stimulation induced current. Computing in Cardiology 2013, Zaragoza (Spain), 24 September 2013.

Sala L, Hegyi B, **Bartolucci C**, Altomare C, Rocchetti M, Mostacciuolo G, Severi S, Szentandrassy N, Nanasi P.P., Zaza A. Effects of species-dependent differences in action potential shape in setting β-adrenergic-stimulation induced current. 58th Annual Meeting of the Biophysical Society, San Francisco (CA) USA, 15-19 February 2014.

Altomare C, Sala L, **Bartolucci C**, Mostacciuolo G, Severi S, Zaza A. IKr impact on repolarization and its variability assessed by Dynamic-Clamp. 58th Annual Meeting of the Biophysical Society, San Francisco (CA) USA, 15-19 February 2014.

Ravagli E, Bucchi A, **Bartolucci C**, Baruscotti M, DiFrancesco D, Severi S. How “funny” is the cardiac pacemaking? A quantitative analysis based on Dynamic Clamp recordings. 58th Annual Meeting of the Biophysical Society, San Francisco (CA) USA, 15-19 February 2014.

Bartolucci C, Moreno C, de la Cruz A, Lambiase P, Severi S, Valenzuela C. Linking a Novel Mutation to its Short QT Phenotype through Multiscale Computational Modelling. Computing in Cardiology 2014, Boston (USA), 10 September 2014.

APPENDIX A

Supplemental materials: Computational analysis of ventricular repolarization: classical approach investigating Short QT Syndrome

---

The content of this chapter has been submitted to:

Moreno C, Oliveras A, Muñoz C, de la Cruz A, **Bartolucci C**, Salar E, Gimeno-Blanes JR, Severi S, Felipe A, Lambiase P, Valenzuela C

New KCNQ1 mutation responsible of short QT syndrome located at the S5 segment

Expanded Methods

The institutional review board at The Heart Hospital, Institute of Cardiovascular Science (London) approved the study, and the patient provided written informed consent. The study conforms with the Declarations of Helsinki.

Expression plasmids and site-directed mutagenesis

Human K_v7.1 cDNA in pTLN vector was provided by T. Jentsch (Leibniz-Institut für Molekulare Pharmakologie and Max-Delbrück-Centrum für Molekulare Medizin, Berlin, Germany). Human KCNE1 cDNA in pHA vector was obteined from S. de la Luna (Centro de Regulación Genómica-CRG, Barcelona, Spain). For confocal microscopy and molecular biology studies both plasmids were cloned in to pEYFP-C1 and pECFP-N1 (Clontech), respectively. Point mutation in wild-type K_v7.1 cDNA was introduced by PCR using QuickChange II XL Site-Directed Mutagenesi Kit (Agilent Technologies). The fenilalanine at the aminoacidic position 279 was replaced by an isoleucine to obtain K_v7.1F279I mutant following the protocol recommended by the manufacturer and using the primers described below. All, wild-type and mutant constructs were verified by DNA sequencing.

Primer sequences for site-directed mutagenesis of Kv7.1F279I*:

Forward 5' CCTCATCTTCTCCTCGTAC**A**TTGTGTACCTGGCTGAG '3

Reverse 5' CCTTCTCAGCCAGGTACACAA**T**GTACGAGGAGAAGATG '3

*modified sequence is shown in bold letters

Cell Culture and Transfection

The African green monkey kidney-derived cell line COS7 was obtained from the American Type Culture Collection (Rockville, MD) and cultured at 37ºC in Dulbecco's modified Eagle's medium supplemented with 10% fetal bovine serum (FBS) and antibiotics (100 IU/ml penicillin and 100 μg/ml streptomycin; all from Gibco, Paisley, UK) in a 5% CO_2 atmosphere. COS7 cells were transiently transfected with Fugene6 (Promega) at 60% confluence.

HEK293 cells were grown in Dulbecco's Modified Eagle's Medium (DMEM) supplemented with 10% (v/v) of FBS and 100U/ml of penicillin/streptomycin (all from Gibco, Paisley, UK). For molecular biology experiments cells were plated in 100-mm culture dishes and for confocal microscopy studies on poly-D-lysine coated coverslips. In these experiments,

transient transfection was performed using Metafecte^{TM}Pro (Biontex) at nearly 80% confluence.

HL-1 cells were grown in Claycomb Medium (Sigma-Aldrich) supplemented with 1% (v/v) L-Glutamine (Gibco), 0.1mM of norepinephrine (Sigma-Aldrich), 10% (v/v) of FBS and 100U/ml of penicillin/streptomycin (all from Gibco, Paisley, UK). Cells were cultured in 60mm pretreated dishes with 0.02% of gelatin solution (Sigma-Aldrich) supplemented with 1mg/ml of fibronectin and bovine plasma (Calbiochem), in a 5% CO_2 atmosphere at 37ºC. Cells were transiently transfected with Fugene6 (Promega) at 80% confluence. HL-1 cells were kindly provided by Dr. Lisardo Boscá (Instituto de Investigaciones Biomédicas CSIC-UAM, Madrid, Spain).

Co-immunoprecipitation, biotinylation of surface proteins and western blotting

Twenty-four hours after transfection cells were washed twice with ice-cold PBS. For co-immunoprecipitation experiments cells were lysed in 1% Triton X-100, 10% glycerol, 5 mM HEPES pH 7.2 and 150 mM NaCl supplemented with 1 μg/ml aprotinin, 1 μg/ml leupeptin, 1 μg/ml pepstatin and 1 mM phenylmethylsulfonyl fluoride as protease inhibitors. Homogenates were centrifuge at 12,000 *g* for 15 min and total protein content of supernatant was determined using Bio-Rad Protein Assay (Bio-Rad). To prepare protein A-Sepharose beads (GE Healthcare) for immunoprecipitation experiments they were incubated with anti-KCNE1 antibody (Alomone Labs) for 1 hour at room temperature on a gently mixing. Once bead-antibody complexes were formed, antibody was covalently bound to protein Using Dimethyl Pimelimidate (DMP) (Pierce) as a cross-linker by incubation with 20 mM DMP for 30 min at room temperature on a gently mixing. Cross-linking reaction was quenched adding Glycine 0.2 M pH 2.5. Cell lysates were pre-cleared with protein A-Sepharose beads for 1 hour at 4ºC on a gently mixing. Beads were removed by centrifugation at 1,000 *g* for 30 seconds and then sample was incubated overnight with beads coated with anti-KCNE1 antibody at 4ºC. After 5 times wash proteins bound to antibody-beads complexes were eluted in 100 μl of Glycine 0.2 M pH 2.5.

Cell surface proteins biotinylation was carried out with Pierce Cell Surface Protein Isolation Kit (Pierce) following manufacturer's instructions. EZ-Link Sulfo-NHS-SS-Biotin (sulfosuccinimidyl-2-[biotinamido]ethyl-1,3-dithiopropionate) is a thiol-cleavable amine-reactive biotinylation reagent, N-hydroxysulfosuccinimide (NHS) ester group can react with

primary amines of lysine aminoacidic residues. Kv7.1 have 3 available lysines in position 218 (extracellular loop S3-S4), 285 and 326 (extracellular loop S5-pore-S6) of aminoacid sequence and KCNE1 2 of them, in position 15 and 41 of N-terminal domain.

For western blotting, protein samples were prepared in 1×Laemmli SDS loading buffer, boiled for 5 min and resolved in a 8-10% SDS-PAGE gel. Then, were transferred into Immobilon-P nitrocellulose membrane (Millipore) and blocked in 5% powdered milk PBS 0.05%Tween-20 before immunodetection. Membranes were immunoblotted against Kv7.1 (anti-Kv7.1 1:2500 (Alomone Labs)), KCNE1 (anti-KCNE1 1:2500) and β-actin (1:50000 (Sigma)) diluted in blocking solution. After washing blots were incubated with secondary antibody horseradish peroxidase-conjugated goat anti-rabbit (Bio-Rad) and developed using Chemiluminiescence Detection Kit for HRP (Biological Industries) detected on Kodak Medical X-Ray Films (Kodak).

Confocal microscopy, Plasma membrane lawns and FRET

Twenty-four hours after transfection staining of plasma membrane was performed using wheat germ agglutinin (WGA) linked with fluorescent dye Alexa 555 (Invitrogen) under non-premeabilizing conditions. Cells were washed twice with cold PBS and incubated with WGA-Alexa555 diluted 1:1500 in DMEM HEPES 30mM for 5 min at 4ºC. Subsequently washed again, fixed with 4% paraformaldehyde during 30 min at 4ºC and mounted in ProLong Gold antifade Reagent (Invitrogen) on microscope slides. Images were taken using a Leica SP2 laser scanning confocal spectral microscope (Leica Microsystems) equipped with an argon laser and red light laser. Laser lines 514 (YFP), 458 (CFP) and 561 (Alexa555), 63× oil immersion objective lens (NA 1.32) and double dichroic filter (458/514) were used to acquire images. Pixel by pixel colocalization analysis was performed using Image J software.

Plasma membrane lawns (PML) are membrane sheets obtained by an osmotic shock. HEK293 cells were seeded in poli-D-lysine treated glass coverslips. Forty-eight hours after transfection (Metafectene Pro) cells were cooled on ice for 5 min and washed twice in PBS. Next, incubated during 5 min in KHMgE buffer (70mM KCl, 30mM HEPES, 5mM $MgCl_2$, 3mM EGTA, pH 7.5) diluted three times and then, gently washed with non-diluted KHMgE to induce the hypotonic shock. Busted cells were removed from the coverslip by pipetting up and down. After two washes with KHMgE buffer only membrane sheets remain attached. PML were fixed with fresh 4% paraformaldehyde during 10 min at room temperature and mounted in Mowiol mounting media.

Föster Resonance Energy Transfer (FRET) by acceptor photobleaching technique was performed under a Leica SP 2 confocal microscope (Leica Microsystems GmbH, Germany) using an Argon laser tuned at 458 and 514nm lines. Pictures were taken with an oil immersion objective of 63 × 1.32 NA at zoom 4. According to this procedure, if a FRET phenomenon is taken place, an increase of donor (CFP) fluorescence intensity should be detected after acceptor (YFP) photobleaching. Acceptor photobleaching consisted in three scans of the region of interest (ROI) using 514 nm line of Argon laser at 100% power intensity. Before and after photobleaching CFP and YFP images were collected.

FRET efficiency (E_F) was calculated following the formula $E_F = (D_{post}-D_{pre})/D_{post}$, where D is the CFP fluorescence intensity (D_{pre}) before and (D_{post}) after photobleaching normalized by CFP fluorescence intensity outside the ROI to monitor CFP photobleaching do to imaging.

Electrophysiological Technique and Data Acquisition from COS7 and HL-1 cells

Membrane currents were measured with the amphotericin B-perforated patch configuration of the patch-clamp technique, as previously reported [1-4]. The intracellular pipette filling solution contained (mM): K-aspartate 80, KCl 50, phosphocreatine 3, KH_2 PO_4 10, MgATP 3, HEPES-K 10, EGTA 5 and was adjusted to pH 7.25 with KOH. The bath solution contained (mM): NaCl 130, KCl 4, $CaCl_2$ 1.8, $MgCl_2$ 1, HEPES-Na 10, and glucose 10, and was adjusted to pH 7.40 with NaOH.

Currents were recorded using the perforated-patch configuration of the patch-clamp technique using an Axopatch 200B amplifier (Axon Instruments) [4]. Currents were filtered at 1 kHz (4-pole Bessel filter) and sampled at 2 kHz. Micropipettes were pulled from borosilicate glass capillary tubes (Narishige, GD-1) on a programmable horizontal puller (Sutter Instruments Co.) and heat-polished with a microforge (Narishige). Micropipette resistance was 1-3 MΩ. Capacitance and series resistance compensation were optimized. pClamp version 9 software (Axon Instruments) was used for data acquisition and analysis. Currents were recorded at room temperature (21-23ºC) at a stimulation frequency of 0.03 Hz. Microcal Origin 8.5 (Microcal Software) and Clampfit 9 programs were used to perform least-squares fitting and for data presentation.

Activation and deactivation process were fitted to a mono- or biexponential equation of the form:

$y = A_1 \exp(-t/\tau_1) + A_2 \exp(-t/\tau_2) + C$

where τ_1 and τ_2 are the system time constants, A_1 and A_2 are the amplitudes of each component of the exponential, and C is the baseline value [2, 4]. The voltage dependence of activation curves were fitted with a Boltzmann equation: $y = 1/[1 + \exp(-(V-V_h)/s)]$, in which *s* represents the slope factor, *V* the membrane potential and V_h the voltage at which 50% of the channels are open.

Computational analysis

To evaluate the electrophysiological consequences of the F279I mutation at the level of the cardiac AP, we modified the Ten Tusscher-Panfilov (TTP) human ventricular myocyte model [5]. We used the TTP I_{Ks} formulation to simulate the WT $K_v7.1$ condition, while we changed the activation kinetics in agreement with voltage-clamp recordings of $K_v7.1$ current in the presence of KCNE1 (Tables S1 and S2) to simulate the mutant condition. In particular, concerning the steady state activation we introduced a negative shift of 25mV between WT $K_v7.1$/KCNE1 and F279I $K_v7.1$/KCNE1 and a negative shift of 14mV between WT $K_v7.1$/KCNE1 and WT $K_v7.1$/ F279I $K_v7.1$/KCNE1. We did not modify the slope factor because the model value (14mV) was close to the experimental fitted values (16-17.9mV). In addition, since the patch-clamp experiments were at room temperature we decided not to use the measured time constants to simulate the effect of the mutation, but rather to scale the activation time constant, τ_f, of the original model (fitted on data at physiological temperature) by a factor equal to the ratio between measured F279I $K_v7.1$/KCNE1, WT $K_v7.1$/ F279I $K_v7.1$/KCNE1 and WT $K_v7.1$/KCNE1 values (Table S1).

To test the model-dependency of the simulation results, we carried out the simulation also using the O'Hara-Rudy (ORd) human ventricular myocyte model [6]. Simulations were conducted for isolated endocardial, epicardial, and M cells. All cells were paced over 500 times at the basic cycle length of 1000ms. The APD_{90} was defined as APD at 90% of repolarization. Model equations were implemented in Matlab 11a (The MathWorks Inc.) and numerically solved by using the ode15s solver. We repeated all the simulations, with both models, by introducing the β-adrenergic stimulation by increasing I_{Ks} (maximal conductance scaled by a factor of 2.66), I_{CaL} (maximal conductance scaled by a factor of 1.5) and I_{up} (maximal current scaled by a factor of 1.5) according to a previous computational study [7] .

Pseudo-ECG Simulations

One dimensional fiber (1.64 cm length) composed by 25 endo-, 25 M-, 50 mid- and 65 epicardial cells has been considered. Model equations have been translated into cellML language using COR environment and monodomain equations have been solved with Chaste Software [8]. Pseudo-ECG signal has been computed as described by Glukhov et al. [9]

Statistical Analysis

Data are presented as mean values±SEM. Two way ANOVA repetitive measurements test followed by Bonferroni test were used to assess statistical significance where appropriate. The curve-fitting procedure used a non-linear least-squares (Gauss-Newton) algorithm; results were displayed in linear and semilogarithmic format, together with the difference plot. Goodness of fit was judged by the χ^2 criterion and by inspection for systematic non-random trends in the difference plot. A value of $P<0.05$ was considered significant.

Additional Figures

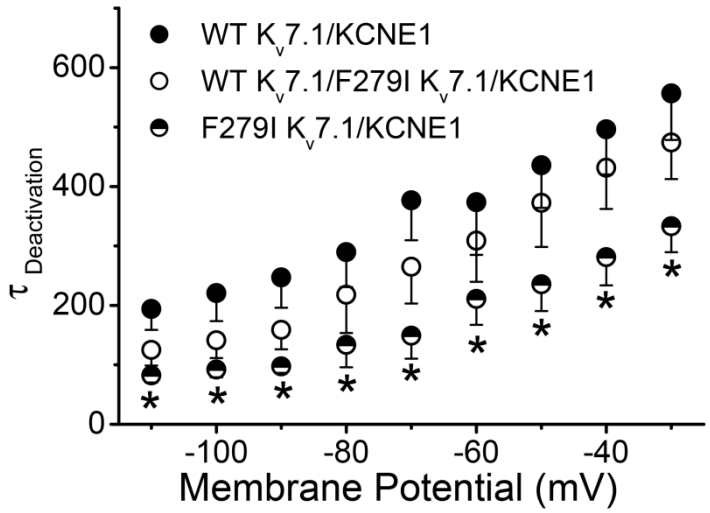

Figure S1. Comparison of deactivation time constants for the WT K_v7.1 channels expressed with the accessory subunit KCNE1 and for F279I K_v7.1/KCNE1 and WT/F279IK_v7.1/KCNE1 channel complexes

Deactivation time constants were obtained by fitting the tail currents to monoexponential decay functions and were plotted as a function of the repolarization potential. (*P<0.05, n=4-11, for WT/F279IK_v7.1/KCNE1 *vs*. control conditions).

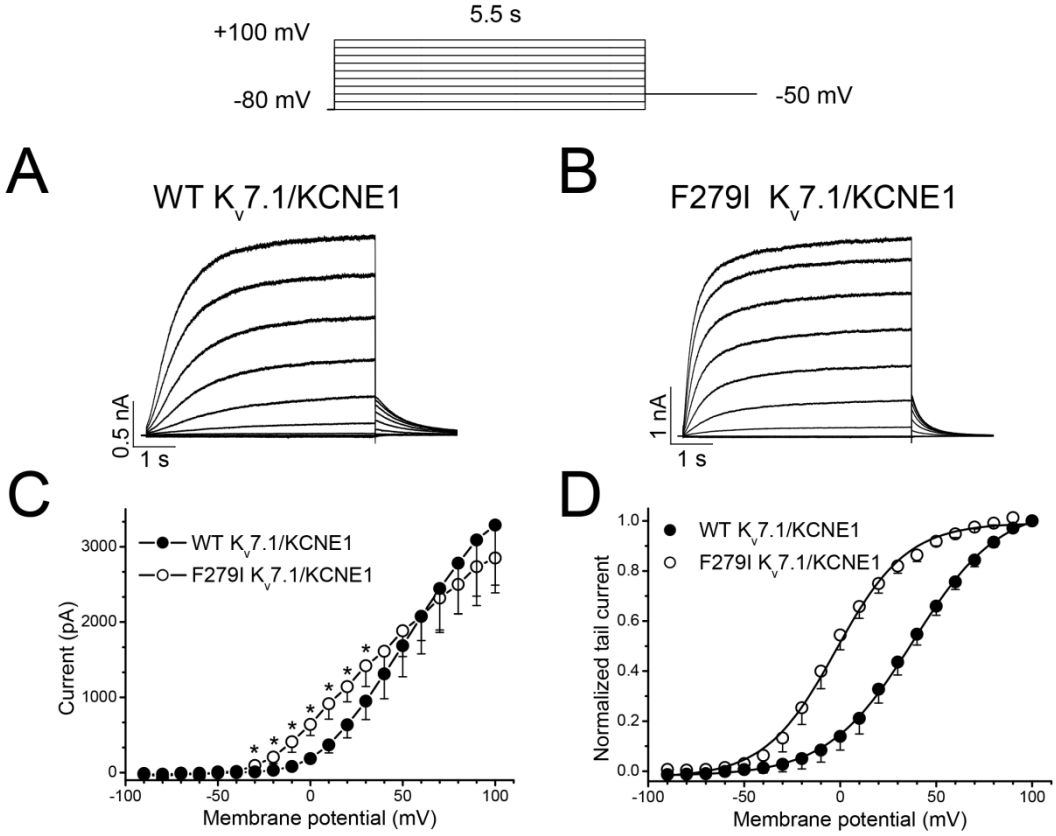

Figure S2. Currents induced by co-expression of KCNE1 with WT or F279I K_v7.1 channels in HL-1 cells.

(A-B) WT and F279I K_v7.1/KCNE1 currents records. For panels A-B, pulses were applied from a holding potential of -80mV to +100mV in 20mV-steps. Tail currents were recorded at -50mV. **(C)** IV relationships obtained after plotting the current magnitude at the end of 5.5s depolarizing pulses. **(D)** Voltage dependence of activation. Activation curves were obtained by plotting the normalized tail current versus the membrane potential. *P<0.05 *vs.*WT K_v7.1/KCNE1, n=6.

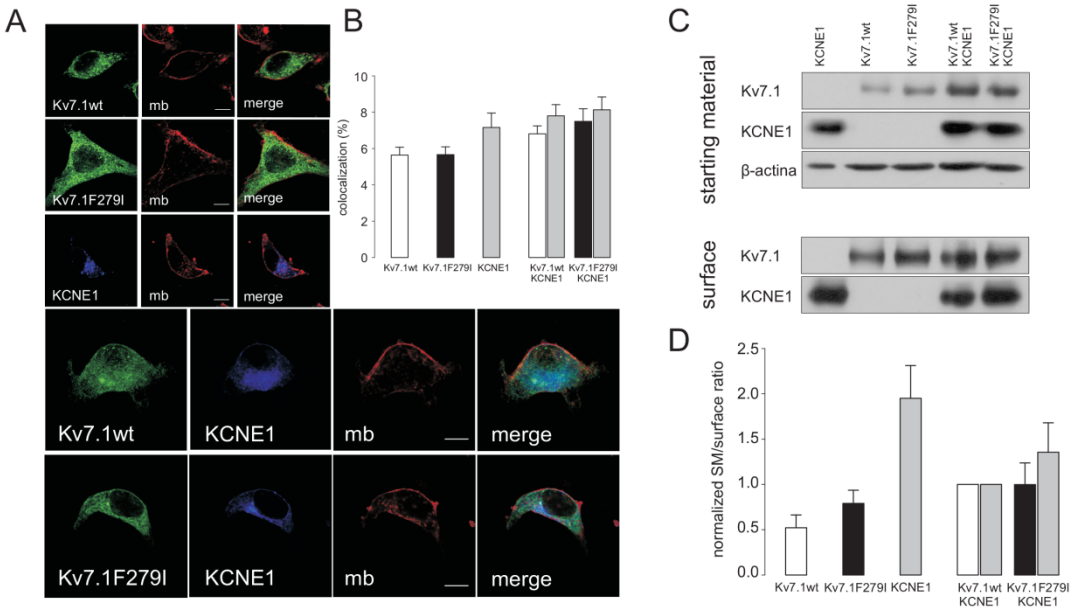

Figure S3. (A) HEK293 cells were transfected or co-transfected with different combination of K_v7.1YFP, F279IK_v7.1YFP, KCNE1CFP and cell membrane was labeled with WGA Alexa 555. Confocal images show no changes in cellular distribution between WT and mutant channel. Red images, plasma membrane staining (mb); green images, WT K_v7.1YFP or F279I K_v7.1YFP; blue images, KCNE1CFP and merge; overlay of pictures of the same series. Scale bar represents 10 μm. **(B)** Histogram showing percentage of colocalization of WT K_v7.1YFP or F279I K_v7.1YFP, with or without KCNE1 with plasma membrane marker, obtained from pixel by pixel analysis of confocal images (n=38-48). **(C)** HEK293 cells were transiently transfected with KCNE1CFP, WT K_v7.1YFP, F279I K_v7.1YFP or co-transfected with WT K_v7.1YFP and KCNE1CFP or F279I K_v7.1YFP and KCNE1CFP. Cells were labeled with biotin and proceed as it is described in Materials and Methods section. Western blot was performed using anti-K_v7.1 and anti-KCNE1 antibodies. Top panel shows starting material bands, K_v7.1YFP channels, KCNE1CFP regulatory subunit and β-actin as a loading control. Bottom panel show levels of biotinylated proteins in each condition. **(D)** Relative abundance of biotinylated channel proteins at the plasma membrane in relation to total expression showed in starting material (n=3).

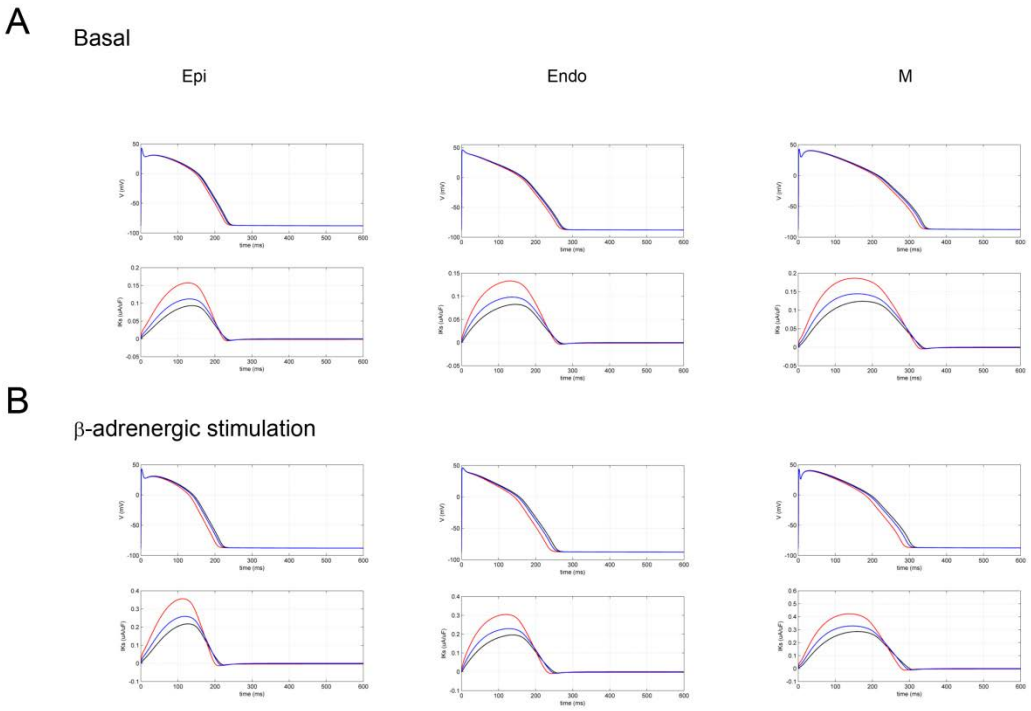

Figure S4. Computational analysis of F279I K_v7.1 effects on the ventricular Action Potential.

(A) Comparison of ventricular action potentials (top) and I_{Ks} current (bottom) in wild-type (WT), F279I K_v7.1/KCNE1 and WT K_v7.1/F279I K_v7.1/KCNE1 conditions for epicardial (left), endocardial (middle), and M (right) cells (basic cycle length: 1,000ms) simulated using the ORd model. **(B)** Simulation of β-adrenergic stimulation in the same conditions as in panel **A** (note the different scale in lower panels showing I_{Ks} time course).

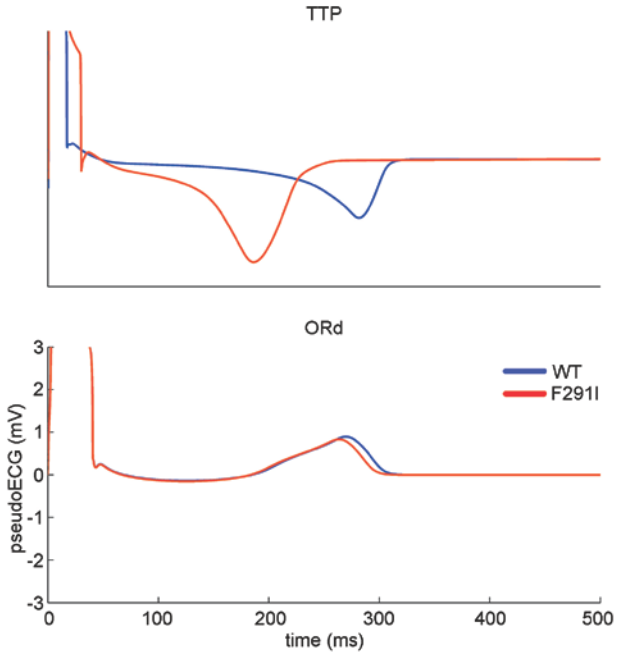

Figure S5. Tissue simulations

The pseudo-ECG computed with TTP (top) and ORd (bottom) model is shown in WT (blue) and mutant (red) conditions.

Additional Tables

Table S1. Activation kinetics of WT K_v7.1/KCNE1, F279I K_v7.1/KCNE1 and WT K_v7.1/F279I K_v7.1/KCNE1 channels after expression in COS7 cells. Time course of activation was fitted to a biexponential equation as described in the Methods section. Results are shown as mean±SEM of 4-9 experiments.

	τ_f (ms)	τ_s (ms)	$A_f/(A_f+A_s)$
WT K_v7.1	125.6±29.7	---	---
F279I K_v7.1	232.0±23.6*	---	---
WT K_v7.1/KCNE1	794.1±35.9	3564.3±481.2	0.75±0.06
F279I K_v7.1/KCNE1	431.8±27.4**	2781.5±209.6	0.62±0.05
WT K_v7.1/F279I K_v7.1/KCNE1	616.9±69.8*§	4212.0±395.2§	0.67±0.06

*: P<0.05 *vs.* WT K_v7.1/KCNE1 or *vs.* WT K_v7.1; **: P<0.01 *vs.* WT K_v7.1/KCNE1; §: P<0.01 *vs.* F279I K_v7.1/KCNE1.

Table S2. Voltage dependence of WT K_v7.1/KCNE1, F279I K_v7.1/KCNE1 and WT K_v7.1/F279I K_v7.1/KCNE1 channels after expression in COS7 cells. Values were fitted to a Boltzmann equation as described in the Methods section. Results are shown as mean±SEM of 4-9 experiments.

	V_h (mV)	s (mV)
WT K_v7.1/KCNE1	32.7±3.2	17.1±0.8
F279I K_v7.1/KCNE1	7.0±4.1**	17.9±1.2
WT K_v7.1/F279I K_v7.1/KCNE1	18.1±3.6*§	16.1±2.0

*:P<0.01 *vs.* WT K_v7.1/KCNE1; **P<0.001 *vs.* WT K_v7.1/KCNE1; §: P<0.01 *vs.* F279I K_v7.1/KCNE1.

Table S3. Activation kinetics of WT K_v7.1/KCNE1, F279I K_v7.1/KCNE1 channels after expression in HL-1 cells. Time course of activation was fitted to a biexponential equation as described in the Methods section. Results are shown as mean±SEM of 6 experiments.

	τ_f (ms)	τ_s (ms)	$A_f/(A_f+A_s)$
WT Kv7.1/KCNE1	459.1±85.2	2143.4±268.7	0.30±0.09
F279I Kv7.1/KCNE1	277.3±28.1*	1909.2±175.4	0.39±0.05

*:P<0.05 *vs.* WT K_v7.1/KCNE1;

Table S4. Voltage dependence of WT K_v7.1/KCNE1 and F279I K_v7.1/KCNE1 channels after expression in HL-1 cells. Values were fitted to a Boltzmann equation as described in the Methods section. Results are shown as mean±SEM of 6 experiments.

	V_h (mV)	s (mV)
WT K_v7.1/KCNE1	40.7±4.4	20.1±2.1
F279I K_v7.1/KCNE1	-1.1±3.8**	19.3±1.8

**:P<0.01 *vs.* WT K_v7.1/KCNE1

Table S5. Action potential duration at 90% repolarization (APD_{90}) of ventricular (endocardial, epicardial and midmyocardial) cells with WT K_v7.1/KCNE1, F279I K_v7.1/KCNE1 and WT K_v7.1/F279I K_v7.1/KCNE1 I_{Ks}, without and with β-adrenergic stimulation, simulated with TTP and ORd models at CL = 1000 ms and 500 ms.

CL = 1000ms		APD_{90} (ms)					
		Endo		Epi		M	
		TTP	ORd	TTP	ORd	TTP	ORd
Basal	WT K_v7.1/KCNE1	300	261	301	228	397	332
	F279I K_v7.1/KCNE1	194	251	196	220	297	318
	WT K_v7.1/F279I K_v7.1/KCNE1	247	258	248	226	350	327
β-adrenergic stimulation	WT K_v7.1/KCNE1	242	246	242	211	340	297
	F279I K_v7.1/KCNE1	149	226	151	195	238	274
	WT K_v7.1/F279I K_v7.1/KCNE1	195	239	197	206	288	289

CL = 500ms		APD_{90} (ms)					
		Endo		Epi		M	
		TTP	ORd	TTP	ORd	TTP	ORd
Basal	WT K_v7.1/KCNE1	274	234	274	206	340	297
	F279I K_v7.1/KCNE1	183	225	184	198	268	285
	WT K_v7.1/F279I K_v7.1/KCNE1	230	231	230	203	308	294
β-adrenergic stimulation	WT K_v7.1/KCNE1	227	216	215	167	304	268
	F279I K_v7.1/KCNE1	146	198	151	148	307	245
	WT K_v7.1/F279I K_v7.1/KCNE1	190	209	193	160	357	259

References

[1] David M, Macias A, Moreno C, Prieto A, Martinez-Marmol R, Vicente R, et al. PKC activity regulates functional effects of KVb1.3 on KV1.5 channels. Identification of a cardiac KV1.5 channelosome. J Biol Chem 2012;287:21416-28.

[2] Macias A, Moreno C, Moral-Sanz J, Cogolludo A, David M, Alemanni M, et al. Celecoxib blocks cardiac Kv1.5, Kv4.3 and Kv7.1 (KCNQ1) channels: effects on cardiac action potentials. J Mol Cell Cardiol 2010;49:984-92.

[3] Moreno C, de la Cruz A, Oliveras A, Kharche SR, Guizy M, Comes N, et al. Marine n-3 PUFAs modulate IKs gating, channel expression, and location in membrane microdomains. Cardiovasc Res 2014;105:223-32.

[4] Valenzuela C, Sanchez Chapula J, Delpon E, Elizalde A, Perez O, Tamargo J. Imipramine blocks rapidly activating and delays slowly activating K+ current activation in guinea pig ventricular myocytes. Circ Res 1994;74:687-99.

[5] ten Tusscher KH, Panfilov AV. Alternans and spiral breakup in a human ventricular tissue model. Am J Physiol Heart Circ Physiol 2006;291:1088-100.

[6] O'Hara T, Virag L, Varro A, Rudy Y. Simulation of the undiseased human cardiac ventricular action potential: model formulation and experimental validation. PLoS Comput Biol 2011;7.

[7] Severi S, Corsi C, Rocchetti M, Zaza A. Mechanisms of beta-adrenergic modulation of I(Ks) in the guinea-pig ventricle: insights from experimental and model-based analysis. Biophys J 2009;96:3862-72.

[8] Mirams GR, Arthurs CJ, Bernabeu MO, Bordas R, Cooper J, Corrias A, et al. Chaste: an open source C++ library for computational physiology and biology. PLoS Computational Biology 2013;9.

[9] Glukhov AV, Fedorov VV, Lou Q, Ravikumar VK, Kalish PW, Schuessler RB, et al. Transmural dispersion of repolarization in failing and nonfailing human ventricle. Circulation research 2010;106:981-91.

APPENDIX B

Supplemental materials: Use of Dynamic – clamp for an improved identification and validation of an ionic current model

---

The content of this chapter has been published in:

Bartolucci C, Altomare C, Bennati M, Furini S, Zaza A*****, Severi S*****

Combined Action Potential- and Dynamic-Clamp for accurate computational modelling of the cardiac I_{Kr} current

Journal Molecular Cellular and Cardiology, vol. 16, no. 3, pp. 396–404, Mar. 2014

***** *Equal contribution to this work.*

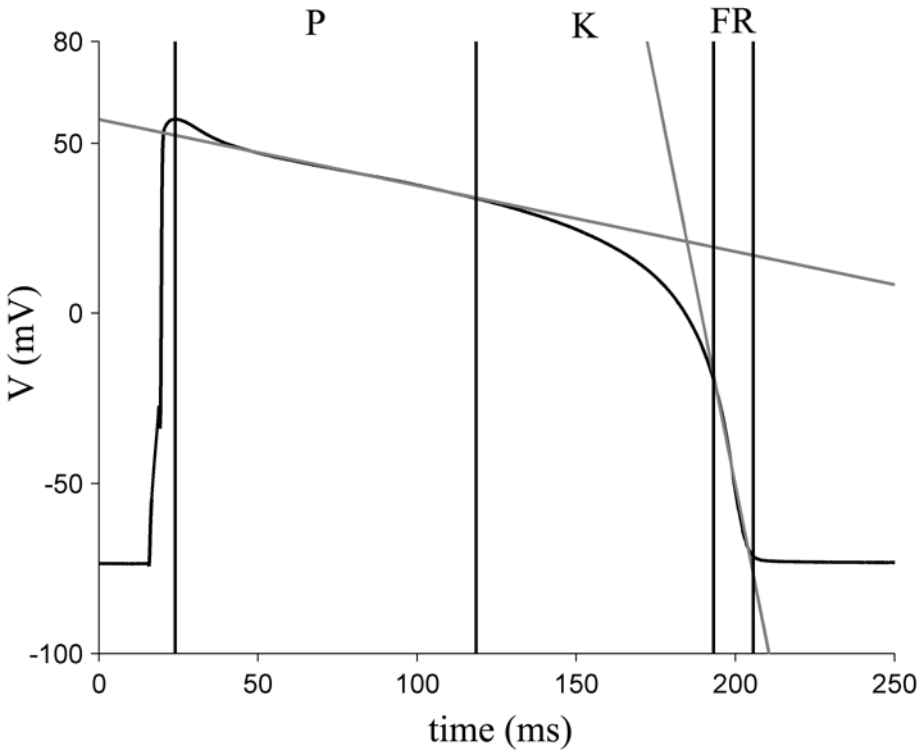

Figure S1. Action Potential (AP) phases

Identification of the 3 phases of the AP: the quasi-linear plateau (P), the non-linear "knee" phase (K), and quasi-linear fast repolarization (FR). The intervals obtained with the algorithm described in the Methods (and attached below) are represented with vertical black lines. The tangents to the AP waveform are also plotted in grey.

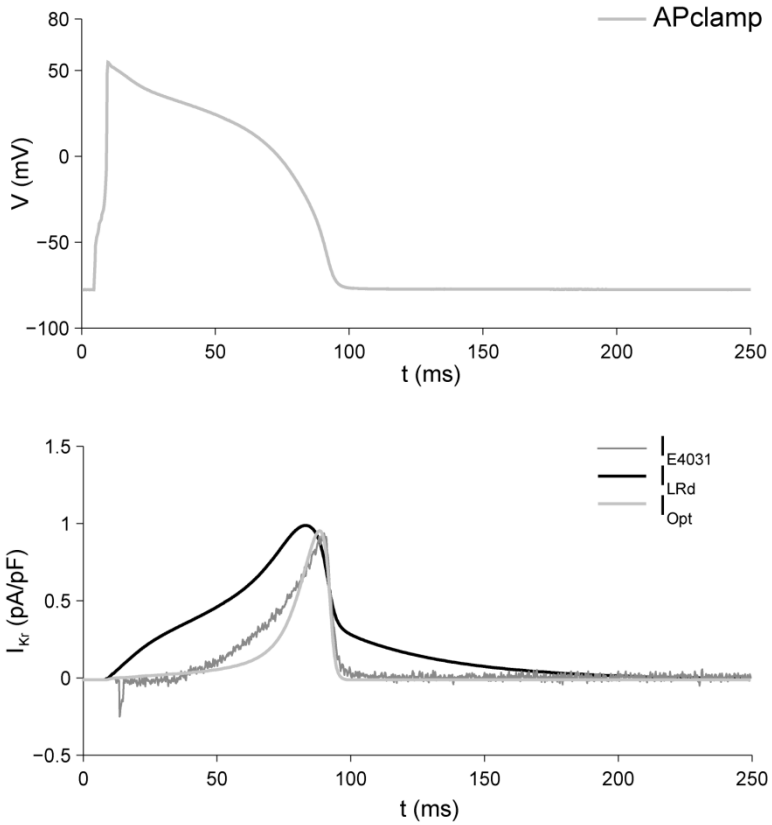

Figure S2. Comparison between IE4031 and modelled currents under AP-clamp at CL = 300 ms

An example of E4031-sensitive current (grey) and the I_{Kr} current computed with the LRd (black) and the optimized (light grey) model (bottom) by using the experimental AP used in the AP-clamp technique (top). See Table 1 in the text for a quantitative comparison of currents at both CL = 1000 and 300 ms.

Table S1. Parameters of the I_{Kr} model (see equations below) and relative constraints

	LRd model	Min	Max	Optimized
p_1	0.02614 mS/µF	0.0132 mS/µF	0.03921ms/µF	0.03 mS/µF
p_2	-21.5 mV	-31.5 mV	-11.5 mV	-20.6 mV
p_3	7.5 mV	5 mV	15 mV	5 mV
p_4	-9 mV	-34 mV	16 mV	-30.7 mV
p_5	22.4 mV	12.4 mV	32.4 mV	14 mV
p_6	180 ms	90 ms	270 ms	270 ms
p_7	-34 mV	-54 mV	-14 mV	-20.5 mV
p_8	20 mV	0 mV	40 mV	20 mV

$$I_{Kr} = \overline{G}_{Kr} * X_r * R * (V - E_{Kr}) \qquad (S1)$$

$$\frac{dXr}{dt} = \frac{Xr_\infty - Xr}{\tau_{Xr}} \qquad (S2)$$

$$E_{Kr} = -\frac{RT}{F} \ln \frac{[K^+]_o}{[K^+]_i} \qquad (S3)$$

$$\overline{G}_{Kr} = p_1 * \sqrt{\frac{[K^+]_o}{5.4}} \qquad (S4)$$

$$Xr_\infty = \frac{1}{1 + e^{\frac{-(V-p_2)}{p_3}}} \qquad (S5)$$

$$R = \frac{1}{1 + e^{\frac{V-p_4}{p_5}}} \qquad (S6)$$

$$\tau_{Xr} = p_6 * e^{\frac{-(V-p_7)^2}{p_8^2}} + 1 \qquad (S7)$$

$$\tau_{Xr_{LRd}} = \left(\frac{0.00138(V + 14.2)}{1 - e^{-0.123(V+14.2)}} + \frac{0.00061(V + 38.9)}{e^{0.145(V+38.9)} - 1} \right)^{-1} \qquad (S7b)$$

TEXT S1: Supplementary Methods

I_{Kr} *model*

To compute the simulated I_{Kr} the model equations were implemented in Matlab 11a (The MathWorks Inc.) and numerically solved by using the ode15s solver. In order to identify the parameters, a standard approach was used: the least square minimization. This method needs an objective function, which was built as the norm of the difference between experimental (I_{Kr1}, I_{Kr2}) and simulated ($\hat{I}_{Kr1}$, $\hat{I}_{Kr2}$) I_{Kr} time course during AP-clamp and the difference between the experimental ($V_{@\mathrm{Ipeak1}}$, $V_{@\mathrm{Ipeak2}}$) and simulated $V_{@Ipeak}$ ($\widehat{V}_{@\mathrm{Ipeak1}}$, $\widehat{V}_{@\mathrm{Ipeak2}}$), i.e. the potential at which I_{Kr} reaches its maximal amplitude, for two different recordings:

$$F_{obj} = \left| I_{Kr1} - \hat{I}_{Kr1} \right|_2^2 + w * \left(V_{@\mathrm{Ipeak1}} - \widehat{V}_{@\mathrm{Ipeak1}}\right)^2 +$$

$$+ \left| I_{Kr2} - \hat{I}_{Kr2} \right|_2^2 + w * \left(V_{@\mathrm{Ipeak2}} - \widehat{V}_{@\mathrm{Ipeak2}}\right)^2$$

where w represent a weight term equal to 500.

To solve the minimization problem a Matlab function was ran: `fminsearch` (multidimensional unconstrained nonlinear minimization based on Nelder-Mead method). Every step we have forced the parameters to belong to their range (see Table S1), assigning an high cost to the objective function if they did not belong. The initial conditions, the vector of LRd parameter values (Table S1), were given as input to the function.

Matlab script files (matrixFinal.m, multiPlot.m) for AP phases analysis

1) matrixFinal.m

```
% Function used to estimate 3 phases of Action Potential (AP):
% plateau phase, fast repolarization and "knee" phase and the corresponding
% amount of current.

% Input: the routine needs a NameFile.xlsx file which can contains
different
% worksheets, corresponding to different experiments, each must
% have in the first column the time, in the second one the current and in
% the third one the corresponding AP (in the first line of each worksheet
% you specify the column subject e.g. time, current, AP).

% Output: the function returns two matrices. DB contains the features
values
% (see the description in the comment to the save instructions in the code)
for % each experiment;
% MeSTD contains mean values and standard deviations.

% For any help or comment please contact: Chiara Bartolucci
% chiara.bartolucci4@unibo.it

clear all;close all;clc;

% Modify to upload the correct file
%[y,sheets]=xlsfinfo('NameFile.xlsx');

jmax=length(sheets);
kmax=1;
for j=1:jmax
    % Modify to upload the correct file
    % file=xlsread('NameFile.xlsx',j);

    siz=size(file);
    n=siz(1,2);
    n=(n-1)/2;
    if kmax<n
```

```
        kmax=n;
    end
end
%DB=ones(jmax,14,kmax);
DB=ones(jmax,17,kmax);
DB(:)=NaN;
clear n sheets kmax

for j=1:jmax
    % Modify to upload the correct file
    % file=xlsread('NameFile.xlsx',j);

    siz=size(file);
    t=file(2:length(file),1);
    dt=t(3,1)-t(2,1);
    sig=file(2:length(file),2:siz(1,2));
    M=(siz(1,2)-1)/2;

    for k=1:M
        p=sig(:,M+k);  % AP
        I=sig(:,k);    % Current

        [picco,tp1]=max(p);

        h=1;
        s1=p(h+1:length(p));
        s0=p(1:length(p)-h);
        ds=(s1-s0)./(h*dt);

        ds=ds(tp1:length(ds));
        [y,tf]=min(ds);
        tf=tp1+tf;

        ti=ceil((tp1+tf)/2.88);


        % Cycle for tangent on the plateau
        im=-1;
        ip=0;
        kl=0;
```

```
Rm=0;
fdx=0;
fsx=0;
Piniz=50;
Rlimit=0.193;

while Rm<=Rlimit && fdx<2 && fsx<2
    if (kl==0 && fdx==0 && fsx==0)||fdx==1
        im=im+1;
        kl=1;
    elseif (kl==1&& fdx==0 && fsx==0)||fsx==1
        ip=ip+1;
        kl=0;
    end

    q=p(ti-Piniz-im:ti+Piniz+ip);
    qm=[q ones(length(q),1)];
    t1=t(ti-Piniz-im:ti+Piniz+ip);
    pol=polyfit(t1,q,1);
    tan1=polyval(pol,t1);
    [y,y,R]=regress(tan1,qm);
    Rm=mean(abs(R([1:Piniz end-Piniz+1:end])));

    if Rm>Rlimit && fsx<2 && fdx<2
        Rm=0;
        if kl==1
            fsx=fsx+1;
            im=im-1;
        else
            fdx=fdx+1;
            ip=ip-1;
        end

    end
end


% Cycle for tangent on fast repolarization
im=-1;
ip=0;
kl=0;
```

```
Rm=0;
fdx=0;
fsx=0;
Piniz=5;
Rlimit=2.3;

while Rm<=Rlimit && fsx<2 && fdx<2
    if (kl==0 && fdx==0 && fsx==0)||fdx==1
        im=im+1;
        kl=1;
    elseif (kl==1&& fdx==0 && fsx==0)||fsx==1
        ip=ip+1;
        kl=0;
    end

    q=p(tf-Piniz-im:tf+Piniz+ip);
    qm=[q ones(length(q),1)];
    t2=t(tf-Piniz-im:tf+Piniz+ip);
    pol1=polyfit(t2,q,1);
    tan2=polyval(pol1,t2);
    [y,y,R]=regress(tan2,qm);
    Rm=mean(abs(R([1:Piniz end-Piniz+1:end])));

    if Rm>Rlimit && fsx<2 && fdx<2
        Rm=0;
        if kl==1
            fsx=fsx+1;
            im=im-1;
        else
            fdx=fdx+1;
            ip=ip-1;
        end
    end
end



tp=t(tp1,1);           % peak istant
tdx=t1(length(t1),1);  % istant tangent plateau last point
tsf=t2(1,1);           % istant tangent fast repolarization first
point
```

```
        tend=t2(length(t2),1); % istant tangent fast repolarization last
point


        DB(j,1,k)=tp;                       % time to peak
        DB(j,2,k)=tdx;                      % end plateau time
        DB(j,3,k)=tsf;                      % start fast repolarization
time
        DB(j,4,k)=tend;                     % end fast repolarization time

        DB(j,5,k)=picco;                    % peak amplitude
        idx=int16(tdx/dt);
        DB(j,6,k)=p(idx);                   % amplitude at end plateau
        isf=int16(tsf/dt);
        DB(j,7,k)=p(isf);                   % amplitude at fast
repolarization begin
        iend=int16(tend/dt);
        DB(j,8,k)=p(iend);                  % amplitude at end fast
repolarization

        tz1=t(tp1:idx);
        I1=I(tp1:idx);
        A1=abs(trapz(tz1,I1));
        DB(j,9,k)=A1;                       % current area during phase 1

        tz2=t(idx:isf);
        I2=I(idx:isf);
        A2=abs(trapz(tz2,I2));
        DB(j,11,k)=A2;                      % current area during phase 2

        tz3=t(isf:iend);
        I3=I(isf:iend);
        A3=abs(trapz(tz3,I3));
        DB(j,13,k)=A3;                      % current area during phase 3

        Atot=A1+A2+A3;
        DB(j,10,k)=(A1/Atot)*100;           % current area% during phases 1
2 e 3
        DB(j,12,k)=(A2/Atot)*100;
        DB(j,14,k)=(A3/Atot)*100;
```

```
        DB(j,15,k) = mean(I(find(t==tp):find(t==tdx))); % current mean
during phase 1
        DB(j,16,k) = mean(I(find(t==tdx):find(t==tsf))); % current mean
during phase 2
        DB(j,17,k) = mean(I(find(t==tsf):find(t==tend))); % current mean
during phase 3



    end
end

MeSTD=ones(jmax,18);                              % matrix of mean and
standard deviation
for j=1:jmax
    MeSTD(j,1)=nanmean(DB(j,2,:)-DB(j,1,:));    % duration phase 1
    MeSTD(j,2)=nanstd(DB(j,2,:)-DB(j,1,:));

    MeSTD(j,3)=nanmean(DB(j,3,:)-DB(j,2,:));    % duration phase 2
    MeSTD(j,4)=nanstd(DB(j,3,:)-DB(j,2,:));

    MeSTD(j,5)=nanmean(DB(j,4,:)-DB(j,3,:));    % duration phase 3
    MeSTD(j,6)=nanstd(DB(j,4,:)-DB(j,3,:));

    MeSTD(j,7)=nanmean(DB(j,9,:));    % area phase 1
    MeSTD(j,8)=nanstd(DB(j,9,:));
    MeSTD(j,9)=nanmean(DB(j,10,:));    % area% phase 1
    MeSTD(j,10)=nanstd(DB(j,10,:));

    MeSTD(j,11)=nanmean(DB(j,11,:));    % area phase 2
    MeSTD(j,12)=nanstd(DB(j,11,:));
    MeSTD(j,13)=nanmean(DB(j,12,:));    % area% phase 2
    MeSTD(j,14)=nanstd(DB(j,12,:));

    MeSTD(j,15)=nanmean(DB(j,13,:));    % area phase 3
    MeSTD(j,16)=nanstd(DB(j,13,:));
    MeSTD(j,17)=nanmean(DB(j,14,:));    % area% phase 3
    MeSTD(j,18)=nanstd(DB(j,14,:));
end
```

2. multiPlot.m

```
% Function used to plot the 3 phases of Action Potential (AP) relative to a
% worksheet previously processed with the matrixFinal script.

% Input: the funciton needs a NameFile.xlsx file which can contain
different
% worksheets, corrisponding to different experiments, each must
% have in the first column the time, in the second one the current and in
% the third one the corresponding AP (in the first line of each work paper
% you specify the column subject e.g. time, current, AP). Only one work
paper
% must be specified in order to run the function.

% Output: the routine returns a figure, with 2 plots which contain the AP
% trace with the different computed phases and the corresponding current
(see Figure S1).

% For any help or comment please contact: Chiara Bartolucci
% chiara.bartolucci4@unibo.it

clear all;close all;clc;

% Modify to upload the correct file;
% Specify the worksheet you want to plot.
% file=xlsread('NameFile.xlsx',1);

siz=size(file);
t=file(2:length(file),1);
dt=t(3,1)-t(2,1);
sig=file(2:length(file),2:siz(1,2));
M=(siz(1,2)-1)/2;
for k=1:M
    p=sig(:,M+k);    % AP
    I=sig(:,k);      % Current

    [picco,tp1]=max(p);

    h=1;
    s1=p(h+1:length(p));
```

```
s0=p(1:length(p)-h);
td=t(1:length(t)-h);
ds=(s1-s0)./(h*dt);

ds=ds(tp1:length(ds));
td=td(tp1:length(td));
[y,tf]=min(ds);
tf=tp1+tf;

ti=ceil((tp1+tf)/2.88);

% Cycle for tangent on the plateau
im=-1;
ip=0;
kl=0;
Rm=0;
fdx=0;
fsx=0;
Piniz=50;
Rlimit=0.193;

while Rm<=Rlimit && fdx<2 &&fsx<2
    if (kl==0 && fdx==0 && fsx==0) ||fdx==1
        im=im+1;
        kl=1;
    elseif (kl==1 && fdx==0 && fsx==0) ||fsx==1
        ip=ip+1;
        kl=0;
    end

    q=p(ti-Piniz-im:ti+Piniz+ip);
    t1=t(ti-Piniz-im:ti+Piniz+ip);
    pol=polyfit(t1,q,1);
    tan1=polyval(pol,t1);
    [y,y,R]=regress(tan1,q);
    Rm=mean(abs(R([1:Piniz end-Piniz+1:end])));

    if Rm>Rlimit && fsx<2 && fdx<2
        Rm=0;
        if kl==1
            fsx=fsx+1;
```

```
            im=im-1;
        else
            fdx=fdx+1;
            ip=ip-1;
        end

    end
end

% Cycle for tangent on fast repolarization
im=-1;
ip=0;
kl=0;
Rm=0;
fdx=0;
fsx=0;
Pinizf=5;
Rlimit=2.3;

while Rm<=Rlimit && fdx<2 &&fsx<2
    if (kl==0 && fdx==0 && fsx==0)||fdx==1
        im=im+1;
        kl=1;
    elseif (kl==1&& fdx==0 && fsx==0) ||fsx==1
        ip=ip+1;
        kl=0;
    end

    q=p(tf-Pinizf-im:tf+Pinizf+ip);
    t2=t(tf-Pinizf-im:tf+Pinizf+ip);
    pol1=polyfit(t2,q,1);
    tan2=polyval(pol1,t2);
    [y,y,R]=regress(tan2,q);
    Rm=mean(abs(R([1:Pinizf end-Pinizf+1:end])));

    if Rm>Rlimit && fsx<2 && fdx<2
        Rm=0;
        if kl==1
            fsx=fsx+1;
            im=im-1;
        else
```

```
                fdx=fdx+1;
                ip=ip-1;
            end
        end
    end

    u=[-200:200]';
    o=ones(length(u),1);

    tpinizdx=ti+Piniz;
    tpinizdx=t(tpinizdx,1);
    tpinizdx1=o.*tpinizdx;
    tpinizsx=ti-Piniz;
    tpinizsx=t(tpinizsx,1);
    tpinizsx1=o.*tpinizsx;
    tpinizU=tf-Pinizf;
    tpinizU=t(tpinizU,1);
    tpinizU1=o.*tpinizU;
    tpinizD=tf+Pinizf;
    tpinizD=t(tpinizD,1);
    tpinizD1=o.*tpinizD;
    ti1=o.*t(ti);

    tp=t(tp1,1);                        % peak istant
    tp2=o.*tp;
    tdx=t1(length(t1),1);               % istant tangent plateau last point
    tdx1=o.*tdx;
    tsf=t2(1,1);                        % istant tangent fast
repolarization first point
    tsf1=o.*tsf;
    tend=t2(length(t2),1);              % istant tangent fast
repolarization last point
    tend1=o.*tend;

    tan=polyval(pol,t);                 % tangent on plateau and fast
repolarization phases
    tanf=polyval(pol1,t);

    figure(k)
    subplot(211)
    plot(t,p,'b',t,tan,'r',t,tanf,'r');hold on
```

```
    plot(tp2,u,'g--',tdx1,u,'g--',tsf1,u,'g--',tend1,u,'g--')
    plot(tpinizdx1,u,'y',tpinizsx1,u,'y',ti1,u,'y--
',tpinizU1,u,'y',tpinizD1,u,'y')
    axis([0 t(length(t),1) -100 100])
    subplot(212)
    plot(t,I,tp2,u,'g--',tdx1,u,'g--',tsf1,u,'g--',tend1,u,'g--')
    axis([0 t(length(t),1) -150 300])

end
```

APPENDIX C

Use of Dynamic – clamp for a sensitivity analysis of the current parameters on the AP features

---

The content of this chapter has been submitted to:

Altomare C, **Bartolucci C**, Sala L, Rocchetti M, Mostacciuolo G, Severi S*****, Zaza A*****,

IKr impact on repolarization and its variability assessed by Dynamic-Clamp

Circulation: Arrhythmia and Electrophysiology, vol. 16, no. 3, pp. 396–404, Mar. 2014

Supplemental Methods and Tables

Table S1. Parameters of the mI_{Kr}: g_{max} = maximal conductance; $V_{0.5}A$ and *sA*= mid-potential and slope factor for steady-state activation; $V_{0.5}I$ and *sI* = mid-potential and slope factor for steady-state inactivation; τ = maximal value of the voltage-dependent activation/deactivation time-constant.

	mI_{Kr}
g_{max}	0.03 mS/μF
$V_{0.5}A$	-20.6 mV
sA	5 mV
$V_{0.5}I$	-30.7 mV
sI	14 mV
$\tau_{act/deac}$	270 ms

Table S2. Recording solutions: extracellular Tyrode's and intracellular pipette solutions.

	Extracellular Tyrode's solution	**Intracellular Pipette solution**
NaCl (mM)	154	
KCl (mM)	4	23
K^+-aspartate (mM)		110
$CaCl_2$ (mM)	2	0.2
$MgCl_2$ (mM)	1	3
HEPES-NaOH (mM)	5	
HEPES-KOH (mM)		5
EGTA-KOH (mM)		0.5
D-glucose (mM)	5.5	
GTP-Na^+ salt (mM)		0.4
ATP-Na^+ salt (mM)		5
Creatine phosphate Na^+ salt (mM)		5
pH	7.35	7.3

Interpretation of SD1, SD2 and SD1/SD2 indexes of variability

SD1 (a.k.a. "Short Term Variability") and SD2 (a.k.a "Long Term Variability") are indexes of temporal variability, initially applied to the analysis of heart rate and more recently applied to repolarization. In previous work [1-3], whereas SD1 was used to quantify "beat-to-beat" variability, SD2 was assumed to reflect variability occurring over a larger number of beats; however, the specificity of these terms was never addressed. In order to clarify the meaning of SD1 and SD2 in terms of variability dynamics, we have tested their performance in a numerical model of variability. The model consisted in a series of 300 values (Y, with mean = 300) in which variability (V) was introduced by a sinus function of adjustable amplitude and frequency. V was generated to oscillate symmetrically around mean Y. In V, the number of beats (N_{beats}) over which Y changes monotonically (i.e. the sinus value goes from 0 to 1) is inversely proportional to the frequency (*f*) of the sinus wave. Figure S1A shows the results of a simulation in which was set to $f = 0.3$ degr/beat, to analyze the case of a fully monotonic variation of Y over the sampled interval ($N_{beats} = 300$). While SD1 was much smaller than SD2 in this case (see below), both indexes showed the same dependency on perturbation amplitude, as demonstrated by constancy of SD1/SD2 (multiplied by 10 to make it compatible with Figure scales). While $f = 0.3$ is an extreme case, independency of SD1/SD2 from V amplitude held true at all *f* values (not shown). These simulations lead to the conclusion that 1) being as affected as SD2 by variations over a large N_{beats}, SD1 does not selectively detect changes in short-term variability ("STV" and "LTV" are actually misnomers for SD1 and SD2 respectively); 2) the SD1/SD2 ratio is instead insensitive to the amplitude of variability. Figure S1B shows that SD1/SD2 is instead a function of *f*, becoming larger as the latter is increased. Therefore, SD1/SD2 specifically reflects the "frequency content" of V, being large when short-term variability prevails over long-term one (it becomes infinite in the extreme case of true alternans). Figure S1C shows Poincaré plots for three specific cases: a) with $f = 0.3$ ($N_{beats} = 300$) data points almost overlap the identity line and SD1/SD2 approaches 0; b) with $f = 90$, $N_{beats} = 4$ (e.g in the cycle 0, 1, 0, -1…) and Poincaré plot forms a square, yielding SD1/SD2 = 1; c) In the special case of pure "alternans" ($f = 180$), $N_{beats} = 2$ (e.g. -1, 1…), points cluster in 2 positions only, Poincaré plot forms a line orthogonal to the identity one (Figure S1Cc), SD2 is null and SD1/SD2 = ∞. This analysis leads to the conclusion that 1) SD1 and SD2 report on changes of variability amplitude, irrespective of its frequency content; 2) the SD1/SD2 ratio is insensitive to variability amplitude, but specifically reflects its frequency content, i.e. it is suitable to discriminate between short-term and long-term variability.

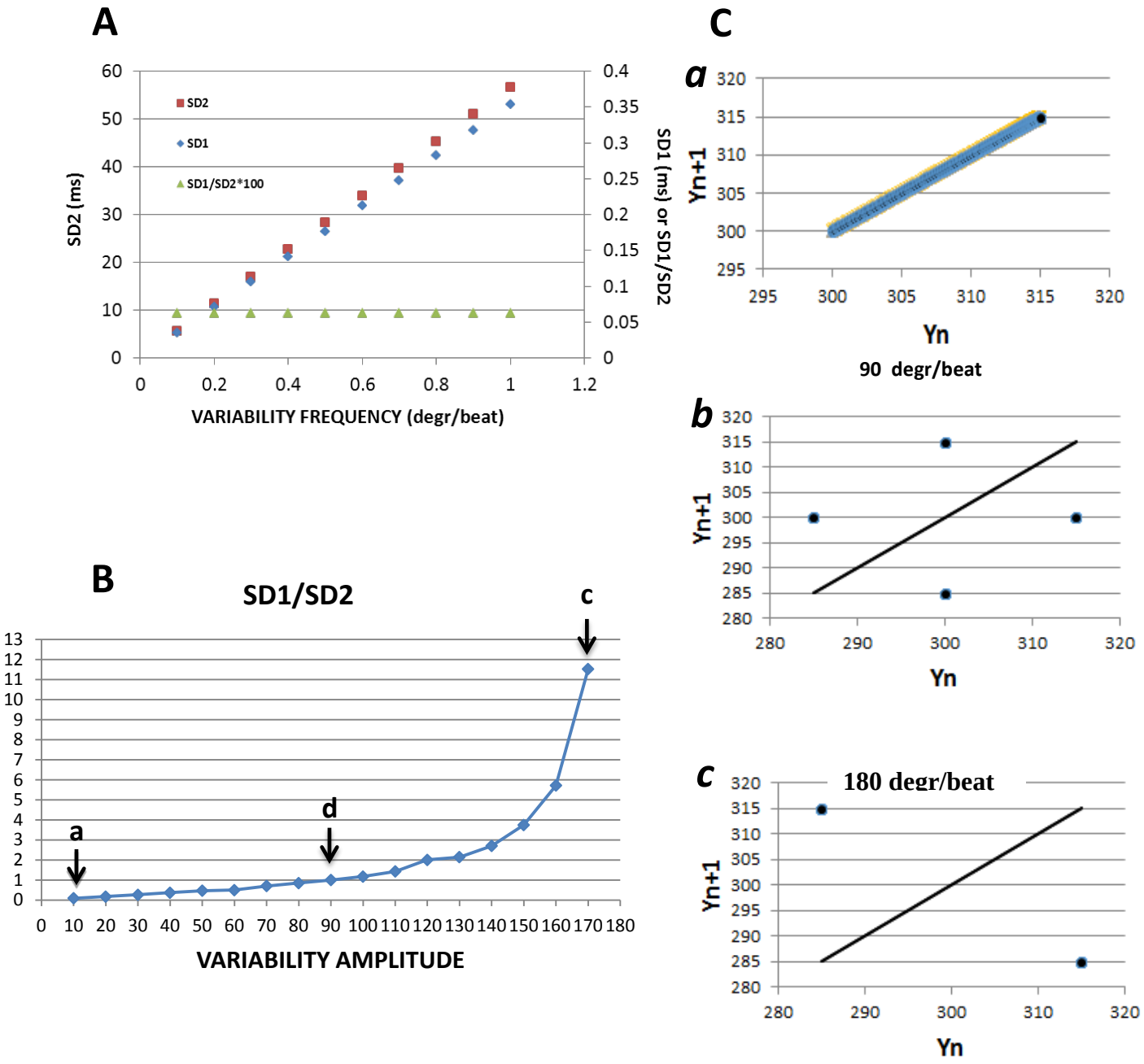

Figure S1: A) dependency of SD2 (left scale), SD2 and SD1/SD2 (right scale, SD1/SD2 multiplied by 10) on variability amplitude; B) dependency of SD1/SD2 on variability frequency (*f*); C) Poincaré plots at 3 frequency points, corresponding to arrows in panel B. Note that in *a*, while visually overlapping the identity line, data points are slightly above it.

Effect of inactivation time dependency on modelled I_{Kr}

The impact of inactivation time-dependency on mI_{Kr} was tested by numerical simulations. To this end, inactivation kinetics was introduced in mI_{Kr}; dependency of inactivation time

constant (τ) on membrane potential, shown in Figure S2A, was simulated according to previous estimates supported by experimental results, obtained in the guinea pig at physiological temperature [4]. Figure S2B compares mI_{Kr} profiles with instantaneous and time-dependent inactivation during an AP. The difference between the two models is limited to a small difference in peak current. Since this difference occurred during AP Phase 3, its impact on APD is expectedly small (see manuscript). This expectation was tested by adding either of the two mI_{Kr} versions (with instantaneous or time-dependent inactivation) to "total membrane current" density (I_m), obtained by differentiation of an AP waveform. New AP profiles were then calculated by numerical integration of I_m traces containing the two mI_{Kr} versions respectively. Figure S2C shows that mI_{Kr} inactivation time-dependency had no visible effect on I_m profile, and caused only a minor (3 ms) prolongation of APD at 90% repolarization (visible as slight "thickening" of the AP trace). A similar approach was used to test for the effect of inactivation time-dependency on the outcome of changes in activation rate. The results (not shown) were again suggestive of a minor impact of inactivation time-dependency.

Overall, these simulations indicate that omission of inactivation time-dependency from the mI_{Kr} formulation should not impact significantly on the outcome of DC studies. Nevertheless, it should be considered that, whereas voltage and current interact in close-loop during a true AP, the present simulations tested only the primary effect of current changes on potential course (open-loop condition). Therefore, they do not rule out the importance of inactivation time-dependency, particularly if slowed by gating abnormalities.

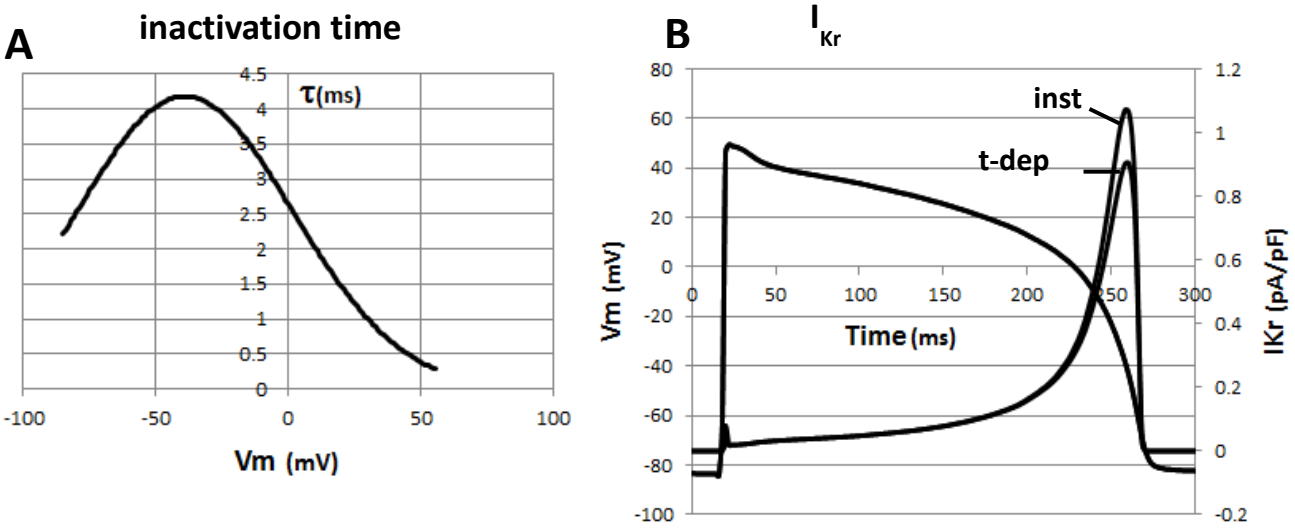

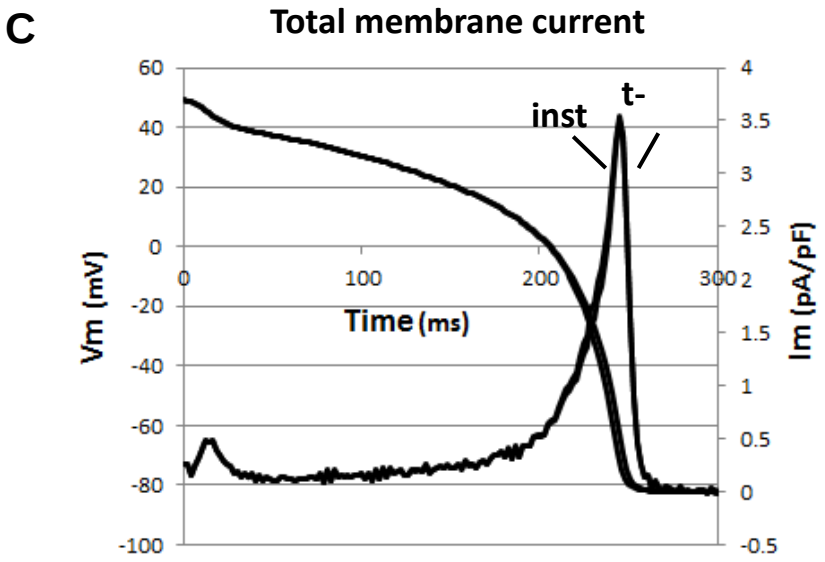

Figure S2: A) voltage dependency of the inactivation time constant (τ) incorporated into the model; B) comparison between mI_{Kr} (right scale) with instantaneous (inst) or time-dependent (t-dep) inactivation during the AP course (left scale); C) total membrane current (I_m) and AP tracings containing mI_{Kr} with either inst or t-dep inactivation. The tracings closely overlap, except during AP phase 3, where the slight thickening reflects a 3 ms difference in APD_{90}.

Effect $V_{0.5}A$ changes without concomitant shifts in τA

According to simple reaction kinetics, shifts in the distribution of states at equilibrium may be associated to similar shifts in the velocity of transitions between states. Therefore, the data concerning $V_{0.5}A$ changes reported in the manuscript (Figure 4.4) were generated by concomitantly shifting V-dependency of activation time constants (τA). The less likely alternative condition, in which shifts in steady-state activation occur without concomitant changes in V-dependency of τA, was tested in a separate series of experiments and is presented in Figure S3.

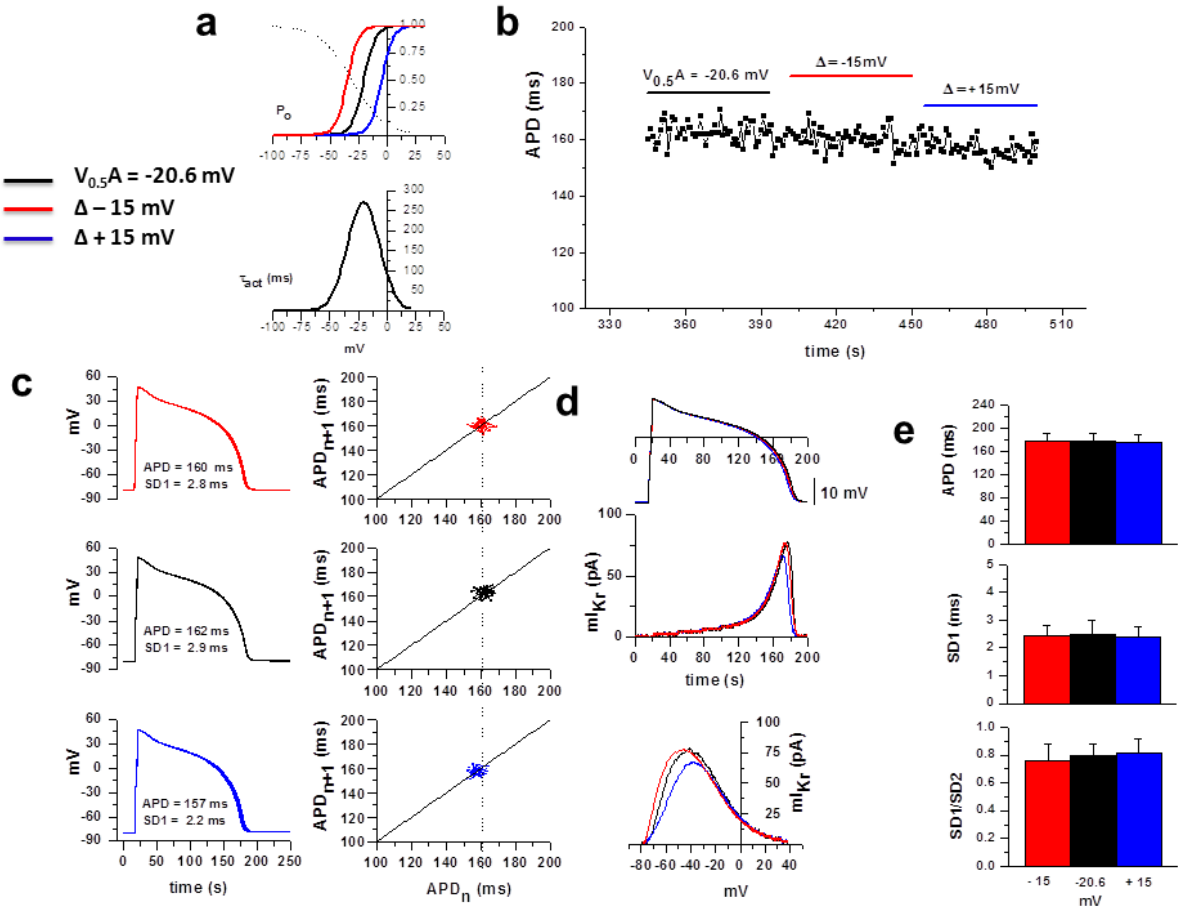

Figure S3. $V_{0.5}$A changes τA-independent. Recordings performed at $V_{0.5}$A = -20.6 mV and with Δ ± 15 mV are shown as: **a)** Steady-state activation (P_o) computed by the model in three conditions (colour) and superimposed inactivation curve (dot line); below $\tau_{act/deact}$ curve in black line; **b)** representative time course of APD recorded at three values of $V_{0.5}$A; **c)** example of 10 APs for each conditions with relative APD and SD1 values and Poincaré plot at the right of panel; ctr APD is evidenced as dot line; **d)** mI_{Kr} profile aligned with the corresponding average AP waveform represented as I/t and I/V_m plots; **e)** statistics of APD, SD1 and SD1/SD2 in all experimental conditions (NS; n = 7).

Table S3. Effect of changes in $V_{0.5}A$, without shifts in τ curves, on mI_{Kr} features, APD and its variability.

V_{peak} = V at peak mI_{Kr} (I_{peak}); TTP: time to I_{peak}; APD: action potential duration at 90% repolarization; SD1: orthogonal APD variability; SD2=longitudinal APD variability (see methods); * = $p<0.05$ vs DC.

$V_{0.5}A$ (mV)	-15	-20.6	+15	# cells
V_{peak} (mV)	42.8 ± 0.25	-42.4 ± 0.4	-42.5 ± 0.15	
I_{peak} (pA/pF)	0.94 ± 0.04 *	0.92 ± 0.04	0.82 ± 0.03 *	7
TTP (ms)	171.9 ± 12.8	175.9 ± 11.7	163 ± 18	

Shifts in $V_{0.5}A$ alone slightly modified mI_{Kr} profile and V-dependency (Figure S3d) during late repolarization (Phase 3), but failed to affect APD and its variability (Figure S3e).

References

[1] Brennan M, Palaniswami M, Kamen P. Do existing measures of Poincare plot geometry reflect nonlinear features of heart rate variability? IEEE Trans Biomed Eng 2001;48:1342-7.

[2] Heijman J, Zaza A, Johnson DM, Rudy Y, Peeters RL, Volders PG, et al. Determinants of beat-to-beat variability of repolarization duration in the canine ventricular myocyte: a computational analysis. PLoS Comput Biol 2013;9:e1003202.

[3] Johnson DM, Heijman J, Bode EF, Greensmith DJ, van der LH, Abi-Gerges N, et al. Diastolic spontaneous calcium release from the sarcoplasmic reticulum increases beat-to-beat variability of repolarization in canine ventricular myocytes after beta-adrenergic stimulation. Circ Res 2013;112:246-56.

[4] Rocchetti M, Besana A, Gurrola GB, Possani LD, Zaza A. Rate dependency of delayed rectifier currents during the guinea-pig ventricular action potential. The Journal of physiology 2001;534:721-32.